Indications of Stress Corrosion Cracking Resistance in Alloy 82 Dissimilar Metal Welds in Simulated Primary Water Environments

by

Suraj Persaud

A thesis submitted in conformity with the requirements
for the degree of Master of Applied Science

Chemical Engineering and Applied Chemistry
University of Toronto

© Copyright by Suraj Persaud 2011

Indications of Stress Corrosion Cracking Resistance in Alloy 82 Dissimilar Metal Welds in Simulated Primary Water Environments

Suraj Persaud

Master of Applied Science

Chemical Engineering and Applied Chemistry
University of Toronto

2011

Abstract

Joints between carbon steel and Alloy 600, containing Alloy 82 weld metal, were exposed to two steam-hydrogen environments considered to simulate exposure to primary water conditions in a Pressurized Water Reactor (PWR) or Canada Deuterium Uranium (CANDU) reactor. The welds were found to have elevated and variable iron contents due to dilution by carbon steel during welding. This gave the Alloy 82 weld, near the inner surface of the component, an iron content approaching that of Alloy 800. A potentially protective external iron oxide film formed on the inner surface of the weld. However, the chromium content throughout the weld is below that which would form an external chromium oxide. The results indicate that low chromium content causes internal oxidation throughout the weld and potentially below the external iron oxide which could lead to Primary Water Stress Corrosion Cracking (PWSCC).

Acknowledgments

I would like to thank my supervisor Professor Roger Newman for allowing me to complete this study; I am grateful for his support and guidance throughout the past two years. Also, I would like to thank Dr. Anatolie Carcea who was always available to help and for discussion regardless of the time or day.

I would like to acknowledge Ontario Power Generation (OPG) and Atomic Energy of Canada Limited (AECL) who provided the weld materials necessary to complete this work. Also, I am grateful for the support and interest from industrial contacts at OPG and AECL who were always available and willing to provide information. I would also like to thank the University Network of Excellence in Nuclear Engineering (UNENE) who provided funding for this study.

I would like to thank Dr. Sridhar Ramamurthy and Surface Science Western (SSW) at the University of Western Ontario for allowing me to set up and use the atmospheric reactor at their facilities. I made several trips to the facilities for periods of up to a week to perform experiments and was always well taken care of. Dr. Ramamurthy was also responsible for performing Auger Electron Spectroscopy (AES) analysis for which I am also grateful.

I would like to express thanks to Mahsa Khatibi and Anatolie Carcea for providing extensive time helping me learn how to use autoclaves and troubleshooting the many problems we encountered. Finally, I would like to thank my many lab colleagues who were always very supportive and made my graduate experience memorable.

Table of Contents

List of Tables

List of Figures

List of Appendices

Chapter 1: Literature Review

1.1 Primary Water Stress Corrosion Cracking (PWSCC)

PWSCC refers to stress corrosion cracking in the primary circuit of Pressurized Water Reactors (PWR) and/or Canada Deuterium Uranium (CANDU) reactors. The purpose of the primary circuit (Figure 1) is to generate heat and transfer it to the secondary circuit. This is accomplished by using uranium fuel bundles to heat water in the reactor vessel. Control rods are used to maintain the rate of reaction by absorbing neutrons. The primary circuit is kept at very high pressure to maintain liquid water at temperatures between approximately 280ºC and 320ºC in present day systems [1]. Constant pressure is maintained using a pressurizer and steam is generated in the steam generator.

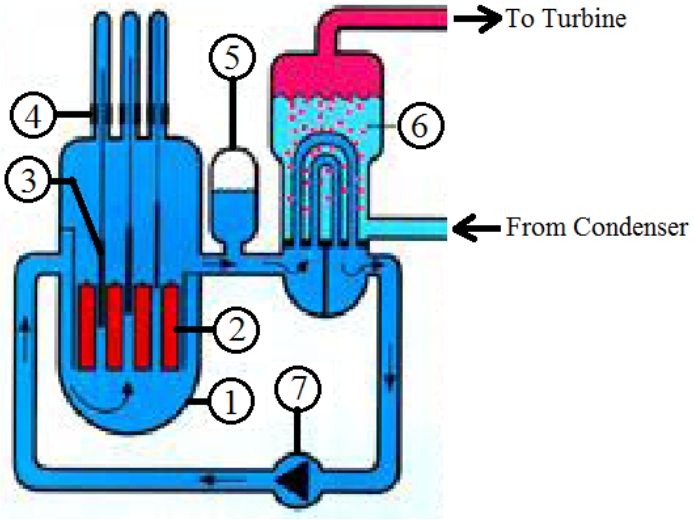

1 – Reactor Vessel 2 – Fuel Elements 3 – Control Rods 4 – Control Rod Dive

5 – Pressurizer 6 – Steam Generator 7 – Main Circulating Pump

Figure 1 – Schematic of the primary circuit in a PWR

Several components in PWRs have been found sensitive to PWSCC such as: steam generator tubes, pressurizer nozzles and welds, and reactor vessel head penetrations and welds. Alloy 600 and its weld materials, Alloy 82 and 182, are Ni-Fe-Cr alloys commonly used to construct these PWR components. Alloy 600 was chosen due to its high corrosion resistance in many

aggressive environments compared to low alloy carbon steel. Table 1 in section 1.1.2 outlines the composition of Alloy 600 and its weld metals as well as other common Ni-Fe-Cr alloys.

Stress corrosion cracking is caused by the combination of 3 factors: a susceptible material, external or residual stress, and a corrosive environment. PWSCC can be eliminated through reduction or replacement of any of these three factors. PWSCC is a function of several variables, including: thermal treatment (carbide distribution), applied and residual stress, grain size, temperature, pH, water chemistry, etc. Consequently, there is no model which successfully incorporates every variable and predicts the occurrence of PWSCC. The variables which effect PWSCC and the proposed mechanisms are discussed in this section.

1.1.1 Primary Water Chemistry

The primary water circuit consists of carefully monitored and controlled water which is not supposed to be particularly corrosive. The temperature in the primary circuit of a PWR ranges from 286ºC in the reactor cold leg to 322ºC in the hot leg and 342ºC in the pressurizer [1]. Lithium hydroxide and boric acid are added to primary water to maintain pH between 6.8 and 7.4 between 280ºC and 320ºC. Hydrogen is added to avoid net decomposition of water by radiolysis in the reactor [1]. The potential is defined by the dissolved hydrogen which is between 20 to 50 $cm^3\ H_{2_{(aq)}}/kg\ H_2O_{(l)}$ at standard ambient temperature and pressure (SATP).

1.1.2 Alloy Composition and Microstructure

The primary constituents of Alloy 600 and its weld metals, Alloy 82 and Alloy 182, are nickel, iron and chromium (Ni-Fe-Cr); a table of compositions for common Ni-Fe-Cr alloys is given in Table 1.

Table 1 – Composition of common Ni-Fe-Cr alloys and welds [3]

		Ni-Fe-Cr Alloys and Welds				
Composition, %	Element	**Alloy 600**	**Alloy 82**	**Alloy 182**	**Alloy 800**	**Alloy 690**
	Ni	72.0 min.	67.0 min.	59.0 min.	30.0 – 35.0	58.0 min.
	Fe	6.0 – 10.0	3.0 max.	10.0 max.	39.5 min.	7.0 – 11.0
	Cr	14.0 – 17.0	18.0 – 22.0	13.0 – 17.0	19.0 – 23.0	27.0 – 31.0
	Mn	1.00 max.	2.5 – 3.5	5.0 – 9.50	1.50 max.	0.50 max.
	Cu	0.50 max.	0.50 max.	0.50 max.	0.75 max.	0.50 max.
	S	0.015 max.	0.015 max.	0.015 max.	0.015 max.	0.015 max.
	Nb	–	2.0 – 3.0	1.0 – 2.50	–	–
	Ti	0.50 max.	0.75 max.	1.0 max.	0.85 – 1.20	–
	Si	0.50 max.	0.50 max.	1.0 max.	1.00 max.	0.50 max.
	C	0.15 max.	0.10 max.	0.10 max.	0.05 – 0.10	0.05 max.

Coriou et al. compared the PWSCC resistance of alloys in chloride environments and pure water [2]. They found that alloys with higher nickel content were more susceptible to PWSCC in pure water. Also, PWSCC resistance was improved as the iron and/or chromium content increased. Figure 2 illustrates PWSCC susceptibility as a function of nickel composition [2].

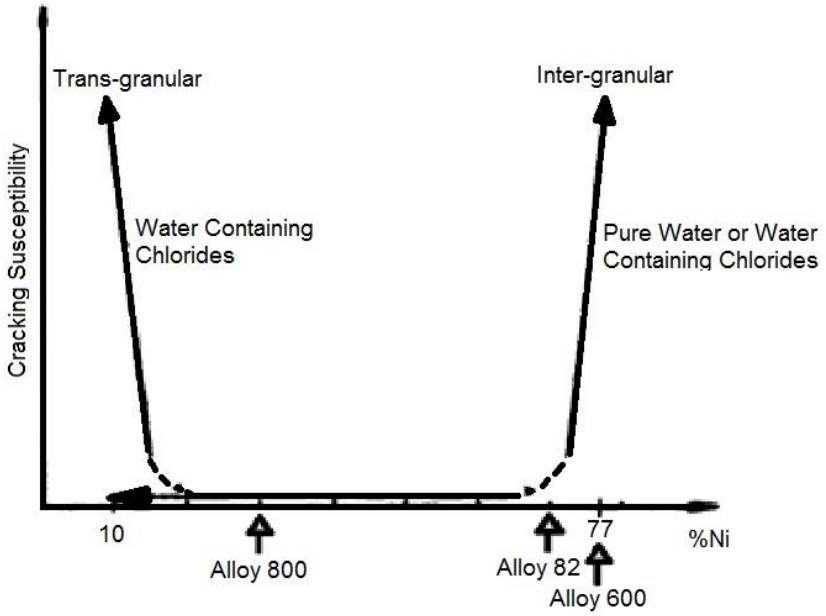

Figure 2 – PWSCC susceptibility as a function of %Ni for Alloys 82, 600 and 800 [2]

Ni-Cr-Fe alloys with higher Fe content, such as Alloy 800 (see Figure 2), tend to be more PWSCC resistant. One possible explanation for this is the formation of a protective iron oxide film on the surface of the alloy. Nickel would not form a protective oxide film in primary water – the conditions are too close to the Ni/NiO dissociation pressure.

Chromium significantly improves the PWSCC resistance of Ni-Fe-Cr alloys. Chromium tends to form an external and passivating Cr_2O_3 oxide film. Delabrouille et al. exposed Ni-Fe-Cr alloys with varying chromium contents (5% - 30%) to simulated PWR conditions at 360ºC and 15.0 MPa [4]. Alloys containing less than 10% chromium did not form a protective oxide. The minimum chromium content deemed necessary to form a protective oxide film was approximately 12%. They found that alloys with the higher chromium content produced a much thinner and more compact external oxide, which contained approximately 90% chromium.

1.1.2.1 Grain Boundary Carbides

Grain boundary carbides have a considerable effect on the PWSCC resistance of nickel alloys. Carbides are usually present as chromium carbides. Chromium carbide, $Cr_{23}C_6$, formation at the grain boundary causes sensitization in nickel alloys. This sensitization is caused by depletion of chromium adjacent to grain boundaries. Carbide precipitation can be eliminated by high temperature annealing (~1100ºC) which causes complete dissolution of carbides [4]. Grain

boundary precipitation occurs when an annealed alloy is thermally treated (TT) and heated between 500ºC and 900ºC [5]. The sensitization of chromium becomes negligible after thermal treatment while the carbides remain on grain boundaries. Figure 3 (a) is a TEM micrograph of an annealed Alloy 600 and (b) is Alloy 600 showing carbide precipitation after being annealed with 16 hours of thermal treatment at 704ºC.

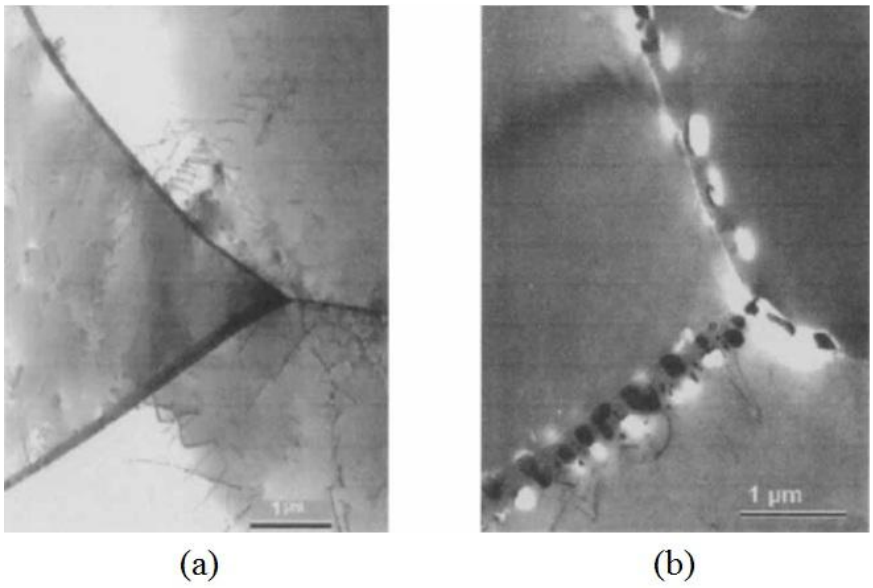

Figure 3 – The grain boundaries of solution annealed Alloy 600 (a) and solution annealed Alloy 600 with thermal treatment at 704ºC (b). Chromium carbides have formed along grain boundaries after thermal treatment (b) [5].

Was et al. [6] performed Constant Extension Rate Tensile (CERT) experiments in pure water at 360ºC to examine the effects of grain boundary chemistry on intergranular cracking. Several Alloy 600 samples were solution annealed and thermally treated for varying times. As they increased the time of thermal treatment, the extent of chromium recovery adjacent to the grain boundaries increased. Thermally treated samples with chromium carbide precipitates were found to be more PWSCC resistant. Furthermore, chromium depletion adjacent to grain boundaries (sensitization) had no effect on PWSCC susceptibility as it recovered with increased thermal treatment time. However, sensitization is undesirable so increasing the time of thermal treatment is common.

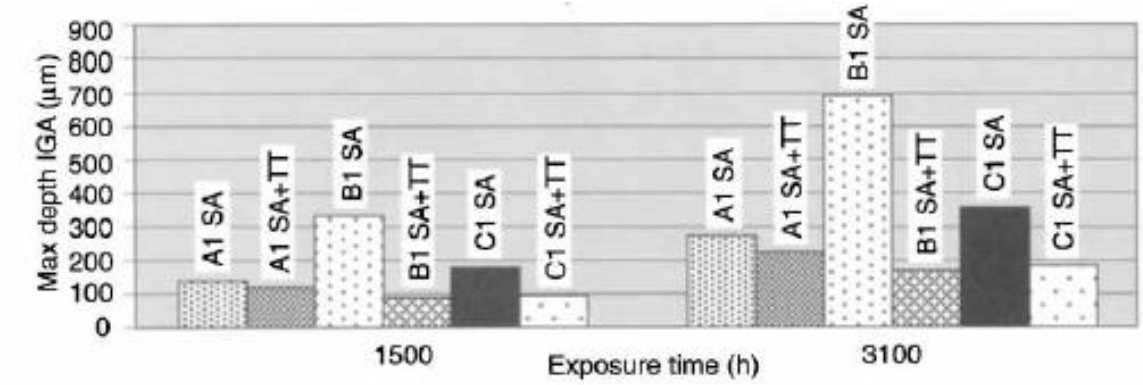

Figure 4 – Comparison of crack growth rate in solution annealed samples (SA) versus those which were solution annealed and thermal treated (SA+TT) [5]

Younes et al. [5] performed further exposures to determine the effect of grain boundary carbides on PWSCC susceptibility. They exposed Alloy 600 and 690 to a high temperature, caustic environment. After thermal treatment, they found that the chromium content at the grain boundaries increased dramatically – by almost 80%. Figure 4 illustrates that the intergranular attack depth was significantly reduced for those samples (A, B, and C) which had been annealed and thermally treated (SA+TT) versus those which were only annealed (SA). These results have been duplicated in other studies as well [7, 8]. Alloy 690 TT exhibits the highest PWSCC resistance. This is due to the combination of a very high chromium content combined with chromium carbide precipitation along the grain boundaries.

1.1.3 Temperature

It has generally been accepted that PWSCC is thermally activated. PWSCC can be described by the Arrhenius equation given in equation 1 [9].

$$k = A \cdot exp\left(\frac{-E_a}{RT}\right) \quad (1)$$

where k is the rate constant (in this case the crack growth constant), A is a constant, E_a is the activation energy, R is the ideal gas constant, and T is temperature. The activation energy for PWSCC initiation is approximately 209 kJ/mol [9] and for PWSCC crack growth approximately 130 kJ/mol [10].

Xu et al. [9] showed that the crack initiation time for Alloy 600 bottom mounted instrumentation (BMI) nozzles varied greatly with temperature. They found that the PWSCC initiation time at

293ºC is 12 times lower than at 327ºC and 37 times lower than at 343ºC. A difference of approximately 50ºC proved to have an enormous impact on PWSCC initiation time.

Temperature can be used to simulate and accelerate PWSCC. Economy et al. [11] attempted to produce intergranular cracks in Alloy 600 in primary water environments. They found the exposure time at 360ºC in primary water conditions required lengthy exposure times. In order to reduce exposure times (i.e. accelerate PWSCC conditions), they found that using hydrogenated steam at 400ºC produced a tenfold increase in PWSCC initiation time. The cracking phenomenon was the same and the role of microstructural variables was similar in both water and steam.

1.1.4 Hydrogen Partial Pressure

The additions to primary water are: lithium hydroxide, boric acid, and hydrogen. The effect of lithium hydroxide and boric acid on the PWSCC susceptibility of nickel alloys is minimal. Changes in pH near the neutral range (which primary water is kept) has minimal effect on PWSCC susceptibility [12, 13]. Figure 5 is a Pourbaix diagram showing the regions of highest cracking susceptibility. It is interesting to note that maximum PWSCC susceptibility occurs at potentials near the Ni/NiO equilibrium line.

In primary water, the corrosion potential is controlled by the addition of hydrogen. The close proximity of the PWSCC region to the Ni/NiO equilibrium means the addition or subtraction of hydrogen can cause changes about the Ni/NiO equilibrium shown in Figure 5.

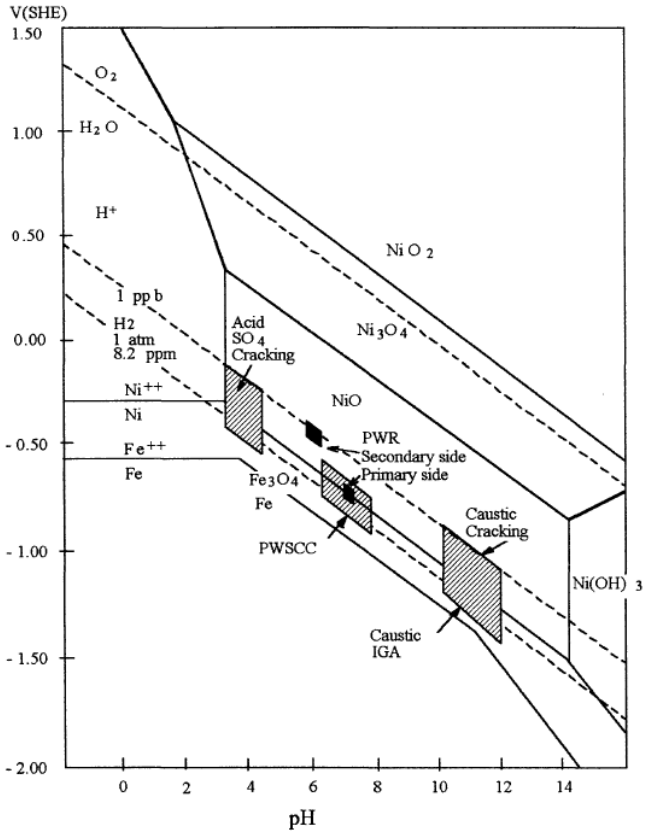

Figure 5 – Pourbaix diagram showing regions of PWR susceptibility to SCC [1]

Andresen et al. performed experiments on Alloys 600, 82, and 182 at 325ºC and 13.7 MPa to examine the effect of Li, B, and H_2 on crack growth rate [12]. Using Li and B to vary pH, they concluded that the crack growth rate between a pH of 5.86 and 7.53 varied minimally (+/- 10%). Morton et al. performed similar experiments at 360ºC between a pH of 6.2 and 8.7 and got similar results [13].

H_2 addition to primary water maintains conditions at 20 - 50 $cm^3\ H_{2(aq)}/kg\ H_2O_{(l)}$ at SATP. Andresen et al. found that near the Ni/NiO equilibrium the crack growth rate is at a maximum. Furthermore, 20 $cm^3\ H_{2(aq)}/kg\ H_2O_{(l)}$ is just to the left of the crack growth peak on the Ni-metal side [12]. Figure 6 shows the crack growth rate was found to be highest near the Ni/NiO transition at all temperatures. Furthermore, the results confirmed that an increase in temperature greatly increases the crack growth rate as discussed in section 1.1.3.

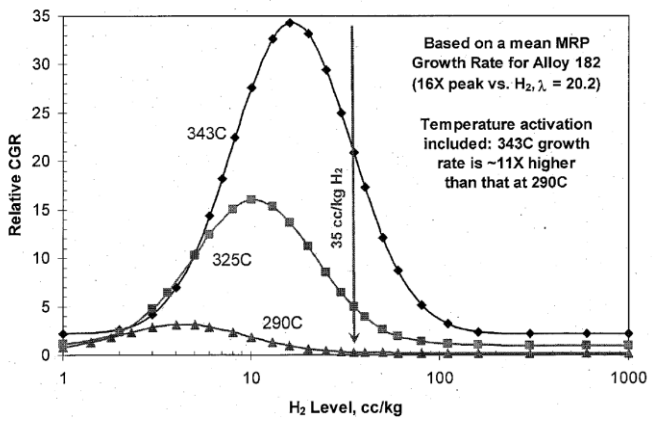

Figure 6 – The effect of H_2 on the relative crack growth rate of an Alloy 182 weld. Crack growth rate is greater near the Ni/NiO oxide equilibrium [12]

Nakagawa et al. performed further experiments with dissolved hydrogen contents varying from 0 to 45 $cm^3\ H_{2_{(aq)}}/kg\ H_2O_{(l)}$ at SATP [14]. Oxide films below 11 $cm^3\ H_{2_{(aq)}}/kg\ H_2O_{(l)}$ were primarily NiO. At the Ni/NiO transition, between 11 - 15 $cm^3\ H_{2_{(aq)}}/kg\ H_2O_{(l)}$, the largest peak in crack growth rate was observed. At greater hydrogen contents, the oxide films formed consisted primarily of Cr and Fe. Also, the ratio of Ni to Ni^{2+} was found to be much greater, indicating they were on the Ni-metal side of the Ni/NiO equilibrium. Their results are shown in Figure 7 (a) and (b).

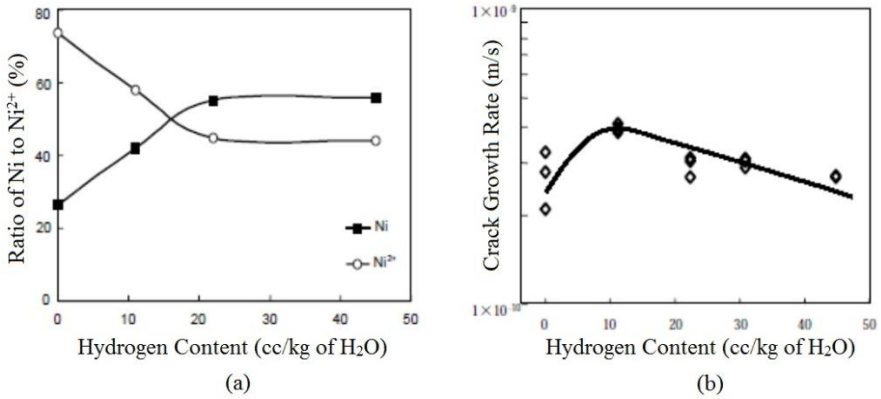

Figure 7 – The effect of H_2 on the transition between Ni and NiO near the Ni/NiO equilibrium (a) and on the relative crack growth rate of Alloy 600 (b) [14]

1.1.5 Possible Mechanisms for PWSCC

Several mechanisms have been proposed to account for PWSCC. None of these mechanisms have proven to be correct for all situations. Each mechanism appears to account for PWSCC with different assumptions or at different stages of crack initiation and propagation.

Rebak et al. examined the different mechanisms of PWSCC and determined that the large amount of variables associated with PWSCC makes it difficult to rely on one particular mechanism [15]. They concluded that PWSCC is a function of eight different variables: grain boundary microchemistry, thermal treatment (carbide distribution), applied and residual stress, grain size, temperature, pH, water chemistry, and the partial pressure of hydrogen. Each mechanism appears to include or neglect different variables.

Possible mechanisms of PWSCC are: slip dissolution, the enhanced surface mobility theory, hydrogen embrittlement, and internal oxidation. Each will be discussed briefly.

1.1.5.1 Slip Dissolution

Ford and Andresen explained that PWSCC is caused by a continuous cycle of oxidation, passivation, and strain [15, 16, 17]. Given the right environment, an active-passive film can form on a metal surface [16]. Oxide films are brittle. Slip dissolution occurs by constant fracture of an active-passive film due to strain or the oxide film not being very protective. Following this, there is dissolution at the crack tip causing it to propagate. Finally, the film reforms and the cycle repeats itself [15, 16, 17].

This mechanism can be modeled taking into account the environment chemistry, material chemistry, and strain rate. Equation 2 is an empirical model describing the slip dissolution mechanism for 304 stainless steel and nickel-based alloys [15, 17]. Mechanistic models also exist to describe slip dissolution [16].

$$V_T = (7.8 \cdot 10^{-3} n^{3.6})(4.1 \cdot 10^{-14} K^4)^n \quad (2)$$

Where V_T is the crack growth rate, K is the stress intensity factor, and n is a constant which takes into account environment and materials chemistry. The model represents primary water at 330ºC quite well for n=0.65. However, the value of n changes depending on environment and alloy chemistry. Determining n can only be done experimentally. Furthermore, this model does

not address many of the other variables associated with PWSCC such as: temperature, thermal treatment, and pH [15].

1.1.5.2 Enhanced Surface Mobility Theory

Galvele proposed the enhanced surface mobility theory as a universal mechanism which explained embrittlement and stress corrosion cracking [18]. He proposed that an atom at the tip of a crack under stress would move, by surface diffusion, from a highly stressed location to the less stressed crack side [15, 18]. Each movement causes the crack to advance by one atom. Figure 8 shows the advancement of an adatom (A) to a new position (B) due to surface stress and a high surface diffusion coefficient. Crack growth rate is described as a function of temperature and the surface diffusion coefficient. The latter is calculated based on the effect of the environment on the surface.

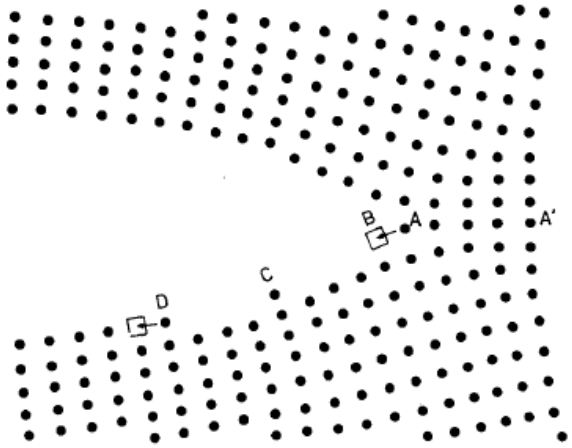

Figure 8 – Schematic representation of the surface mobility theory as proposed by Galvele [18]

The rate controlling step of this mechanism is the rate of movement of the adatoms along the crack. Thus, a surface with a high surface diffusion coefficient would be more susceptible to stress corrosion cracking. Galvele calculated surface diffusion coefficients for oxides such as: NiO, Fe_3O_4, and Cr_2O_3. He classified the oxides by their PWSCC susceptibility. He concluded that NiO formation on Alloy 600 would be necessary for PWSCC to occur. However, cracking has occurred in Alloy 600 below the Ni/NiO dissociation pressure (i.e. in the absence of NiO). Furthermore, the formation of Cr_2O_3 on the surface in the absence of NiO causes the crack growth rate of Alloy 600 to be two orders of magnitude lower than predicted by the surface mobility theory [15, 18].

The formation of carbides on grain boundaries is neglected in this model. The formation of chromium carbide along grain boundaries causes the crack growth rate to be significantly smaller which should, theoretically, decrease the surface diffusion coefficient.

1.1.5.3 Hydrogen Embrittlement

Hydrogen embrittlement is a common SCC mechanism in Alloy 600 and its weld metals, Alloy 82 and 182. Hydrogen embrittlement is not discussed in great detail here because it becomes negligible at temperatures greater than 200ºC unless it is induced by vast loading with hydrogen. Three mechanisms trigger hydrogen embrittlement: gas bubble formation, hydrogen-enhanced decohesion, and hydrogen-enhanced localized plasticity [19]. These 3 mechanisms are described briefly below:

- Gas bubble formation – Hydrogen which diffuses into a metal along grain boundaries can form methane or hydrogen gas. The formation of much larger methane or hydrogen gas bubbles embrittles the grain boundary making it liable to fracture under stress [15].
- Hydrogen-enhanced decohesion – This mechanism is based on the increased solubility of hydrogen under high stress. Hydrogen diffusion decreases the binding forces in the metal lattice. The penetration of hydrogen along grain boundaries weakens the metal bonds. As a result, grain boundaries become susceptible to brittle fracture under stress [15, 19].
- Hydrogen-enhanced localized plasticity – similar to hydrogen-enhanced decohesion, hydrogen diffusion again increases in a region of intense stress. After the application of external stress, a dislocation movement occurs. The hydrogen eases the dislocation movement by shielding it against the stress generated by other dislocations. There is a local drop of yield stress and shearing action occurs which leads to the formation of a small scale ductile fracture [19].

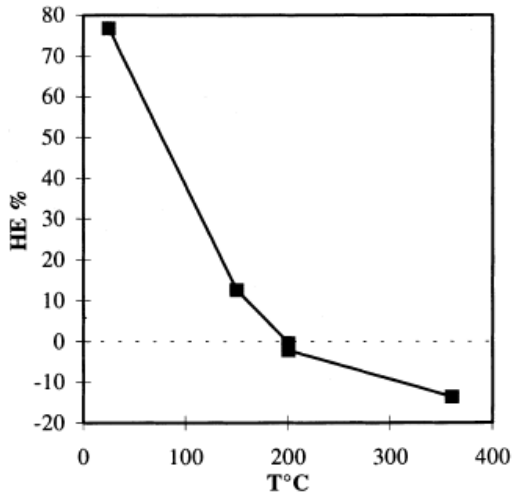

Figure 9 – Graph indicating the percent of cracking in Alloy 600 with 94 ppm of H_2 which occurs as a result of hydrogen embrittlement at different temperatures. The results indicate that hydrogen embrittlement does not affect cracking above 200ºC [20].

Hydrogen embrittlement is prevalent at lower temperatures (from approximately 25ºC to 150ºC). After 200ºC, the effect of hydrogen embrittlement is negligible [15, 20]. Foct et al. investigated hydrogen embrittlement at temperatures from 25ºC to 360ºC with Alloy 600 in environments with 94 ppm of H_2 [20]. They compared the effect of hydrogen embrittlement at different temperatures using a hydrogen embrittlement coefficient (HE %); the coefficient compares the elongation to rupture of an uncharged specimen to the elongation to rupture of hydrogen charged specimens. Figure 9 is their findings which indicate that at elevated temperatures, the effect of hydrogen embrittlement is negligible. Furthermore, there was no correlation between the amount of hydrogen in the environment or absorbed by the material and the severity of SCC. A sample exposed at 25ºC cracked easily while a sample at 360ºC with similar hydrogen charging did not crack [20].

1.1.5.4 Internal Oxidation at High and Low Temperatures

The internal oxidation model is discussed in detail in section 1.3. Internal oxidation is a common phenomenon at high temperatures (greater than 360ºC primary water). It occurs in alloys which consist of a more noble solvent material, such as Ni, and a lower concentration of a less noble material, such as Cr or Al. The less noble metal must be present in low enough quantity such that it does not undergo the transition from internal to external oxide. Under these

conditions, the less noble metal can undergo internal oxidation when the oxygen partial pressure is within range of the dissociation pressure of the more noble metal oxide [21, 22].

At temperatures greater than 700ºC, lattice diffusion is dominant and internal oxidation is primarily intragranular. At lower temperatures, grain boundary diffusion becomes dominant and oxygen would predominantly form oxides along the grain boundary. The ingress of oxygen along grain boundaries can cause embrittlement [22]. This can occur due to oxygen embrittlement of grain boundaries, the formation of a brittle oxide along grain boundaries, or the formation of CO or CO_2 gas bubbles. Due to embrittlement, the grain boundaries are susceptible to fracture under stress [22].

Internal oxidation at high temperatures was observed by Guruswamy et al. in Ag-In alloys [23]. Tests were performed at 550ºC while varying oxygen partial pressures from 1 atm to 10^{-4} atm. Internal intergranular oxidation was observed for In concentrations up to 30 vol.%. At this point, In_2O_3 formed an external oxide. When internal oxidation occurred, pure Ag nodules were expelled to the surface. It was assumed that these nodules were extruded by pipe diffusion to account for the increased volume beneath the surface due to internal oxidation of In.

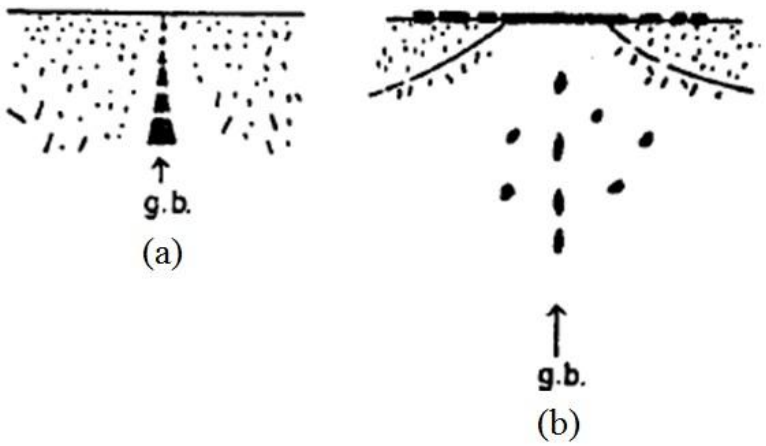

Figure 10 – Intragranular oxidation of Ni-Cr alloys at high temperatures (1100ºC) (a) versus the intergranular oxidation of Ni-Cr alloys at lower temperatures (800ºC) (b) [24].

Wood et al. performed further experiments demonstrating internal oxidation on Ni-Cr alloys by varying Cr content from 1-5% at temperatures from 800ºC to 1100ºC in a Rhines pack of Ni/NiO [24, 25]. Internal oxidation occurred at all conditions, producing primarily Cr_2O_3. At high temperatures, a discontinuous oxide formed which was not preferential to the grain

boundaries. As the temperature was lowered and the Cr content increased, internal oxides tended to form along grain boundaries due to the dominance of grain boundary diffusion. Figure 10 is a schematic representation of the intragranular oxidation (a) and intergranular oxidation (b) that was observed.

Oxygen embrittlement in Ni-based super alloys is similar to internal oxidation in PWSCC. Oxygen has been found to increase the crack growth rate in Inconel 718 at high temperatures (greater than 800K) by up to 4.5 orders of magnitude [26]. It is assumed that oxygen ingress along the grain boundaries causes oxygen embrittlement. Miller at al. exposed nickel-based super alloys to inert conditions and oxygen charged conditions [26]. Oxygen penetration was observed ahead of the crack tip. Oxygen embrittled the grain boundaries increasing susceptibility to cracking. Furthermore, selective oxidation of Ti, Al, Cr, and Nb in Alloy 718 was observed, which may have also increased the crack growth rate.

Scott and Le Calvar were the first to propose internal oxidation as a mechanism of PWSCC at lower temperatures [27]. Alloy 600 in atmospheres with partial pressures of oxygen below the Ni/NiO dissociation pressure could promote the internal oxidation of less noble elements along grain boundaries. Internal oxidation intergranularly could embrittle grain boundaries and cause SCC. High temperature oxidation studies show that internal oxidation occurs easier with higher Cr contents (1-5%) and lower temperatures (800ºC). Given that Alloy 600 contains 16% Cr, it is plausible that at lower temperatures internal oxidation could occur in the absence of an external Cr_2O_3 oxide. Primary water conditions are maintained slightly above or below the dissociation pressure of Ni/NiO at a temperature of approximately 320ºC which could promote internal oxidation of Alloy 600. Furthermore, maximum PWSCC susceptibility is observed in close proximity to the Ni/NiO equilibrium (see Figure 5).

Experimental evidence has been found by Gendron, Newman, and Panter which support the internal oxidation model as a mechanism of PWSCC [28, 29, 30] (See section 1.3.8.1). However, Staehle et al. disagree claiming that experimental evidence does not provide any unique support for the internal oxidation model [31] (See section 1.3.8.2).

1.2 Alloy 82 Dissimilar Metal Welds

Alloy 82 dissimilar metal welds are common in nuclear power plants. Typically, these welds are located between parent materials of stainless steel, carbon steel, or Alloy 600.

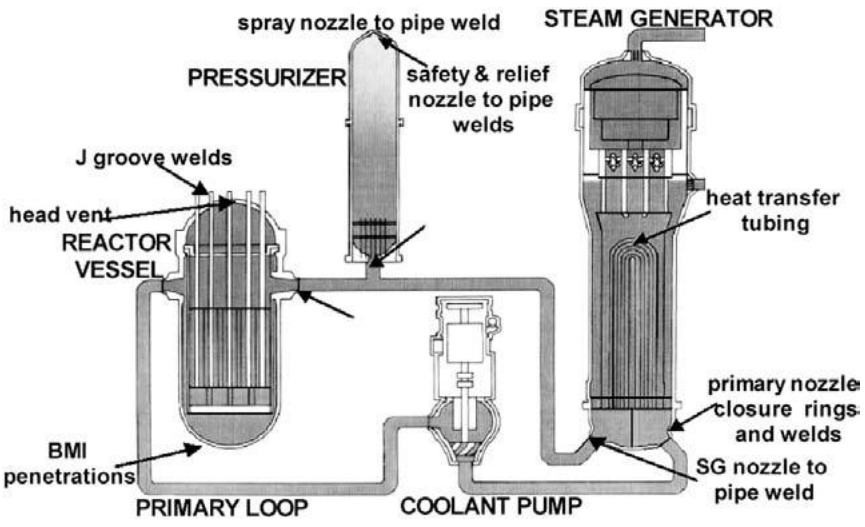

Figure 11 – Location of Alloy 82 dissimilar metal welds in a PWR [32]

In a PWR or CANDU plant, Alloy 82 dissimilar welds are located primarily around nozzles in the reactor, pressure vessel, and steam generator. The location of these nozzles is shown in Figure 11. These welds are usually Gas Tungsten Arc Welded (GTAW) to reduce impurities and enhance operator control during welding (see section 1.2.4).

1.2.1 Microstructure

The microstructure of Alloy 82 welds is similar to that of most metal welds. The grains of welds are much larger. The heat affected zone (HAZ) of the weld area contains enlarged grains and is located at the point of highest heating during welding on the parent material, at the point closest to the weld area. The consequence of having grain boundaries which continue from the HAZ into the weld is that a crack in the HAZ can easily propagate into the weld [33]. Furthermore, Alloy 82 welds have been known to have many carbide inclusions on the surface [34]. The inclusions are typically chromium, niobium, and titanium rich. In particular, niobium-rich inclusions can be found along grain boundaries.

Alloy 82 welds exhibit a dendritic microstructure. Dendrites grow during solidification of the weld and in the opposite direction of heat flow. Crystallization occurs at many different positions during solidification causing dendrites to initiate and grow in different directions. They grow as a result of latent heat that is produced when crystallization occurs. The solidification causes the release of heat which warms the liquid directly in front and either promotes or stops the growth of dendrites [32].

Nucleation of local solidification can be a concern with regards to weld degradation. During welding, minor or major elements can re-arrange themselves in a crystalline form, which is followed by nucleation [35]. As a result, there can be regions after solidification which contain an abundance of one element. It is possible that these non-homogeneous regions are depleted in other corrosion-resistant elements, such as chromium.

1.2.2 Composition

The composition of Alloy 82 dissimilar metal welds varies across the weld. This heterogeneity in composition is due to minor elements locally crystallizing during solidification and dilution due to mixing with the parent material during welding (see section 1.2.3). The nominal composition of an Alloy 82 weld, assuming no dilution and homogeneous crystallization, is given in Table 2. An in-service Alloy 82 dissimilar weld would have a significantly different composition across the surface of the weld.

Table 2 – Nominal composition of Alloy 82 [3]

Element	Ni	Fe	Cr	Mn	Nb	Si	Ti	C
At. %	67 min.	3.0 max.	18 – 22	2.5 – 3.5	2.0 – 3.0	0.5 max.	0.75	0.1 max

The nominal composition of Alloy 82 is similar to Alloy 600. However, Alloy 82 contains Nb and Mn in larger quantities and less Fe. The effect of the minor elements in Alloy 82 on the mechanical properties of the weld is given in Table 3.

Table 3 – The effect of minor elements in Alloy 82

Minor element	Effect on mechanical properties
Manganese, Titanium	Mn and Ti effect mechanical properties positively [21]. The concern with these two minor elements is the potential for localized nucleation causing an area on the surface of the weld to be depleted in chromium. In particular, Mn has been known to be enriched on dendrite boundaries causing depletion of Ni and Cr [21].
Niobium	Nb is common in nickel-based superalloys, such as alloy 625. Nb tends to reside along grain boundaries as carbides or nitrides. Patel et al. showed that including Nb in superalloys increases resistance to dislocations and allows for control of grain boundary size at high temperatures [36]. Furthermore, Nb is added to replace Cr when carbides are formed along grain boundaries. Given the extreme temperatures that welding takes place, Nb would be useful to increase strength and control grain boundary size during welding.
Silicon	Si can be useful in reducing the oxidation rate (including internal oxidation). Silicon contents exceeding 3% have been known to cause embrittlement of Ni alloys [21]. Silicon-rich protective oxides could be formed but this only occurs at very high corrosion potentials [37].
Carbon	C is present in quantities not exceeding 0.10%. Carbon is found in carbide precipitation of the above minor elements. The carbides tend to form along grain boundaries, but could form within grains if present in greater quantity.

1.2.3 Dilution Due to Mixing

Dilution due to mixing is critical when considering the PWSCC resistance of dissimilar metal welds. Dilution can cause a large variation in the composition of the weld – with the potential to change the PWSCC susceptibility of the weld entirely.

Dilution occurs when the composition of one or both parent materials is significantly different than the weld material. In the case of Alloy 82 welded to carbon steel, one would expect a large

variation in iron, chromium, and nickel content in the weld after solidification. Dilution would occur most in the first pass (or the root) of the weld. Subsequent passes would experience dilution by mixing with the previous pass. The final pass would be expected to have a composition near that of the nominal composition of Alloy 82 given in Table 2.

T. Fukumura et al. performed studies on the PWSCC susceptibility of an Alloy 82 dissimilar metal weld with stainless steel and Alloy 600 as parent materials [38]. Dilution of the stainless steel into the weld resulted in an improvement in PWSCC resistance of the weld compared to Alloy 82 welds with Alloy 600 as the sole parent materials. Given the substantial difference in iron and nickel content between stainless steel and Alloy 82, the extent of dilution was considerable.

M. Nouri et al. determined that several factors during welding can affect the rate and extent of dilution [39]. As the wire feed rate of the weld material or the welding speed is increased, the extent of dilution increases. Given these variables, along with the angle of contact between wire feed and the surface, mathematical equations were derived to model the relationship between the welding variables and the extent of dilution.

1.2.4 Gas Tungsten Arc Welding

Gas Tungsten Arc Welding (GTAW) is a welding procedure used for Alloy 82 in PWR and CANDU reactors. It is a highly specialized welding process and considered more difficult than other welding procedures.

The advantage of GTAW is excellent operator control over the weld. This leads to welds with better mechanical properties. When the temperature of the weld is raised to the melting point, the liquid pool formed is vulnerable to contamination. The amount of impurities entering the weld is at a minimum due to the inert gas surrounding the welding area [40]. The electrode is made of tungsten which has a high melting point and does not contaminate the weld.

When welding nickel alloys, some precautions should be taken to reduce cracking and embrittlement. Any sulfur or phosphorus in the atmosphere near the weld would cause severe problems [40]. Sulfur is known to cause hot cracking in nickel alloys due to the formation of NiS around grain boundaries. Phosphorus is detrimental to the mechanical properties of nickel alloys and can cause embrittlement.

1.2.5 PWSCC of Alloy 82

Alloy 82 has been known to undergo PWSCC. Usually, the cracks result in leaks rather than catastrophic failures. There is only one known case where a weld has failed along the circumference [41].

Recent studies by Lima et al. analyzed the PWSCC susceptibility of an Alloy 82/182 weld joint in PWR primary water containing 25 cm^3 $H_{2(aq)}$/kg $H_2O_{(l)}$ and 50 cm^3 $H_{2(aq)}$/kg $H_2O_{(l)}$ at SATP[42]. The first pass of welding was done using Alloy 82 (i.e. the root) and each subsequent pass was done with Alloy 182 (see Table 1 for compositions). Slow Strain Rate Tensile (SSRT) tests were performed on the Alloy 82/182 well joints and the dissimilar metal weld crack growth rate was greater at 25 cm^3 $H_{2(aq)}$/kg $H_2O_{(l)}$ than at 50 cm^3 $H_{2(aq)}$/kg $H_2O_{(l)}$. They did not go into great depth about the effect of dilution on the dissimilar weld. However, it is evident that the iron content is elevated because an Fe-rich oxide film was formed on the surface. The iron oxide was more compact, with smaller crystal sizes, at 50 cm^3 $H_{2(aq)}$/ kg $H_2O_{(l)}$ which suggests that the film formed is protective. The concluded that keeping the dissolved hydrogen closer to 50 cm^3 $H_{2(aq)}$/kg $H_2O_{(l)}$ can help to form a protective oxide film on the surface.

Andresen et al. performed further experiments attempting to mitigate PWSCC of Alloy 82 dissimilar metal welds by optimizing dissolved H_2 [12]. They found that current PWR water contains less dissolved H_2 (closer to 25 cm^3 $H_{2(aq)}$/kg $H_2O_{(l)}$). This was very close to the Ni/NiO dissociation pressure, slightly on the Ni-metal side. By increasing the amount of H_2, the crack growth rate fell dramatically and became negligible at approximately 100 cm^3 $H_{2(aq)}$/ kg $H_2O_{(l)}$. This suggests that increasing the amount of dissolved H_2 is one potential way to mitigate PWSCC in dissimilar metal welds.

P. Scott et al. found that cracks tend to grow where dendrites intersected and where grains formed. This form of SCC was dubbed Inter-Dendritic Stress Corrosion Cracking (IDSCC) [34, 43, 44]. During solidification of the weld, dendrites change direction frequently depending on the direction of heat flow. Furthermore, as the weld is layered, these dendrites can overlap one another. New grains are often found at the boundaries between dendrites and are usually elongated.

Dilution by carbon steel or stainless steel into Alloy 82 during welding has a positive effect on PWSCC resistance [38]. After dilution, the crack growth rate of the weld is one order of magnitude smaller; these results are shown in Figure 12. Unlike dissimilar metal welds, there is a peak where crack propagation increases greatly for non-diluted welds.

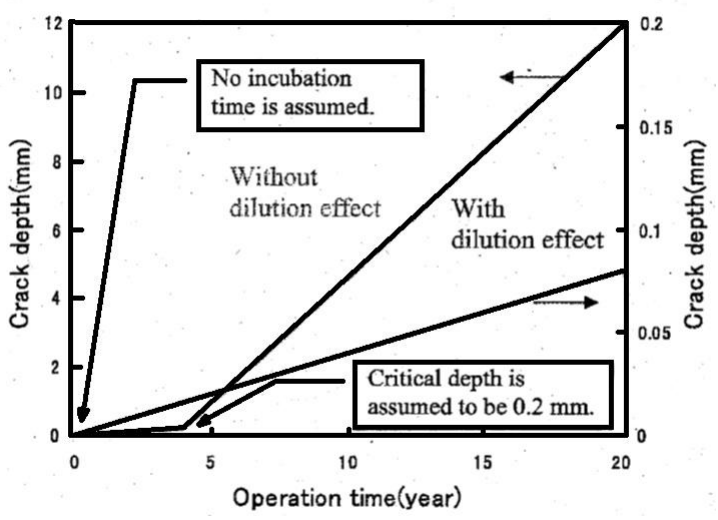

Figure 12 – Crack depth improvement of metal welds with dilution effects versus those without dilution effects [38].

Alloy 82 has been deemed more PWSCC resistant than other dissimilar welds. P. Efsing et al. performed experiments to generate disposition curves (crack growth rate versus stress intensity curves) for both Alloy 182 and 82 [45]. The results indicated that crack growth rate of these two weld alloys plateau at certain stress intensities. Furthermore, when comparing Alloy 182 and 82, there was a factor of improvement of 3 for the latter. Alloy 82 contains significantly more chromium than Alloy 182 (see Table 1). Assuming that the extent of dilution is the same for both welds, Alloy 82 is probably more corrosion resistant due to increased chromium content [34].

1.2.5.1 Determining Crack Growth Rate

Using operator experience and laboratory tests, EPRI created an empirical model for the crack growth rate (CGR) for Alloy 82 [38, 41, 45]:

$$CGR = exp\left[\frac{-E_a}{R}\left(\frac{1}{T} - \frac{1}{T_{ref}}\right)\right] \propto f_{alloy} f_{orient} K^{\beta} \quad (3)$$

This equation takes into account temperature dependence (E_a and T), dendrite and grain orientation (f_{orient}) and stresses on the weld (f_{alloy}). α, K, and β are constants determined experimentally. It should be noted that the effects of dilution or compositional variations are not accounted for in this model. However, dilution normally reduces the CGR in Alloy 82 welds. Nonetheless, this model is useful for determining an estimate of the crack growth rate.

1.3 The Internal Oxidation Model

Internal oxidation is the formation of oxides with minor alloying species beneath the surface of an alloy. Oxygen atoms diffuse into the alloy and react with the less noble minor species; this is illustrated in Figure 13 [46]. The diffusion rate of oxygen into the alloy must be greater than the diffusion rate of the minor alloying species to the surface. In other words, the less noble species are required to be present in small quantity compared to the base metal. The objective is to maintain the oxygen pressure slightly above or slightly below the dissociation pressure of the base metal oxide. This can be done using conventional thermodynamic calculations [21].

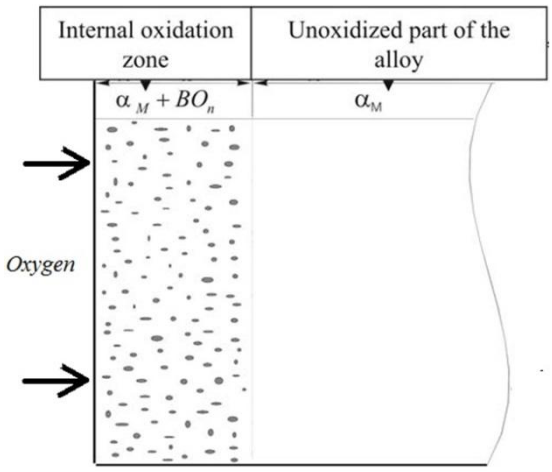

Figure 13 – A simplified illustration describing the basic principle of the Internal Oxidation model

Where the alloy is composed of the base metal, A, and a more reactive minor element, B. α_M is the alloy AB. The reaction between oxygen and B is:

$$B + nO \rightleftharpoons BO_n$$

Where n is the stoichiometric coefficient. The standard Gibbs free energy, ΔG^o, for this reaction must be kept very negative. Also, the $\Delta G^o_{BO} < \Delta G^o_{AO}$ [21, 46]. It is assumed that the metals and

their oxides are both solids and pure. Therefore, their activities are equal to 1. An equation for the $\Delta G^{o}_{BO_n}$ at equilibrium can be found and manipulated for the equilibrium partial pressure of oxygen, $P_{O_2,eqm}$, [21]. This is shown in equation 4.

$$P_{O_2,eqm} = exp\left(\frac{-2 \cdot \Delta G^{o}_{BO_n}}{a \cdot RT}\right) \tag{4}$$

When the partial pressure of oxygen is slightly less or slightly greater than $P_{O_2,eqm}$, the thermodynamic requirement to form the oxide of a more reactive minor alloying element is met. The kinetics of the reaction and the rate of diffusion determine whether or not the oxide will form internally or externally. If the composition of B is sufficient, the minor element will diffuse to the surface and react externally. Also, if the oxygen diffusion rate is insufficient only external oxidation can occur.

1.3.1 Kinetics of the Internal Oxidation Model

Wagner and Rapp derived equations to model the flux of oxygen (N_O) into the alloy and the flux of the minor element diffusing towards the surface of the alloy (N_B) [21, 47, 48, 49]. These were derived using Fick's second law of diffusion. Figure 14 shows the concentration profiles for N_O and N_B defined by the solutions to Fick's second law.

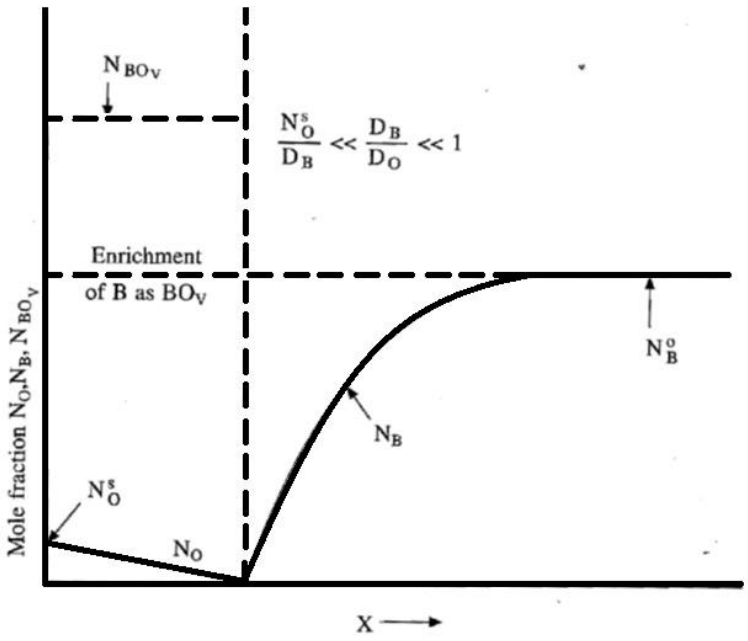

Figure 14 – The concentration profile for N_O and N_B as predicted by Wagner theory [46]

It was concluded that the reaction occurs within the alloy at the point where the flux of the oxygen atoms diffusing into the alloy is equal to the flux of the minor element, B, diffusing outward multiplied by the stoichiometric coefficient, n. This occurs in Figure 14 where x = X. This relationship is given in equation 5:

$$D_O \left(\frac{dN_O}{dx}\right)_{x=X} = nD_B \left(\frac{dN_B}{dx}\right)_{x=X} \quad (5)$$

Through manipulation of the above equation, it can be shown that if there is enrichment of either oxygen or B (i.e. $D_O N_O >> D_B N_B$ or $D_O N_O << D_B N_B$) [48, 49] then the internal oxide formed will be concentrated in oxygen or B.

1.3.2 Internal Stress Build Up

Internal oxidation causes internal stress to build within the metal alloy lattice or along grain boundaries. The volume of the metal oxide beneath the surface is greater than the volume of the metal it replaces. This increase in volume creates stresses between the stress-free surface region and the oxidation front (where internal oxidation occurs and is under compressive stress) [50]. Internal stress relief is achieved by expulsion of pure metal from the base metal to the surface of the alloy via mechanical action and/or diffusion.

Guruswamy et al. have done extensive work on the internal oxidation of Ag-In alloys [23, 48]. They examined the effect of compressive stresses on the oxidation front during internal oxidation. Experiments were performed in air at temperatures ranging from 773K – 1073K. The result was a layer of pure Ag nodules on the surface of the Ag-In alloys. Ag nodules diffused to the surface due to the internal compressive stresses caused by the internal oxidation of In to In_2O_3. Furthermore, the mechanism for diffusion of Ag changes depending on temperature. At lower temperatures, grain boundary diffusion is dominant. Consequently, nodules tend to form along grain boundaries. At higher temperatures, lattice diffusion dominates due to more dislocations being present [23]. This allows for preferential diffusion along dislocation lines which requires less energy than diffusing through grain boundaries. Figure 15 is an Ag-In alloy after exposure with expelled pure Ag nodules on the surface.

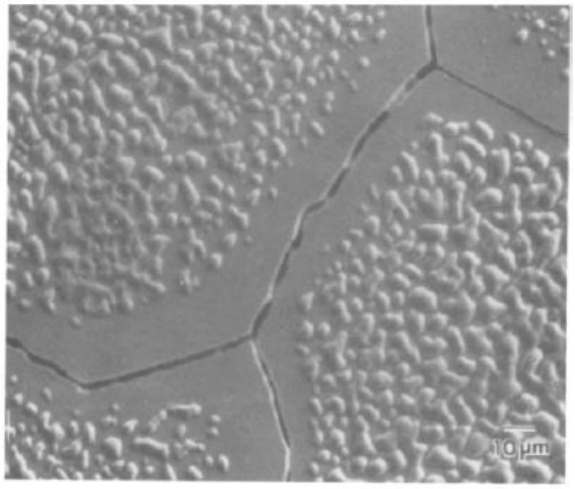

Figure 15 – Ag nodules present on the surface of a dilute Ag-In alloy after 2 hour exposure in air at 1073K [23]

Similar studies were performed on Alloy 600 by F. Scenini et al [50]. Experiments were performed at atmospheric pressure in hydrogenated steam at 480ºC. Conditions were maintained such that the partial pressure of oxygen was below the dissociation pressure of NiO. Performing experiments below the Ni/NiO dissociation pressure would reduce the possibility of NiO being formed on the surface.

After exposure, nodules of pure Ni were discovered on the surface of electropolished Alloy 600 (Figure 16). These were attributed to the diffusion of Ni to the surface to relieve compressive stresses due to internal oxidation of Cr [50]. However, for mechanically polished Alloy 600, an external layer of chromium oxide was formed. Alloy 600 contains 16% Cr which is close to the threshold chromium composition necessary for transition from an internal to external oxide as defined by Wagner theory [47, 48]. The difference in oxidation between electropolished Alloy 600 and mechanically polished Alloy 600 suggests that surface preparation plays a large role in the type of oxidation.

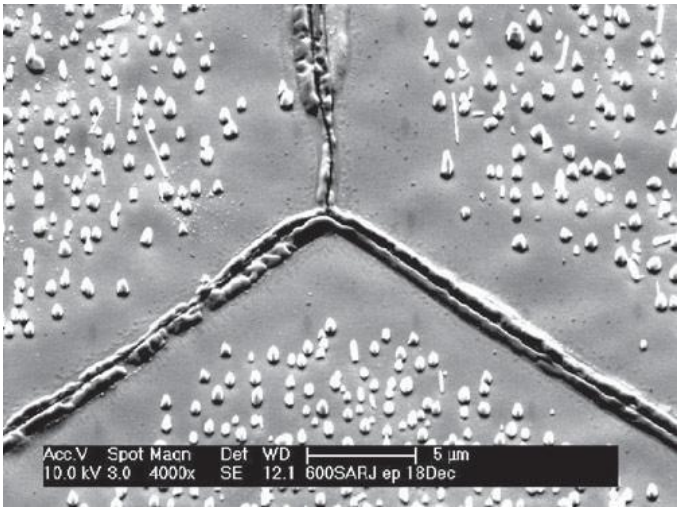

Figure 16 – SEM image of an electropolished Alloy 600 surface after oxidation for 65 h in steam and hydrogen at 480°C, below the dissociation pressure of NiO. Most or all of the features seen are pure nickel expelled through diffusion and/or a pure mechanical action [50]

1.3.3 Transition from Internal to External Oxide

When the composition of the less noble species, B, is increased a critical value is eventually reached where an external oxide, BO_n, is formed rather than an internal oxide. There are two conditions that potentially cause this transition:

- High concentration of B, or rapid diffusion of B towards the surface
- Slow diffusion of oxygen into the alloy or slow flux because of low oxygen partial pressure

Under these conditions, the outward flux of B is greater than the inward flux of oxygen. Section 1.3.1 describes this as $D_O N_O << D_B N_B$. According to Wagner theory, when the volume fraction of oxide reaches a critical value, g^*, transition from internal oxide to external oxide will occur. The equation to model this relationship is given in equation 6 [21].

$$N_B^o = \left(\frac{g^*}{2} \cdot \frac{n N_O^S D_O V_m}{D_B V_{OX}}\right) \quad (6)$$

Where $N_O^S$the oxygen solubility, n is the stoichiometric coefficient, D_O is the diffusivity of oxygen, V_m is the molar volume of the BO_n oxide, V_{OX} is the molar volume of oxygen and N_B^o is the initial concentration of B in the alloy. Rapp tested Wagner's theory in Ag-In alloys. He experimented at 550ºC while varying oxygen partial pressures from 1 atm to 10^{-4} atm. The

transition from internal to external In_2O_3 occurred for a value of $g^* = 0.30$. Knowing the transition point and constant g^* value he could vary the oxygen partial pressure (i.e. increase or decrease N_O^s) and test the agreement between the transition point for the measured results and those calculated from equation 6 [48]. The agreement between experiments and Wagner's theory was excellent.

The presence of another, less noble, alloying element can affect internal to external oxide transition. The oxygen entering the alloy could oxidize the second element. This reduces the rate of oxygen diffusion and makes it favourable for another alloying element to diffuse to the surface and form an external oxide [49].

Newman et al. proposed a percolation theory for the transition from internal to external oxide at low temperatures, where lattice diffusion is negligible. It is based on the idea that the interface between the internal oxide and metal solvent is a good short circuit for diffusion [51]. At low temperatures, the inward diffusion of oxygen would be fast and would internally oxidize less noble species. There is a percolation requirement that the random internal oxide would form a connected skeletal structure rather than particles being dispersed. This nanometer-scale connected skeletal oxide allows the oxide to be transported to the surface faster than through the lattice [51]. This is due to the skeletal interface having a higher diffusivity of the reactive alloying element i.e. Cr compared to the lattice.

1.3.4 Protective versus Porous Surface Oxides

Many alloys form porous oxides which are not protective. Porosity can develop normally for metals such as magnesium and calcium. More commonly, initially protective oxides can crack due to compressive stresses causing them to become porous. Sintering can increase the protective characteristics of a porous oxide film. An increase in temperature will cause the sintering rate to increase exponentially, causing the oxide to become less porous [49].

Oxide metal-volume ratios are commonly used to define whether or not an oxide film is stressed and whether or not that could lead to porosity. This ratio is called the Pilling-Bedworth ratio, R_{PB}, and is defined in equation 7 [52]:

$$R_{PB} = \frac{V_{oxide}}{V_{metal}} = \frac{M_{oxide} \cdot \rho_{metal}}{n \cdot M_{metal} \rho_{oxide}} \quad (7)$$

Where M is the molecular mass, ρ is density, and n is the number of atoms of metal per one molecule. R_{PB} defines criteria which determine whether a metal oxide will be porous or protective as follows [52]:

- For $R_{PB} < 1$, the metal oxide is porous
- For $R_{PB} > 2$, the metal oxide is initially protective but does not adhere to the surface properly due to volume expansion and eventually cracks due to compressive stresses.
- For $1 < R_{PB} < 2$, the metal oxide adheres well to the surface as a protective oxide.

1.3.5 Effect of Temperature

Temperature variations impact the diffusion rate of elements to the surface and oxygen inward. Increasing temperature would increase the kinetic energy of the diffusing atoms. Furthermore, atomic vibrations in the lattice caused by temperature increases would allow for atoms to diffuse easier through dislocations. In general, temperature has an exponential effect on diffusion as defined by the Boltzmann factor.

Temperature also has an effect on the type of diffusion to the surface that solvent atoms undergo during stress relief. Rapp et al. concluded that at lower temperatures, grain boundary diffusion is dominant. Consequently, nodules tend to form along grain boundaries [23]. At higher temperatures, intragranular diffusion dominates due to more dislocations being present. As mentioned, additional dislocations are caused by an increase in atomic vibrations in the lattice. This allows for preferential diffusion through dislocations leading to diminished nodules around grain boundaries.

1.3.6 Internal Oxidation as a Mechanism of PWSCC

Conventional internal oxidation occurs at higher temperatures than PWSCC (greater than 700ºC, see section 1.1.5.4). Scott and Le Calvar were first to propose internal oxidation as a viable mechanism of PWSCC at lower temperatures (approximately 360ºC) [27]. Nickel alloys in environments with partial pressures of oxygen in the vicinity of the Ni/NiO dissociation pressure are susceptible to internal oxidation of minor elements. Oxygen can diffuse down the grain boundaries causing intergranular embrittlement in 3 ways [27]:

- Nickel alloys can form CO_2, CO, or O_2 in vacant cavities along grain boundaries
- Direct embrittlement by O_2 on the grain boundaries through adsorption

- Selective oxidation of chromium

The presence of precipitates (such as carbides or nitrides) along grain boundaries slows O_2 diffusion and can help inhibit PWSCC.

1.3.6.1 Examples

The use of internal oxidation as a model to describe PWSCC of nickel-based alloys occurs frequently. Some examples of PWSCC which support internal oxidation are given below:

Gendron et al. performed high pressure steam/hydrogen experiments at 400ºC on Alloy 600 [28]. Irreversible embrittlement was found along grain boundaries. There was no strain applied so this could not be explained by other conventional PWSCC mechanisms. Scanning Electron Microscope (SEM) examination of specimens revealed brittle intergranular fracture to a depth of 1 µm. Secondary Ion Mass Spectroscopy (SIMS) analysis confirmed that minor reactive elements, such as Cr, along grain boundaries were oxidized. At 1 µm depth, no further penetration of oxygen was observed. Furthermore, longer exposure times did not have an impact on the depth of oxygen penetration. This suggests that a healing layer of Cr_2O_3 at some critical depth was formed which prevented further ingress of oxygen.

Newman et al. performed experiments in hydrogenated steam at 400ºC and found that Alloy 690 and Alloy 800 generally are not susceptible to internal oxidation [29]. The chromium content in both of these alloys is significantly higher than Alloy 600. Therefore, the flux of Cr diffusing to the surface is sufficient to undergo the transition from internal to external oxide. On Alloy 690 and Alloy 800 a protective external Cr_2O_3 film can form which inhibits PWSCC. The observations of Newman et al. are consistent with internal oxidation and Wagner theory.

Experiments have been done which demonstrate the influence of grain boundary carbides on PWSCC. Panter et al. described carbides as having the ability to impede the diffusion of oxygen and reduce internal oxidation along grain boundaries [30]. However, this "blocking" mechanism is unlikely. Newman et al. propose that the carbides create a chromium reservoir [52]. Cr_2O_3 carbide formation inhibits oxygen diffusion due to an elevated concentration of Cr at carbides.

In some cases, Alloy 600 exposed to PWR environments did not crack after thermal treatment with carbides residing along grain boundaries. Panter et al. suggested that the internal oxidation of chromium produced vacancies containing oxygen atoms. The oxygen atoms can be transported toward the grain boundaries causing embrittlement [30]. Figure 17 illustrates how the presence of carbides would create a Cr_2O_3 reservoir and not allow oxygen to embrittle grain boundaries.

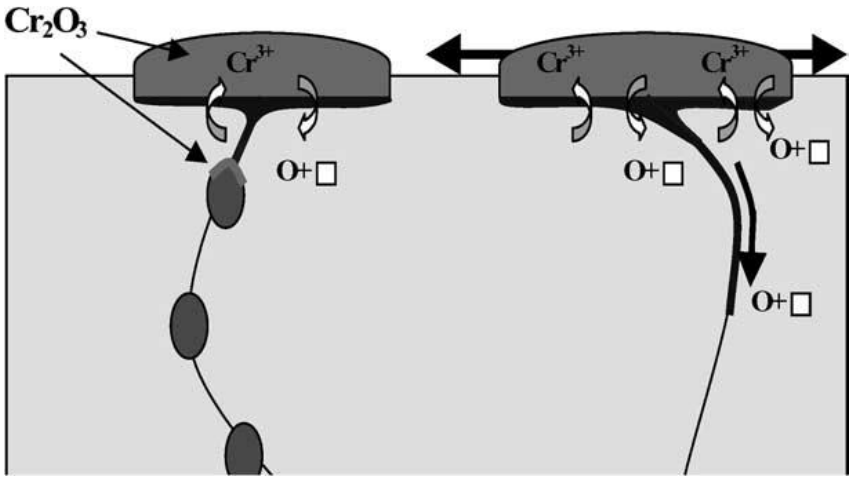

Figure 17 – Vacancies which allow oxygen diffusion embrittles grain boundaries via internal oxidation. The benefit of carbides being present along grain boundaries is oxygen ingress beyond carbides is greatly reduced [30].

1.3.6.2 Criticisms of the Internal Oxidation Model

Staehle et al. argue that the internal oxidation model is not reasonable as a mechanism of PWSCC [31]. In their opinion, the experimental evidence which support the internal oxidation does not provide any unique support for the internal oxidation model. Staehle analyzes the potential-dependent solubility of oxygen versus the occurrence of PWSCC and the depth of intergranular oxygen diffusion to criticize the internal oxidation model.

Staehle's first claim is that there is no correlation between oxygen solubility in the metal and PWSCC [31]. The oxygen solubility is at a maximum right at or above the Ni/NiO equilibrium and rapidly decreases at lower potentials below the Ni/NiO equilibrium. He also derives equations for mixed oxides containing Cr or Fe on the surface. His assumption is that at potentials higher than the Ni/NiO equilibrium, NiO is formed and the oxygen solubility is at a

maximum and remains constant. At lower potentials, mixed oxides of Ni, Cr, and Fe will form and the oxygen solubility would be defined (much lower) at those potentials.

Essentially, Staehle is assuming that an external NiO oxide must always form. This is not true. NiO does not form externally on Alloy 600 below or near the Ni/NiO equilibrium. The conditions are kept slightly above or slightly below the Ni/NiO equilibrium in primary water. According to Staehle, the potential at the Ni/NiO equilibrium is when oxygen solubility is at its peak. Just below this peak is where internal oxidation occurs. Once you have initiation of internal oxidation, the metal near the surface is Ni so there is very high oxygen solubility. Furthermore, the Pourbaix diagram in section 1.1.4 confirms the assertion that PWSCC occurs near the Ni/NiO equilibrium.

Staehle's second argument was that the depth of intergranular oxygen diffusion predicted by the internal oxidation model does not support experimental data of grain boundary oxygen diffusion depth at temperatures from 800ºC to 1300ºC [31]. Experimental data at high temperatures was extrapolated to PWSCC temperatures (approximately 360ºC). Two equations were derived to by Staehle to describe oxygen diffusion depth: equation 8 for Staehle's prediction and equation 9 as predicted by Scott for internal oxidation.

$$d = \left\{t \cdot \left[exp\left(0.0296 - \frac{3.20 \cdot 10^4}{T}\right)\right]\right\}^{0.5} \quad (8)$$

$$d = \left\{t \cdot \left[exp\left(-15.52 - \frac{1.31 \cdot 10^4}{T}\right)\right]\right\}^{0.5} \quad (9)$$

Where d is the depth of intergranular oxygen penetration (m), t is the time of experiment (s), and T is the temperature (ºK). The results of equations 8 and 9 were plotted and Staehle determined that high temperature experimental evidence produced depth penetrations up to 10000 times lower than those predicted by Scott. However, Staehle does admit that Scott's depth of intergranular diffusion does correlate well with the range of penetrations actually observed in experiments, such as those by Gendron et al. [28].

Scott countered Staehle's argument by comparing the extrapolation of high temperature diffusion data to actual experimental evidence of the crack growth rate at low temperatures [1]. From Figure 18 it is clear that it is impossible to account for the crack growth rate from 400ºC

to 800ºC using intergranular diffusion data alone. Staehle appears to be making a massive extrapolation which could be inaccurate. Furthermore, experiments, such as those by Gendron et al., prove that internal oxidation does happen at lower temperatures regardless of Staehle's theoretical criticisms and extrapolations.

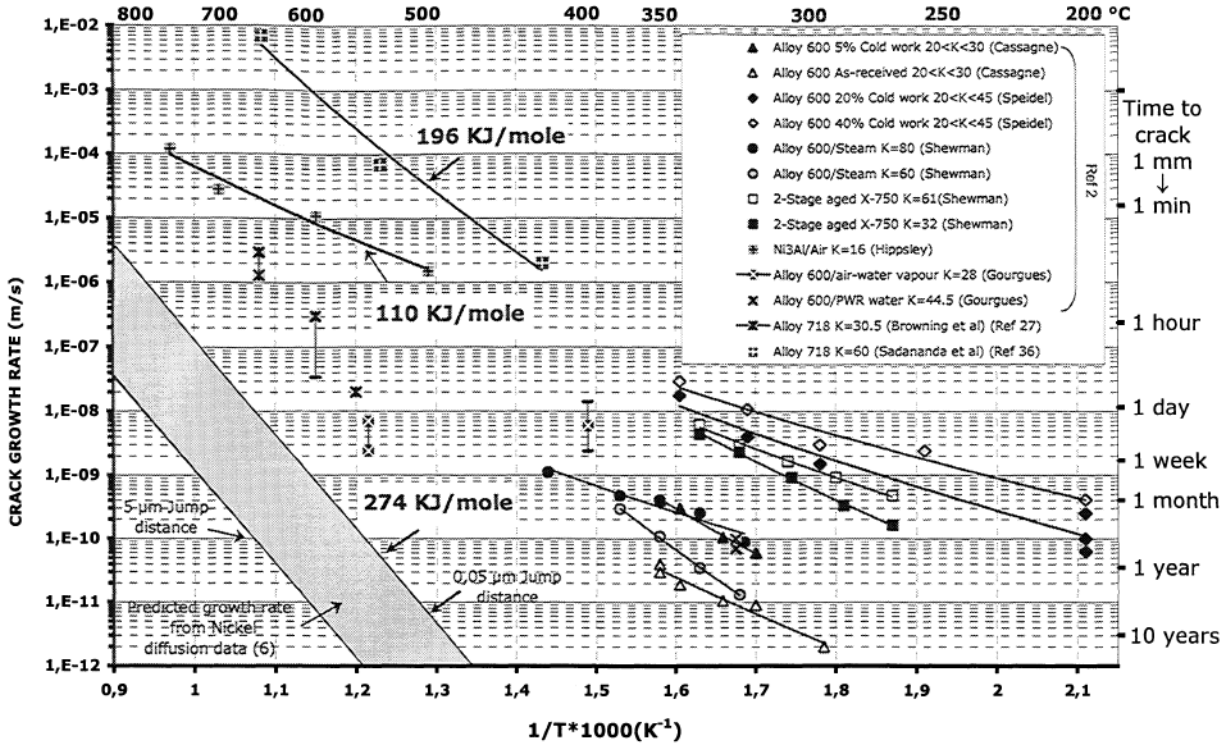

Figure 18 – Arrhenius plot of oxygen induced cracking above 425°C and intergranular SCC below 425°C of various Ni-base alloys [17].

Gendron et al. performed experiments at 400ºC which demonstrated that oxygen intergranular diffusion depth is in agreement with the internal oxidation model [28]. The depth of oxygen penetration was observed to be up to 1 µm at 400ºC. The theoretical depth of penetration can be calculated using equations 8 and 9 and Gendron's data to validate the internal oxidation model. The internal oxidation model predicts a depth of penetration of 7.4 µm while Staehle's oxygen diffusion profile predicts 14 nm. The internal oxidation model overestimates by a factor of 7 while Staehle's model underestimates by a factor of 70.

1.3.6.3 Potential Immune Systems

Potential immune systems to PWSCC by internal oxidation include Alloy 690 and Alloy 800. These two alloys are considered as potential replacements for Alloy 600 in nuclear power plant

piping. However, Kilian et al. have reported that Alloy 800 has cracked under secondary side water conditions [54]. The corrosion resistance of these two alloys compared to Alloy 600 can possibly be attributed to the following compositional differences:

- Alloy 690 contains 27% - 31% chromium, almost double the chromium content of Alloy 600
- Alloy 800 contains 19% - 23% chromium and a minimum of 35% iron

The apparent immunity of these two alloys in PWR environments near the Ni/NiO dissociation pressure can be attributed to protective oxide films which form on the surface. In Alloy 690, this film is purely chromium oxide. Alloy 800 is interesting due to the elevated iron content. Iron has the potential to form a protective oxide film of magnetite, Fe_3O_4. In Alloy 800, there is the potential for layers or mixed layers of protective oxide films of Cr_2O_3 and Fe_3O_4. These films inhibit the diffusion of oxygen reducing the likelihood of embrittlement by internal oxidation[29].

Dutta et al. performed experiments on Alloy 600, 690 and 800. They determined that alloy 800 has grain boundary carbide precipitates which help to inhibit oxygen diffusion [53]. In addition, after exposure of Alloy 800 in steam for 264h, they found mixed oxides of both chromium and iron on the surface. Alloy 690 and Alloy 800 have better SCC resistance in pure water than Alloy 600 but have been known to undergo SCC in caustic environments [53]. After exposure in an acid chloride environment, Alloy 690 formed a protective chromium oxide film with no iron or nickel oxides present.

Scenini et al. performed experiments in hydrogenated steam at 1 atm and 480ºC on both alloy 600 and alloy 690. Alloy 600 had internally oxidized which caused the expulsion of pure nickel nodules to the surface. Alloy 690 did not internally oxidize at all but possibly underwent some thermal etching [50]. Experiments at similar Ni/NiO conditions, but at 400ºC, were carried out by Capell and Was [55]. Their results indicated the formation of an unprotective $Ni(OH)_2$ film. However these results are inconsistent with Scenini's work and Wagner's kinetic theory. Given the low chromium content of the nickel alloys tested by Capell and Was, one would expect internal oxidation of chromium to happen rather than a nickel hydroxide film being formed.

Chapter 2: Introduction and Hypothesis

Alloy 82 dissimilar metal welds are found in several designs of nuclear plant. The Stress Corrosion Cracking (SCC) resistance of these and other nickel-base alloy welds in the presence of primary coolant is debatable, and much research has been carried out [34, 38, 41-45].

The welds in question have a non-homogenous microstructure. They are composed of dendrites with local recrystallization. Furthermore, there are defects such as niobium carbide inclusions at dendrite boundaries. Similar nickel alloy welds, such as Alloy 182, have been found to undergo inter-dendritic stress corrosion cracking (IDSCC) in simulated PWR environments [34, 43, 44]. SCC susceptibility of Alloy 82 welds has been observed to increase near the Ni/NiO dissociation pressure [12]. This suggests internal intergranular oxidation as a potential mechanism.

Internal intergranular oxidation is a well-supported mechanism for PWSCC of nickel alloys. The model was first proposed by Scott and Le Calvar [27] and received support from surface embrittlement studies done in steam and hydrogen at 400°C [29]. Scenini et al. [50, 56] extended the studies at 400°C, and also exposed Alloys 600 and 690 to a steam and hydrogen environment at 480°C and atmospheric pressure; in all cases they found that chromium was internally oxidized and this caused the expulsion of metallic nickel nodules on the surface [50]. This kind of environment is believed to reproduce the selective oxidation phenomenon that occurs during PWSCC.

The internal oxidation mechanism involves the ingress of oxygen into the alloy. Assuming the conditions are below the dissociation pressure of the solvent metal, the oxidation occurs with a minor alloying element in the material leaving the main solvent material untouched. This is a generalized problem for nickel alloys at low partial pressures of oxygen, whether at 300°C or 800°C, because minor alloying elements, such as chromium, can oxidize internally if they are present in insufficient amount, as in Alloy 600.

Dissimilar metal welds are prone to undergo dilution with parent materials. Dilution can change the composition of a weld significantly. Alloy 82 and 182 dissimilar welds with significant dilution of iron-based alloys have greatly increased iron contents compared to literature [38];

As a result, iron rich external oxides have been found on Alloy 82 and 182 weld joints after exposure to primary water conditions [42].

In this study, two Alloy 82 dissimilar metal welds with parent materials of carbon steel and Alloy 600 were exposed in two separate simulated primary water environments:

- In an atmospheric reactor vessel in hydrogenated steam at 480ºC. Temperature was elevated to account for slow kinetics caused by low pressure.
- At high pressure in an autoclave vessel at 375ºC and 10.0 MPa total pressure.

Whilst one might rely on residual stress considerations to validate the performance of such welds, it is also useful to examine whether they have any inherent SCC resistance on grounds of the weld-metal chemistry (dilution or microstructure). I believe it is possible to support or counter the likelihood of PWSCC by studying weld chemistry and surface or internal oxidation using the internal oxidation model as a guide. This is accomplished by first examining the extent of dilution and microstructure of the weld before exposure. Following this, exposed weld samples are analysed for potential internal oxidation and/or the formation of external oxides due to changes in weld chemistry.

Chapter 3: Analytical Techniques Employed

3.1 Scanning Electron Microscopy (SEM)

The scanning electron microscope (SEM) was used for imaging of Alloy 82 weld samples both before and after exposure. The SEM was deemed a suitable option for topographical imaging of Alloy 82 weld samples down to a scale of 10 nm.

SEM image formation is reliant on the attainment of signals produced from the interaction between an electron beam and a sample [57]. For imaging, secondary electrons (SE) and backscattered electrons (BSE) are analyzed. SE's are more useful for topography while BSE's are more useful to understand the composition differences on different areas of the sample.

For this study, SE's were used to study the topography. SE's are emitted when the electron beam strikes the sample surface causing ionization of atoms in the sample. Loosely bound electrons may be emitted from the surface due to the increase in energy these are referred to as SEs [57]. SEs are emitted within a few nanometers of the surface giving topographical information with good resolution. These electrons are detected by the SE detector and a scintillator absorbs the incoming energy from the SE and converts it into photons. The photons then move through the specimen chamber and into a photomultiplier tube [57]. The photomultiplier converts the photons back into electrons and the output voltage from the photomultiplier tube is outputted as a brightness modulation on a CRT screen.

The Hitachi S-570 scanning electron microscope was used at a working distance of 15 mm and an accelerating voltage of 20 keV were used. The SEM was equipped with an EDX detector and had a resolution down to 10 nm.

3.2 Energy-Dispersive X-ray Spectroscopy (EDX)

Energy-dispersive X-ray spectroscopy (EDX) was used to determine the composition on the surface of samples before and after exposure. The EDX detector used on the Hitachi S-570 was not reliable for detecting weak X-ray signals emitted from lighter elements such as oxygen.

When a sample is bombarded with electrons a variety of signals are produced. SE's and BSE's are used for imaging (as discussed in Section 3.1). For EDX, the X-ray signals emitted are used to determine the composition on the surface of a sample. X-rays are produced when the electron

beam causes ionization of the atoms in the sample and an electron from an inner shell is ejected [58]. An electron from an outer shell fills the vacancy and an X-ray is emitted whose energy is equivalent to the difference in energies of the two orbitals. The shells are designated K, L, M, and N. They contain 1, 3, 5, and 7 sub-orbitals respectively [58].

X-ray energies are characterized by the shell which an electron vacancy originally occurs. For example, the K shell can be labeled K alpha or K beta. A K alpha X-ray occurs when an L shell electron fills a vacancy in the K shell and a K beta X-ray occurs when an M shell electron fills a vacancy in the K shell [58]. Beta peaks generally have a higher energy than alpha peaks but are smaller in signal intensity. The process of electron transitions becomes more complicated as you move into L, M, and N shell vacancies. For example, an L shell vacancy in any of the three sub orbitals can be filled by any of the electrons in the M shell (five sub-orbitals) or N shell (seven sub-orbitals) [58].

The X-ray energy emitted for each transition is designated to a unique element. The signal intensity of these X-ray energies is used to generate a spectrum describing the composition at the point of electron beam bombardment. The EDX detector used was incorporated in the Hitachi S-570 scanning electron microscope used for SEM.

3.3 Auger Electron Spectroscopy (AES)

Auger electron spectroscopy (AES) depth profiling was performed on Alloy 82 weld samples to determine the composition beneath the surface oxides after exposure and for more accurate detection of oxygen. Auger electron emissions are stronger than X-ray emissions for lighter elements, such as oxygen [59, 60]. Depth profiling makes use of sputtering the sample. Sputtering is the removal of a surface layer by bombarding the surface with ions. The incident ions increase the energy of atoms on the surface above the surface binding energy and the atoms are ejected.

The advantages of AES are high sensitivity for compositional analysis near the surface (approximately 0.5 nm – 2 nm deep), data acquisition speed, and its ability to detect all atoms above helium [59, 60]. A specimen atom bombarded by an electron beam will undergo ionization. An incident electron with sufficient energy can eject an electron from an inner shell, such as the K shell. This vacancy is filled by an electron from an outer shell orbital, such as an

electron from the first orbital in the L shell (L_1). The energy released from the transition is either released as an X-ray or transferred to another electron, such as one in the second orbital of the L shell, L_2. This electron is then ejected from the L_2 orbital as an Auger electron and designated KL_1L_2 [59, 60]. Several other similar transitions can occur such as KL_1L_1,KM_1M_2, etc. The Auger electron energy and intensities are unique to an element in the area being analyzed. It should be noted that AES is a technique which is done in ultra high vacuum 0.5 nm to 2 nm from the surface while EDX penetrates down to about 1 µm.

AES spectra is usually plotted on a kinetic energy scale since the kinetic energy of an Auger electron is independent of the type of primary beam (electrons or X-rays) [59, 60]. X-ray and Auger transition peaks differ by the photon energy [59, 60]. Therefore, any overlap in peaks can be overcome by changing the X-ray source from Mg-K_α to Al-K_α. The position of the XPS peaks will remain constant but the AES peaks will shift by 233 eV due to the change in photon energy between the two. In this study, an electron beam was used for Auger analysis instead of X-rays [59, 60].

AES depth profiling was performed using the PHI 660 Scanning Auger Microprobe at Surface Science Western. A 10 keV electron beam rastered over a small size (typically 100x100 µm) was used for this examination. Sputtering was performed using a 3 keV Ar^+ ion beam rastered over a 1 x 1 mm area. The sputter rate under these conditions was determined to be approximately 9.6 nm/min.

3.4 X-ray Photoelectron Spectroscopy (XPS)

X-ray photoelectron spectroscopy was used to determine elemental composition right at the surface of the Alloy 82 weld samples after exposure. XPS analysis is similar to AES in the sense that it is a shallow analysis which takes place at depths within 1 nm deep of the surface [60]. The analysis goes deeper (up to 5 µm) but there is an exponential decay of signal with added depth. The advantage of XPS analysis is the ability to determine different chemical states of elements present in a sample [59, 60].

XPS involves bombarding the surface with X-ray photons from Al-K_α or Mg-K_α sources. The X-ray photon excites an electron in an orbital causing ejection of the electron from an orbital in the inner shell, such as the 1s or 2p orbital. The XPS spectrometer measures the kinetic energy

of the ejected electron. This can then be used to determine the electron binding energy using equation 10 discovered by Ernest Rutherford.

$$E_{binding} = E_{photon} - (E_{kinetic} + \emptyset) \quad (10)$$

Where E_{Photon} is the energy of the X-ray photons, $E_{kinetic}$ is the kinetic energy of the emitted photoelectron and $\emptyset$ is the spectrometer work function from the spectrometer. The binding energy peaks are recorded versus the number of electrons recorded by the principal quantum number with the electron shell (1, 2, 3, etc.), the sub-orbital (s, p, or d) and the spin of the electron within the orbital (1/2 or 3/2). The binding energy of electrons ejected (i.e. 2p3/2) from each orbital peaks at different binding energies. Different chemical states have different binding energies. Depending on the intensity of the binding energies, the different states of elements can be identified.

XPS was done on the Thermo Scientific K-Alpha XPS spectrometer located at the University of Toronto. A monochromatic Al-K_α X-ray source was used, with a spot area of 400 μm.

Chapter 4: Metallurgical Analysis of Alloy 82

4.1 Welds Used

Figure 19 – an Alloy 82 dissimilar metal weld joint between parent materials of Alloy 600 and carbon steel (shown on the left). The weld was cut axially to reveal the cross-section of the weld (shown on the right).

Weld samples were taken from two Alloy 82 dissimilar metal welds. The two parent materials were Alloy 600 and carbon steel. The welds were cut to reveal the cross-section of the weld. Figure 19 is a weld, with both parent materials, and an axially cut portion of the weld used to create samples. The cross section of the weld was analyzed because PWSCC is a process in which crack propagation can occur through the cross section.

Figure 20 shows a typical weld sample after mechanical polishing and removal of carbon steel (a) and the different sections which the weld area can be split into (b). The root of the weld is the initial pass applied at very high temperature. Subsequent passes which follow are denoted as the filler. There is a portion of carbon steel present from the parent material in all weld samples. The carbon steel is located in the bottom right corner of the weld sample in Figure 20.

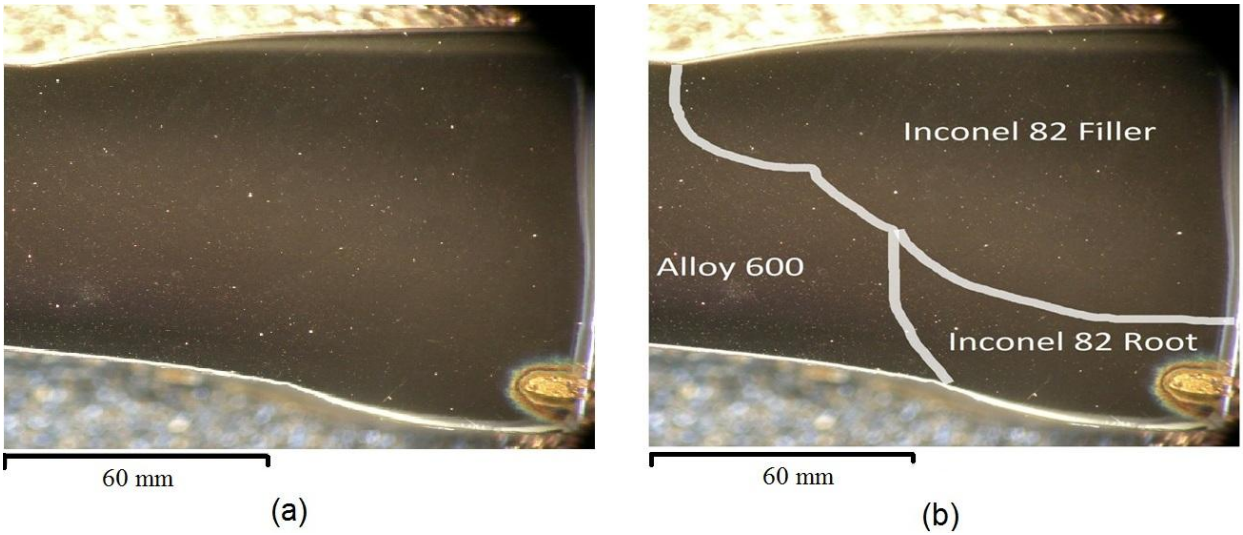

Figure 20 – A typical weld sample after mechanical polishing (a) with the 3 distinct regions shown in (b). A portion of carbon steel from the parent material is located in the lower right corner of the sample.

4.2 Microstructural Characteristics

The microstructural characteristics of welds are different from conventional alloys, such as Alloy 600. Welds are not cold rolled or annealed after solidification. This produces a dendritic structure rather than compact grains. The differences in microstructure can impact the PWSCC susceptibility of welds.

4.2.1 Dendritic Structure

Dendrites are the tree-like growth of crystals during solidification of a liquefied metal. The crystals initiate nucleation at numerous positions in the weld and grow in varying directions. Eventually, dendrites intersect which halts further growth. The result is a microstructure with dendrites that have grown in varying directions. Inter-dendritic stress corrosion cracking (IDSCC) occurs where two dendrites intersect [33, 43, 44]; this is due to the large grains at the point of intersection.

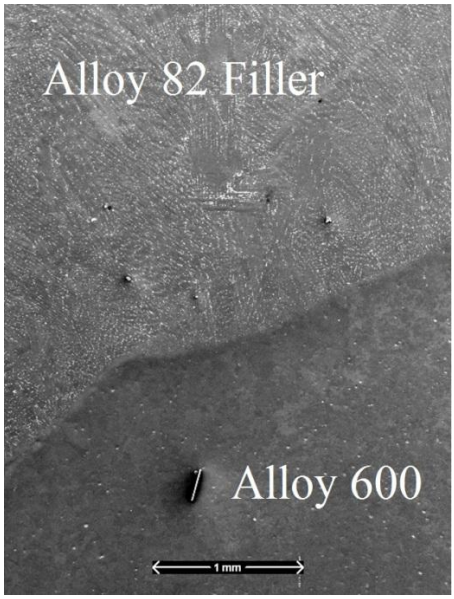

Figure 21 – The border between the Alloy 82 weld and a parent material, Alloy 600 - Alloy 82 has a dendritic structure.

Alloy 600 does not have a dendritic structure. Once solidified, Alloy 600 undergoes a series of refinement steps including rolling, annealing, and thermal treatment which remove dendrites. Figure 21 is an Alloy 82 weld samples (top) with the parent material, Alloy 600 (bottom). Even at the relatively low magnification in Figure 21, Alloy 82 clearly has a dendritic structure.

Figure 22 further magnifies a region in the Alloy 82 filler. As mentioned, nucleation occurs at numerous positions during solidification depending on the direction of heat flow. The direction of dendrite growth is different depending on where nucleation initiates. Figure 22 illustrates the possible tree-like growth of different dendrites. Unlike welds, alloys are given the opportunity to slowly recrystallize which helps to greatly reduce the presence of compositional variations associated with dendrites. It is important to distinguish between dendrites and grain boundaries. Figure 22 shows dendrites as ripples growing in different directions while grains have many white inclusions which represent carbides residing along grain boundaries. The grains are larger than those in Alloy 600. Also, the heat affected zone has enlarged grain size. Previous studies have indicated that the grain boundaries where two dendrites intersect are the most susceptible to PWSCC [33, 43, 44].

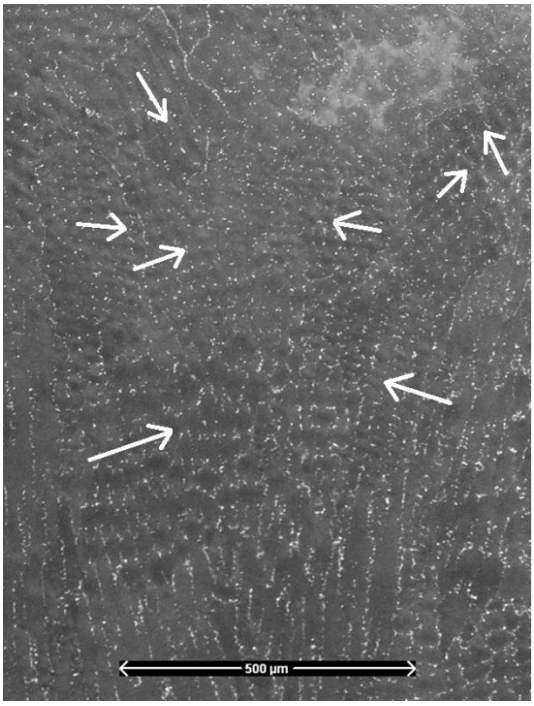

Figure 22 – SEM image of the Alloy 82 filler material before exposure at 100x magnification. The filler shows signs of dendritic growth in many directions (some outlined in red).

4.2.2 Grain Boundaries and Carbide Inclusions

Carbide inclusions were noticed on the surface of the Alloy 82 weld samples. Niobium carbide inclusions were formed along grain boundaries, while titanium carbide inclusions were distributed within grains randomly. Figure 23 is SEM images of the grain boundaries in the Alloy 82 filler at two different magnifications. EDX spectra confirming the composition of carbides as titanium or niobium can be found in Appendix A.

Alloy 82 deliberately contains an elevated niobium content which promotes the formation of niobium carbides at high temperatures during welding. Niobium and titanium are added to nickel-based alloys to reduce the formation of chromium carbides at grain boundaries. Chromium carbides reduce the chromium content around grain boundaries. Previously, it was thought that the chromium depletion would increase the susceptibility of nickel alloys to PWSCC under primary water conditions. However, studies have indicated that chromium carbide formation increases PWSCC resistance under these conditions.

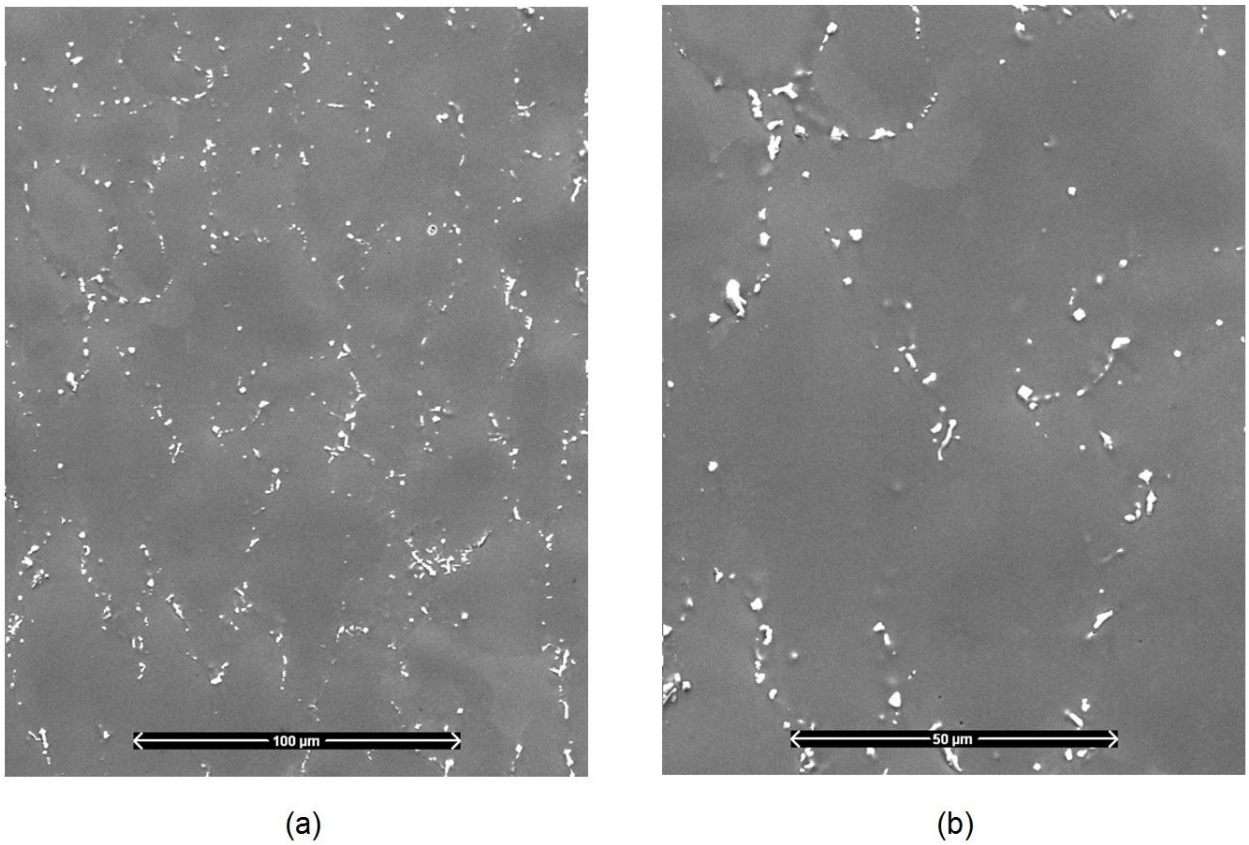

Figure 23 – SEM images of niobium carbides along the grain boundaries of an Alloy 82 weld at 500x magnification (a) and 1000x magnification (b)

4.3 Composition Variations

The composition is non-homogeneous throughout the weld. Elements crystallize by segregating either to the forming solid or to the remaining liquid. This can lead to areas with an elevated composition of a minor or major element in the weld. Dilution also plays a significant role in weld compositional variations across the weld. The composition of Alloy 82, from literature, is given in Table 1. Literature suggests that Alloy 82 contains only 3.0% iron. Given that one parent material of the dissimilar metal weld studied is carbon steel, it is possible that the composition of iron and chromium in the weld could change significantly as a result of dilution.

4.3.1 Dilution

Figure 24 (b) is the composition profile of an Alloy 82 weld, from EDX analysis, along the cross-section of the weld in the y-direction (shown in (a)). As expected, there is an elevated iron content near the carbon steel parent material. Furthermore, as a result of dilution nickel and

chromium are greatly depleted in the root of the weld. The composition across the root and filler of the weld shows minimal variation in the x direction. Compositional trends in the x-direction can be found in Appendix A.

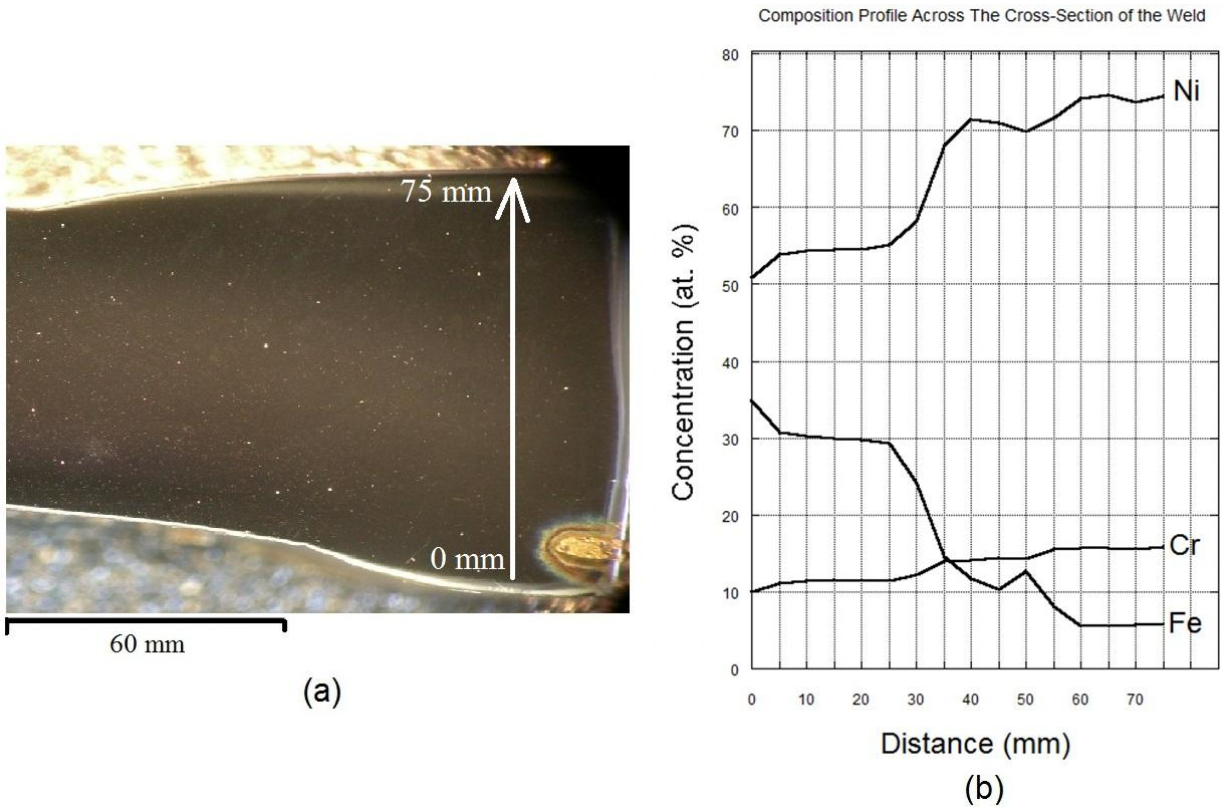

Figure 24 – The composition trend (b) across the cross section of an Alloy 82 weld (a) for Ni, Cr, and Fe. Iron is particularly elevated in the root portion of the weld (near 35%).

The root of the weld is the point of exposure to primary water during plant operation. The elevated iron content could promote the formation of an external iron oxide film; external iron oxide films have been noted previously in Alloy 82 welds but elevated iron content due to composition variations was not credited [12, 38, 42]. Dilution had to be present because forming a protective external iron oxide film of magnetite, Fe_3O_4, with only the 3.0% Fe content in Alloy 82 is unlikely.

Depletion in chromium is noticed throughout the weld. There are rare patches where the chromium content peaks at 18% in the filler, but normally the content does not exceed 16% in the filler and 12% in the root. This could promote internal oxidation of chromium throughout the entire weld cross-section. Theoretically, the root could undergo internal oxidation of

chromium before an external oxide of iron is formed depending on the flux of chromium and iron diffusing to the surface.

4.3.2 Comparison to Alloy 800

Alloy 800 is a nickel-based alloy containing a high percentage of iron and chromium compared to Alloy 600. A comparison of Alloy 800 to the Alloy 82 welds used, in this study, is given in Table 4. Alloy 800 is known to be immune to PWSCC. This can be attributed to the formation of a protective iron oxide film, Fe_3O_4, and/or a protective chromium oxide film, Cr_2O_3. The Alloy 82 welds contain a similar amount of iron as Alloy 800 but far less chromium.

Table 4 – Comparison of Alloy 800 to the root of the Alloy 82 weld

Alloy	Ni	Fe	Cr
Alloy 82 Root	53%	34%	13%
Alloy 800	30% - 35%	39.5% min.	19% - 23%

It is possible for a protective iron oxide film of Fe_3O_4 to form on the surface of the weld. However, the chromium content is significantly lower which indicates a potential susceptibility to PWSCC by internal oxidation embrittlement. Similar diluted dissimilar metal welds have shown to be less susceptible to PWSCC than Alloy 600 [12, 38]. Also, there have been indications that increasing the hydrogen content can promote the formation of a compact iron oxide film on Alloy 82. One can hypothesize that the PWSCC susceptibility of Alloy 82 would be somewhere between the susceptibility of Alloy 600 and Alloy 800 due to the unique combination of iron and chromium in Alloy 82 dissimilar metal welds.

Chapter 5: Low Pressure Exposure to Hydrogenated Steam at 480ºC

5.1 Experimental Details

Alloy 82 weld samples were exposed to hydrogenated steam at Surface Science Western under the supervision of Dr. Sridhar Ramamurthy. The exposures were similar to those performed by Scenini et al. on Alloys 600 and 690 [50]. The exposures were performed in a tube reactor, placed in a furnace, at 480°C and atmospheric pressure. The reactor was based on the design used by Scenini et al. The reactor had to be built, using available parts and tubing, at Surface Science Western prior to any exposures.

Only hydrogen and steam were present in the tube during experiments. The hydrogen partial pressure and steam flow rate were varied to maintain conditions slightly above or below the Ni/NiO dissociation pressure. The partial pressure of oxygen is dependent upon the dissociation of steam into hydrogen and oxygen. By controlling the ratio of steam to hydrogen, the partial pressure of oxygen was controlled. Calculations demonstrating how this is done can be found in Appendix B.

5.1.1 Sample Preparation

The Alloy 82 weld samples were machine-cut to reveal the cross-section of the weld and remove carbon steel. The Alloy 600 portion of the parent material was retained. The cross-section of the weld was mechanically polished with silicon carbide grit paper (400, 800, and 1200 grit) and diamond paste (9 μm, 6 μm, 3 μm, 1 μm, and 0.05 μm).

After each polishing stage, the samples were washed with deionized water, ultrasonically cleaned in ethanol for 7 minutes, and air dried. The samples were checked for scratches using optical microscopes after each stage. Upon completion of polishing, samples were kept in a desiccator.

5.1.2 Description of System and Operating Procedure

The heart of the system is a tube reactor enclosed in a furnace. The furnace is unable to encase the entire tube and Variacs attached to high temperature heater tapes are used to heat exposed areas of the tube. Argon gas is used to purge the system of air before embarking on

experiments. The system is continuous, with hydrogenated steam being refreshed constantly. Water fed to the system is de-ionized and this is maintained throughout the experiment. Steam and hydrogen are pre-mixed in a stainless steel block before entering the reactor. Upon exit from the reactor, the hydrogenated steam is separated into hydrogen and water by way of a condenser. The hydrogen is combusted using methane in a fume hood while condensed water is collected in a beaker.

There are some flaws in the system which could impact experiment performance. Water is fed drop-wise to the reactor by a peristaltic pump. This means the amount of steam in the system fluctuates constantly. The rate of steam inputted to the reactor is an average throughout the experiment. The heating tape used to heat the exposed portion of the tube is not maintained above temperatures of 150ºC due to safety concerns. Initially, the low temperature of the exposed tube portion causes small amounts of condensed water along the exposed tube. However, within 2 hours all water in the system is present as steam and the samples in the middle of the tube are always exposed exclusively to hydrogenated steam.

Figure 25 is a schematic of the atmospheric reactor. The operating procedure is as follows:

1. The quartz tube was removed and cleaned using acetone and deionized water. Samples were placed in the centre of the tube and all connections were tightened. The tube was then capped at both ends.
2. The reactor was heated to a controlled temperature of 480 °C. The stainless steel block was heated to approximately 300 °C. While heating, the air in the tube was purged using argon gas for 1 hour followed by hydrogen gas for 1 hour.
3. Once the reactor reached 480 °C, the peristaltic pump was started and steam was fed to the 300ºC heating block. The steam takes approximately 15 minutes to pump from the peristaltic pump into the heating block and reach the reactor.
4. After exposure, the heating and pump were turned off. The reactor was allowed to cool and the samples then removed for analysis.

Calculations to determine the flow rate of water required and the partial pressures of hydrogen and oxygen relative to the Ni/NiO dissociation pressure can be found in Appendix B. This was done using methods similar to those described in section 1.3 and by Scenini et al [50].

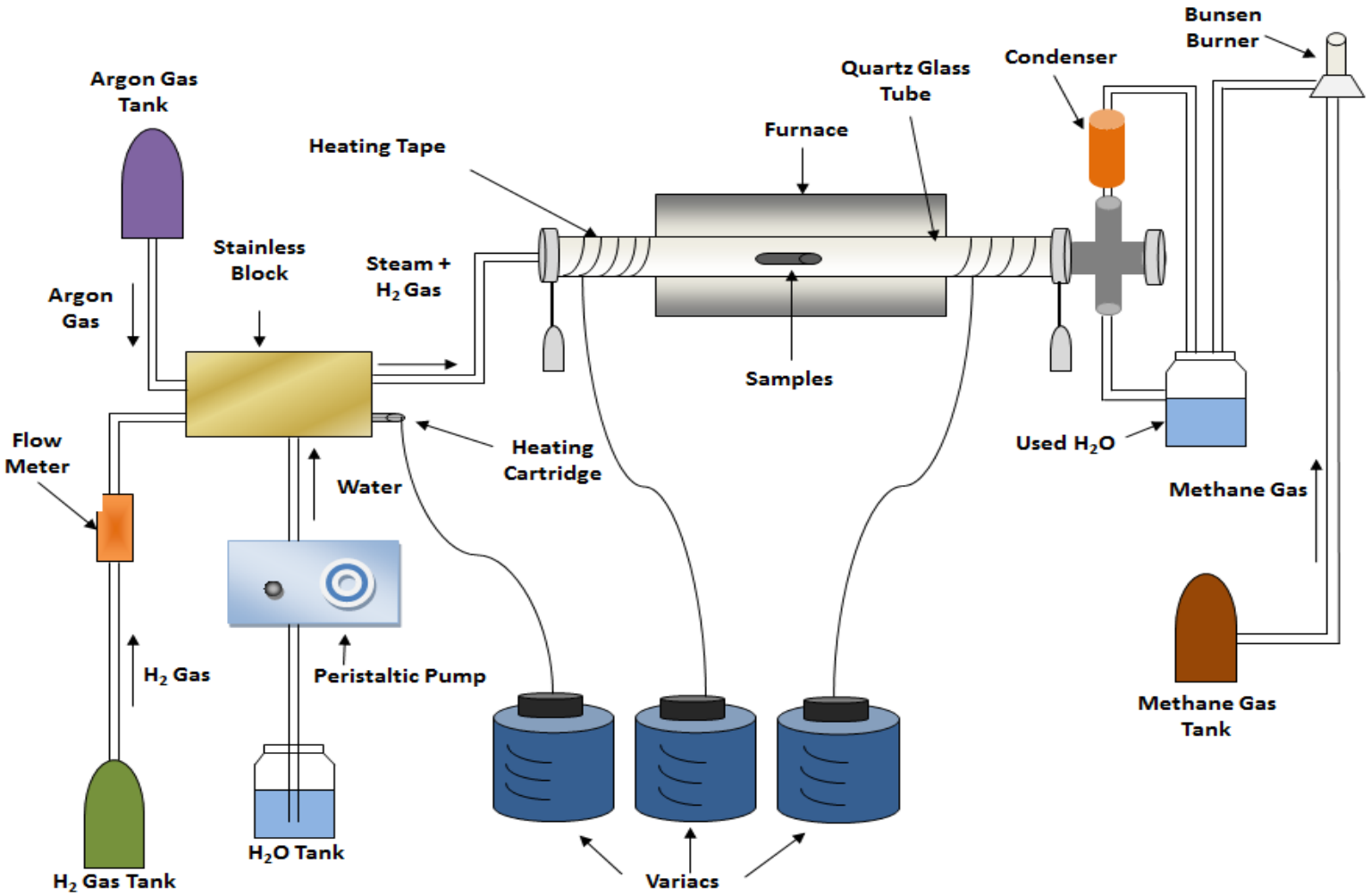

Figure 25 – Atmospheric-Pressure Reactor

5.1.3 Sample Removal and Storage

Samples were removed from the reactor vessel and immediately placed in a desiccator. The samples were shipped to the University of Toronto in sealed plastic bags. Once received, samples were placed in a desiccator until analyzed by SEM or EDX. Any necessary analysis was performed within three weeks of sample arrival.

Samples requiring AES analysis were kept in a vacuum desiccator until analyzed at Surface Science Western. Samples requiring XPS analysis were kept in an argon filled container immediately after exposure and transported to the University of Toronto. This was done to limit the amount of carbon on the surface which could introduce error in XPS and/or AES results.

5.1.4 List of Experiments Performed

Table 5 is a list of experiments performed in the atmospheric-pressure reactor. Temperature was maintained at 480ºC for all experiments. Newman [61] had indicated that the oxidation, or not, of Ni would not respect the Ni/NiO dissociation pressure at lower temperatures and atmospheric pressure which was evident in experiments done by Scenini et al. at 400ºC [50, 61]. The temperature was increased to 480ºC to counteract the slow kinetics caused by low pressure.

Table 5 – List of experiments performed at 480ºC and 1 atmosphere at Surface Science Western. Weld samples from two Alloy 82 welds were exposed.

Test #	Duration (h)	Steam/Hydrogen Ratio ($R_{H2O/H2}$)	P_{O2} (bar)	Distance from Ni/NiO Dissociation Pressure
1	72	62	9.72×10^{-26}	30 times below
2	72	100	2.53×10^{-25}	10 times below
3	72	345	3.04×10^{-24}	At or slightly above
4	120	62	9.72×10^{-26}	30 times below
5	120	100	2.53×10^{-25}	10 times below

The experiments performed in Table 5 are all done at 480ºC and 1 atmosphere total pressure. The steam/hydrogen ratio, partial pressure of O_2, and the distance from the dissociation Ni/NiO partial pressure of O_2 ($P_{O2, Ni/NiO}$) are given; the calculation of each of these variables is given in detail in Appendix B. It should be noted that all experiments were run well above the dissociation pressures for the Fe/Fe_3O_4 and Cr/Cr_2O_3 equilibria. Experiments 1, 2 and 3 were performed with only the first weld acquired. The remaining two were performed with samples from both welds. All experiments were performed slightly below the Ni/NiO dissociation pressure, except experiment 3 which was done slightly above.

5.2 Results

Weld samples were exposed for 3 or 5 days for 5 total experiments. Samples exposed for the same time interval exhibited similar oxidation macroscopically and microscopically. One sample was exposed in experiments 1, 2 and 3 while two samples (one from each weld) were exposed in experiments 4 and 5. Figure 26 is typical weld samples after exposure for three days (a) and five days (b). Samples from both Alloy 82 welds showed similar oxidation. The Alloy 82 root had an external oxide for all experiments performed. The filler of the welds had a snake-like external oxide across the cross-section of the weld. It is possible that areas without any external oxide (i.e. the filler) may have undergone internal oxidation. Welds were analyzed using SEM, EDX, AES, and XPS analytical techniques.

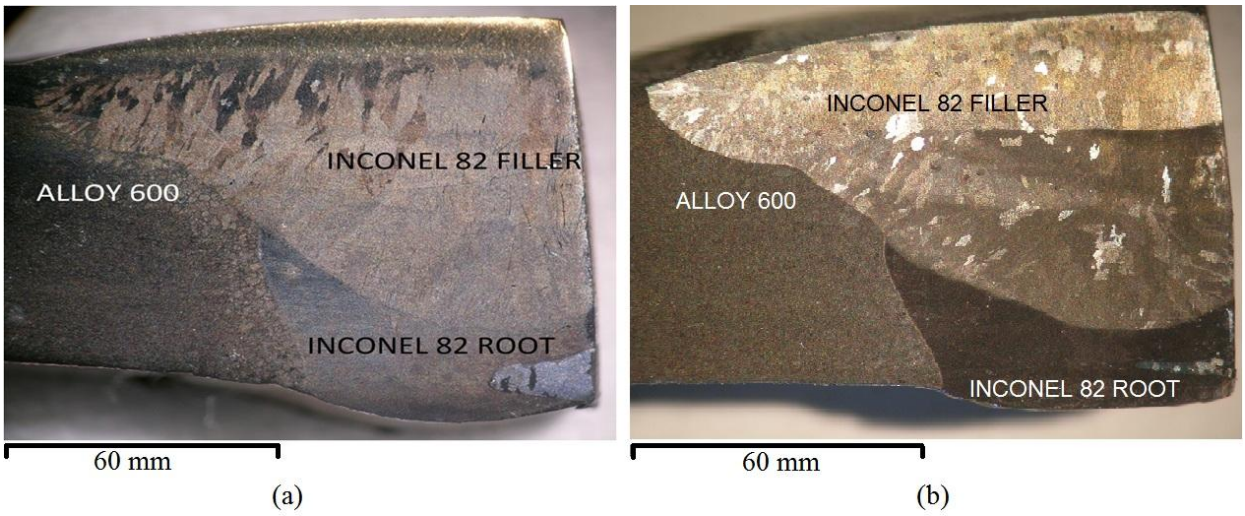

Figure 26 – Typical exposed weld samples after exposure in the atmospheric reactor below the Ni/NiO dissociation pressure after three days (experiment #2) (a) and five days (experiment #5) (b).

5.2.1 SEM and EDX Analysis

5.2.1.1 Analysis below the Ni/NiO Dissociation Pressure after 3 Days

SEM images of a typical Alloy 82 weld after exposure for 3 days are given in Figure 27 (b) and (d) with Figure 26 (a) and (c) indicating where the pictures were taken on the weld sample. Results for all 3 day exposures were very similar. The root of the weld (b) had small particles while the filler had large neatly spaced spherical nodules with areas in between without nodules (d). The initial hypothesis was that the nodules in the filler were pure nickel, similar to those observed by Scenini et al. on Alloy 600 [50]. This would indicate internal oxidation of chromium in the filler portion of the weld. The root of the weld appears to have a dark external oxide film with much smaller nodules or particles.

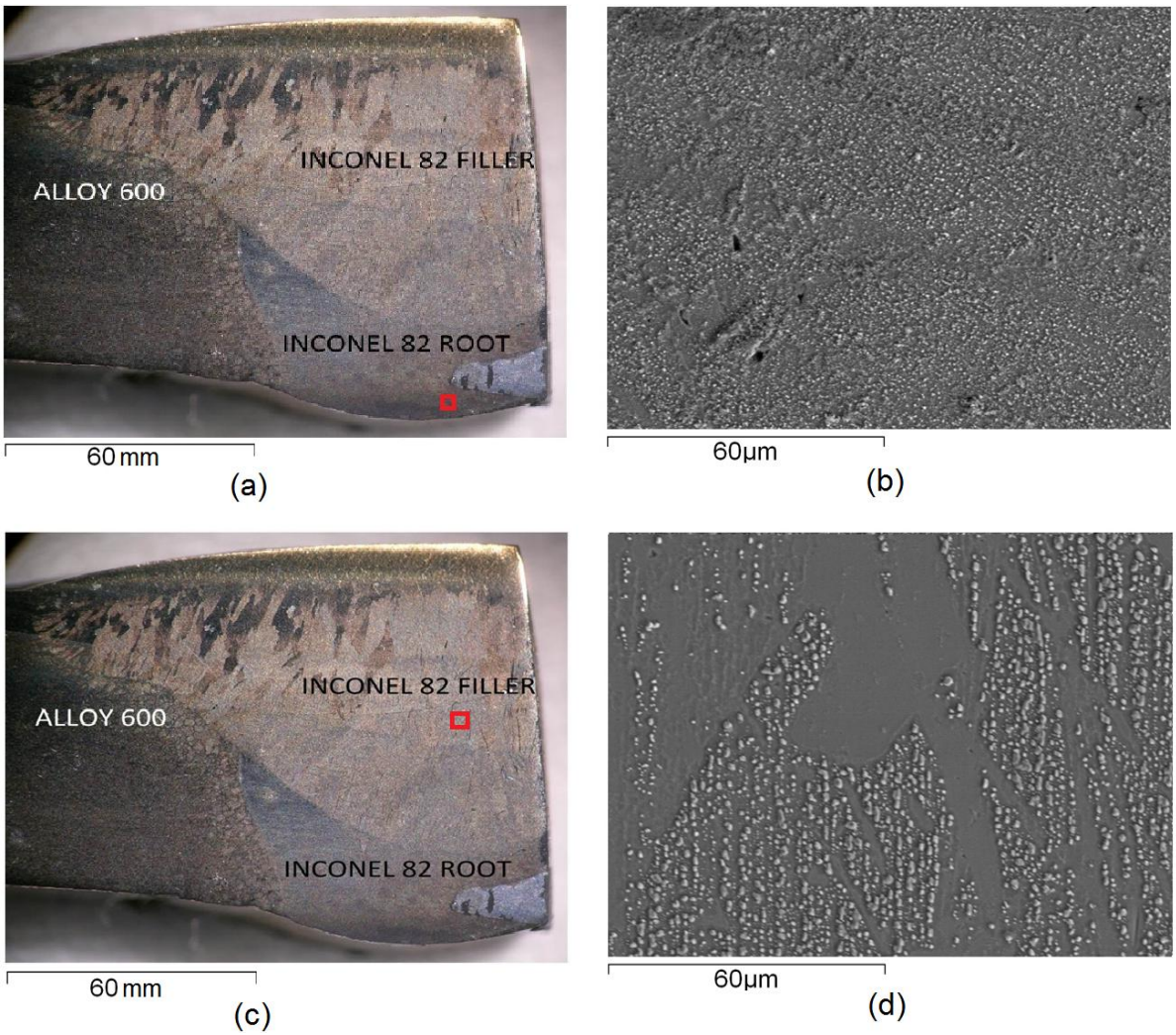

Figure 27 – SEM images of the root (a, b) and the filler (c, d) regions of the Alloy 82 weld

EDX analysis was performed to confirm the presence of nickel nodules on the filler and to characterize the oxide present on the root. Table 6 lists the results from EDX, with the EDX spectra given in Appendix A. The large spherical nodules in the filler are primarily composed of nickel. The EDX results for the root indicate elevated iron and nickel. However, EDX equipment was not available to accurately detect oxygen (although this was attempted as shown in Table 6). In order to characterize the oxide formed on the root (if any), AES and XPS analysis was performed.

Table 6 - EDX results for nodules and around nodules in the root (b) and filler (d) in at. %

Region	Ni	Fe	Cr	Mn, Ti, Nb, Al, Si	O
Small Nodules in Fig. 25 (b)	51.4	24.2	9.80	9.01	Bal.
Around Small Nodules in (b)	51.4	34.3	11.5	Bal.	-
Large Nodules in Fig. 25 (d)	85.3	3.63	5.01	2.05	Bal.
Around Large Nodules in (d)	64.7	15.1	15.4	Bal.	-

5.2.1.2 Analysis below the Ni/NiO Dissociation Pressure after 5 Days

SEM images are given in Figure 28 for the Alloy 82 weld after exposure for five days in the atmospheric pressure reactor. Figure 28 (a) indicates the region of the weld which each SEM image is taken (designated region 1, 2 or 3). The results after five days are different from those after three days. Table 7 presents the EDX analysis which was performed to determine the composition of the layer in region 3, the nodules in region 2, and the composition of the oxide formed in region 1. EDX spectra for Table 7 are given in Appendix A.

The root, region 1, has a snake-like oxide with small nodules in between. The region between the root and the edge of the filler, region 2, is similar to that of Figure 27 (d) with large spherical nickel nodules. The edge of the filler, region 3, indicates that additional internal oxidation may have occurred which resulted in a high quantity of nickel expulsion such that it almost forms a layer on the exposed sample.

Table 7 - EDX results the nickel layer, nickel nodules, and oxide in Figure 27. Compositions are given in at. %.

Region	Ni	Fe	Cr	Mn, Ti, Nb, Al, Si
Region 3 Nickel Layer	93.8	2.96	2.66	0.50
Region 2 Nickel Nodules	90.8	3.51	5.06	0.62
Region 1 Oxide	33.1	53.3	7.46	6.06
Region 1 areas within Oxide	67.8	27.3	2.76	1.69

The results from SEM and EDX after five days indicate the amount of internal oxidation occurring in the filler has increased. This was similar for experiments 4 and 5. Furthermore, the oxide film on the root looks remarkably different after five days. EDX analysis is unable to successfully characterize the oxide due to limitations accessing proper EDX equipment.

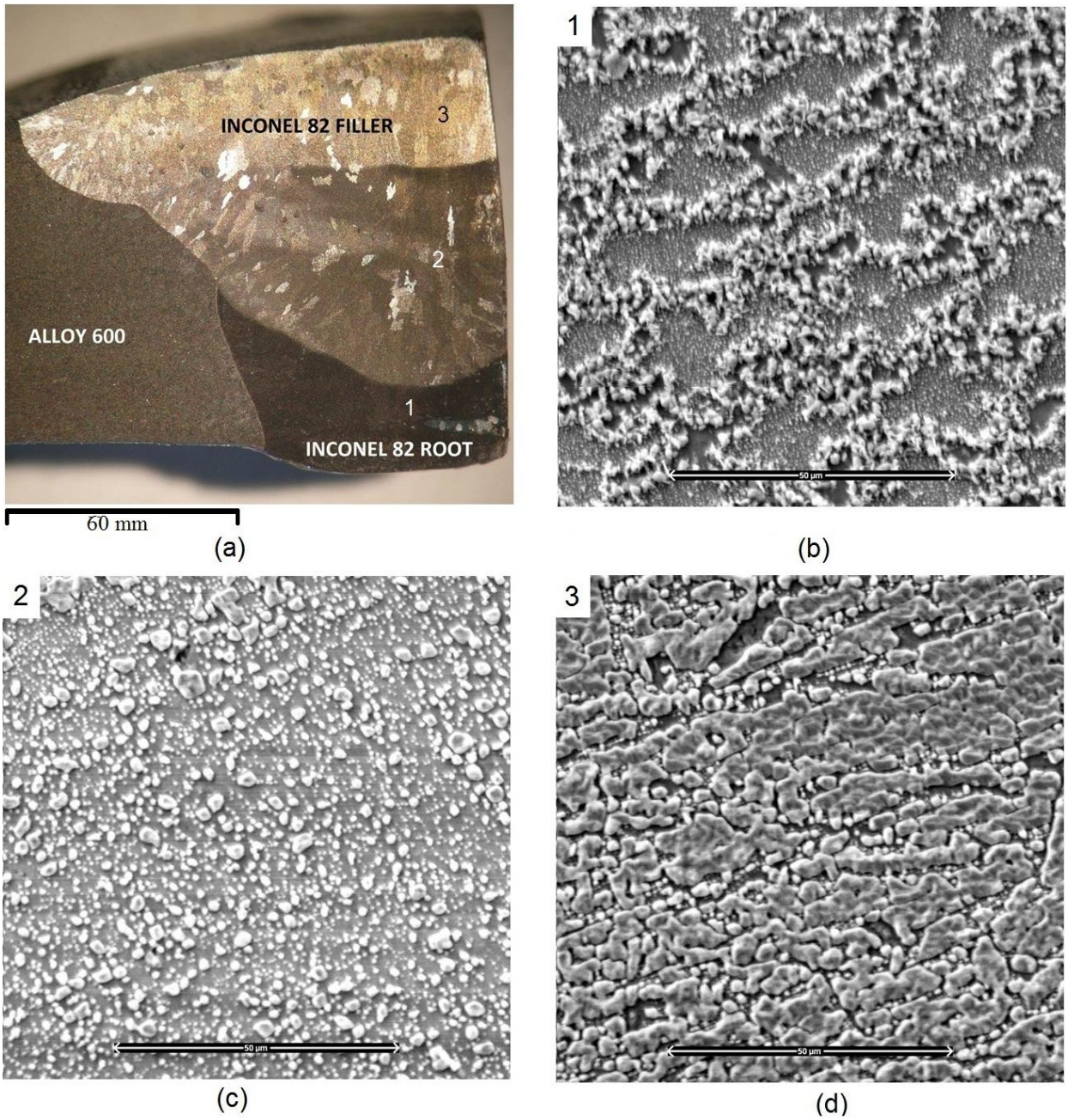

Figure 28 – Exposed weld after five days (a) with SEM images of the root (b, region 1), between the root and the filler (c, region 2) and the edge of the filler (d, region 3).

5.2.2 AES Analysis

Figure 29 is an Auger Electron Spectroscopy (AES) depth analysis which was performed on exposed weld samples. The 3 graphs (Figure 29, b, c, and d) are associated with regions 1, 2, and 3 in Figure 29 (a).

The root, region 1, indicates the presence of an iron oxide, although it is difficult to characterize this oxide; this is because interpretation of the ratio of atomic percent of iron to oxygen does not equate to a particular iron oxide. The filler of the weld in regions 2 and 3 has similar results. There is a peak in nickel followed by a peak in oxygen and chromium. This would indicate the presence of internal oxidation expelling pure nickel to the surface with chromium oxidizing internally. The thickness of each layer is calculated and given in Table 8, assuming a sputter rate of approximately 9.6 nm/min. Regions 2 and 3 also have initial spikes in iron. This suggests that some of the iron oxidized externally in addition to internal or external oxidation of chromium.

Table 8 – Thickness of different layers on exposed Alloy 82 weld samples from AES

Region	Description of Layer	Approx. Thickness (µm)
1	Root Iron Oxide	0.4
2	Ni-Enrichment On Surface	0.4
2	Depth of Oxidation Below Ni-Enrichment	0.6
3	Ni-Enrichment On Surface	0.3
3	Depth of Oxidation Below Ni-Enrichment	0.7

AES results indicate that internal oxidation has occurred on the filler of exposed weld samples. The root has an external iron oxide which could form a protective layer if it is Fe_3O_4. However, the root contains significantly less chromium, due to dilution, and this may increase PWSCC susceptibility. The oxygen trend in region 1 does not suggest that chromium oxidized internally. However, it is possible to have both internal and external oxidation.

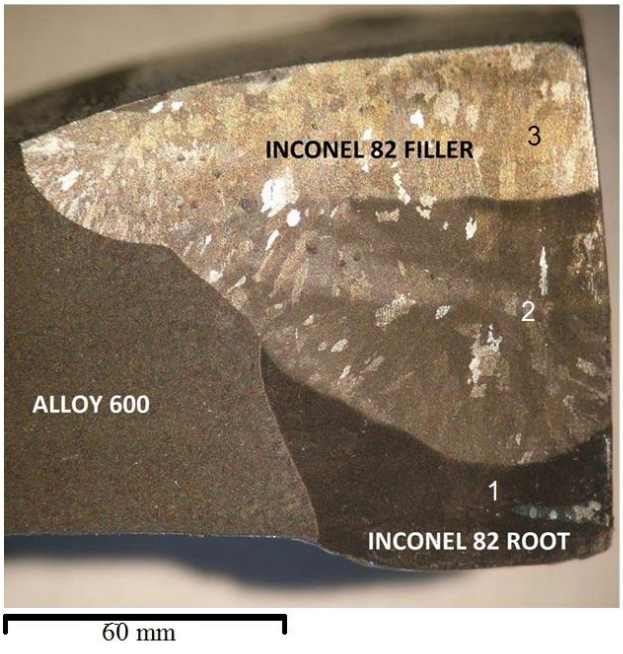

(a)

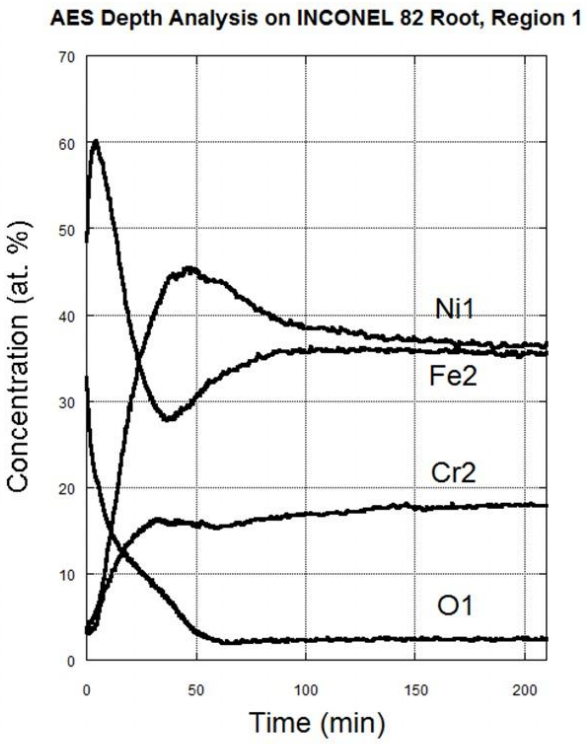

(b)

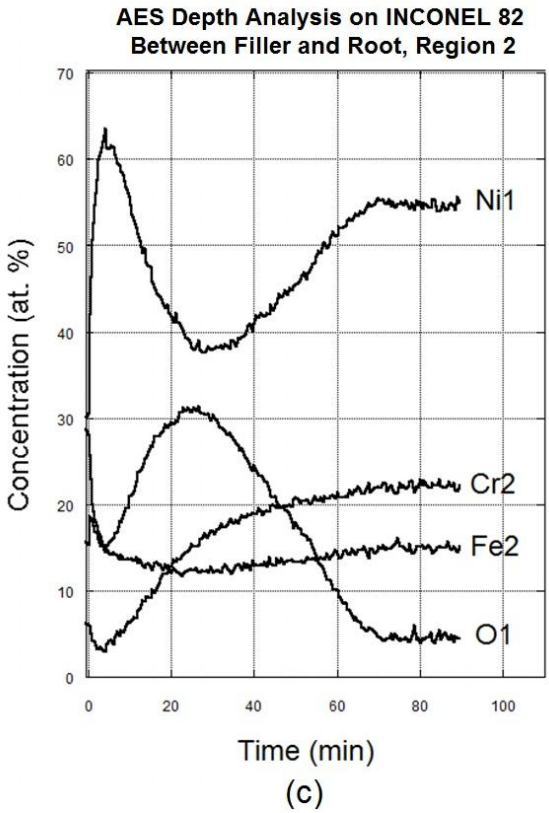

(c)

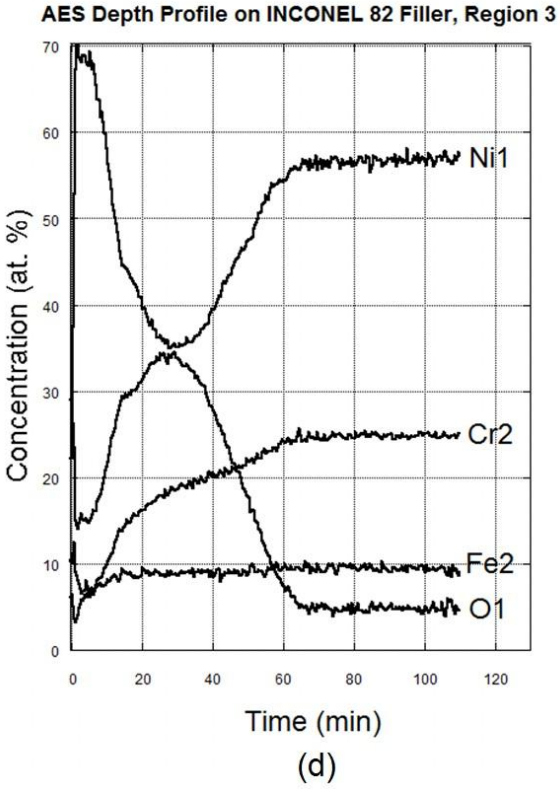

(d)

Figure 29 – AES results designated by region: root (1), middle of the filler (2), and filler edge (3)

5.2.3 XPS Analysis

XPS analysis was performed in an attempt to clarify which oxide of iron was present on the root of the exposed Alloy 82 welds. Samples were kept in an inert environment after exposure. This was done to limit the amount of carbon on the surface. XPS is an extremely sensitive surface analysis technique and the presence of carbon from the atmosphere can introduce error in results.

.

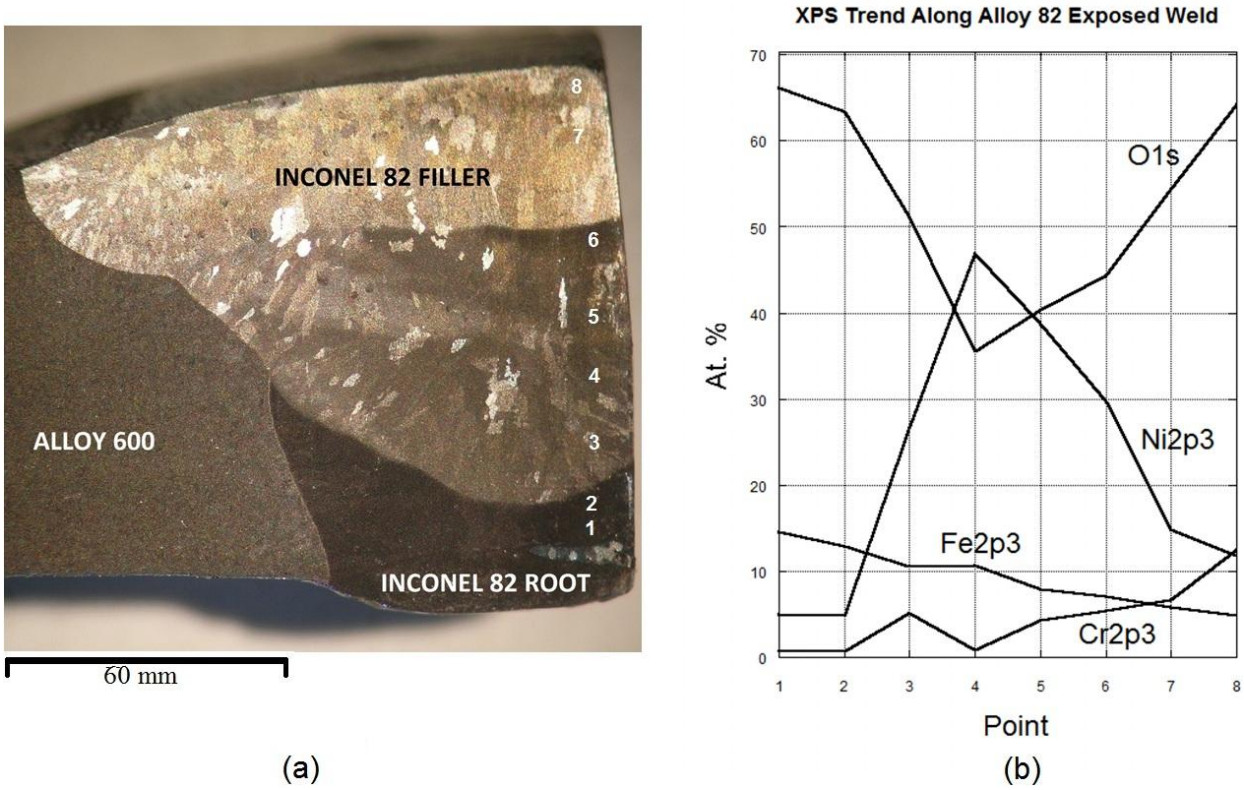

Figure 30 – XPS results showing the composition trends of oxygen, iron, chromium, and nickel

Figure 30 (b) is the composition trend from XPS of the total oxygen, iron, nickel and chromium along the surface of the exposed Alloy 82 weld in Figure 30 (a). These results are an overall summary quantifying how much of each element is present on the surface along the cross-section of the weld. Similar to EDX and AES analysis, there is an indication of a nickel enriched zone at the midpoint of the weld and the root of the weld may have an iron rich oxide. Points 5-8 indicate enrichment in oxygen and chromium. It is possible that there is external oxidation of chromium at the edge of the filler given that the composition reaches 18% Cr in some regions of this area.

XPS analysis was also performed on the as-received Alloy 82 weld samples to determine the chemical state of iron and nickel in those areas outlined in Figure 29 (a). The average peak binding energies from XPS analysis are given in Table 9 for nickel in the filler (point 4) and iron in the root (average of point 1 and 2). In addition, Dr. Rana Sodhi at Surface Interface Ontario suggested using the NIST X-ray Photoelectron Spectroscopy Database [62] to identify the potential element or oxide present at each peak; the element or oxide present is given in Table 9. The NIST X-ray Photoelectron Spectroscopy Database is a collection of previous studies which identified elements or compounds at different peak binding energies.

Table 9 – Identification of oxides or elements on the surface of the root (iron) and filler (nickel) on the Alloy 82 weld samples using the NIST X-ray Photoelectron Spectroscopy Database [62]

Element	Binding Energy Peaks (eV)	Identified element or compound	Atomic %
Nickel	852.50	Ni	43.03
	853.93	Ni	37.88
	857.61	NiO	18.95
	860.78	Unidentified	0.14
Iron	710.25	Fe_3O_4	60.77
	712.47	$FeCr_2O_4$	21.11
	715.16	Unidentified	9.12
	719.13	Unidentified	18.12

The unidentified peaks in Table 9 were identified as organometallic compounds in the NIST X-ray Photoelectron Spectroscopy Database. Only the oxides of importance were identified. The filler was identified as having a layer on the surface with 80% pure nickel and only 20% nickel oxide. This finding confirms that internal oxidation of chromium occurred causing the expulsion of pure nickel to the surface. The oxide on the root of the weld is composed of a mixed oxide of magnetite, Fe_3O_4, and $FeCr_2O_4$. The oxide on the root could potentially be

protective. However, internal oxidation may have taken place prior to the formation of the mixed external iron oxide due to the low chromium content.

5.3 Internal Oxidation of Alloy 82

Results indicate that the Alloy 82 filler undergoes internal oxidation. It should be noted that the root, and not the filler, is exposed during plant operation. According to Wagner theory, the flux of oxygen atoms diffusing into the filler must be greater than the chromium diffusing outward [47]. The abundant element, nickel, exposed to primary water conditions does not oxidize rapidly given the partial pressure of H_2. Internal oxidation at these temperatures occurs preferentially along grain boundaries. Oxidation along grain boundaries can lead to oxygen embrittlement and has been noticed frequently in nickel superalloys [26].

The results of this study support the internal oxidation model as observed previously [23, 27-30, 52]. The internal oxidation observed on the Alloy 82 filler is similar to the Ag-In system observed by Rapp et al.; the difference between the two studies is the Ag nodules tended to appear intragranularly for the Ag-In system [23]. This was due to intragranular diffusion through dislocations being dominant at temperatures of 700ºC. Increased temperature caused additional atomic vibrations in the lattice which increased the amount of dislocations available. At lower temperatures, intergranular diffusion dominates and nodules tend to form near grain boundaries. This was observed by Scenini et al. on Alloy 600 [50]. The Alloy 82 filler underwent similar internal oxidation. The internal stress caused by the internal oxidation of Cr caused Ni nodules to be expelled to the surface by a combination of diffusion and mechanical action. XPS results indicate that the edge of the filler may have an external chromium oxide. The chromium content at the edge of the filler is in excess of 18% at the filler edge which is greater than the 16% chromium content threshold needed to undergo transition from internal to external oxide.

The depth of oxygen penetration for all exposures was approximately 0.5-0.7 μm. Chromium carbides inhibiting further oxygen ingress was an initial assumption. Several studies indicate that chromium carbides have the potential to increase PWSCC resistance [4-7]. Chromium carbides tend to inhibit oxygen ingress along grain boundaries due to the formation of protective Cr_2O_3. However, further analysis of the Alloy 82 welds indicated a large percentage of niobium and titanium. These two metals are added to welds to form carbides which would reduce or

eliminate chromium carbides formed on grain boundaries. In this study, only niobium carbides were present along grain boundaries (see Section 4.2.2). One possible reason for the halt in oxygen penetration is the system becoming limited by kinetics of Cr_2O_3 formation. Another plausible reason is given by Gendron et al. Gendron found that oxygen penetrated to a critical depth of approximately 1 µm along brittle cracks in Alloy 600 at 400ºC [28]. At the critical depth, a healing layer of Cr_2O_3 is formed which prevents further ingress of oxygen.

Similar internal oxidation is observed on the root of the weld, but as much smaller nodules. This indicates that the volume of internally oxidized chromium is significantly less. The root has greater iron content than the filler which promotes the formation of an external iron oxide. AES indicates the depth of oxygen penetration in the root to be less than in the filler (Table 8). Also, EDX and XPS analysis indicate that the surface of the root has an external oxide consisting primarily of magnetite, Fe_3O_4.

5.4 External Oxidation of Alloy 82 Root

5.4.1 Potential for Oxide Film Protection

The three major constituents of Alloy 82, nickel, iron, and chromium, are present in varying quantities throughout the weld. This is primarily caused by dilution of carbon steel. The greatest dilution occurs in the root of the weld. The iron content is approximately 12 times the amount stated in literature. In addition, nickel and chromium are greatly depleted. This comparison is shown in Table 10.

Table 10 – Comparison of Alloy 82 composition from literature to actual (in root)

Alloy 82 Composition	Ni	Fe	Cr
Literature	67.0% minimum	3.0% Maximum	18.0% - 22.0%
Actual – In root (EDX)	53%	34%	13%

The extent of dilution of iron from carbon steel is significant. It is possible, under PWSCC conditions, to form an external iron oxide film. However, chromium is greatly depleted. Such low percentages of chromium would promote internal oxidation in the root. Diluted dissimilar welds have been found to be more PWSCC resistant. Fukumura et al. determined that dissimilar

welds between Alloy 600 and 316 stainless steel have a crack growth rate one order of magnitude smaller than similar welds between Alloy 600 [38]. These results indicate that the external oxide could potentially be protective.

The oxide formed is apparent in SEM imagery (Figure 28 (b)). It appears to be an iron oxide with small nodules (compared to the filler). AES and XPS analysis confirm the presence of an iron oxide on the surface of the root. XPS further determines the chemical state of the oxides present. The primary iron oxide in the root is magnetite, Fe_3O_4, which is protective in alloys such as carbon steel. The small nodules are elevated in Ni, which may indicate internal oxidation of chromium expelling pure Ni to the surface. It is possible that the nodules (similar to the filler) form first then there is a delay followed by the formation of an imperfect healing iron oxide layer. The iron oxide formed could crack and allow for PWSCC. The potential of external oxides to be protective can be measured by the Pilling-Bedworth ratio, R_{PB}: [52]

$$R_{PB} = \frac{V_{oxide}}{V_{metal}} = \frac{M_{oxide} \cdot \rho_{metal}}{n \cdot M_{metal}\rho_{oxide}} = \frac{231.54\ \frac{g}{mol} \cdot 8.33\ \frac{g}{cm^3}}{3 \cdot 55.7\ \frac{g}{mol} \cdot 5.50\ \frac{g}{cm^3}} = 2.10$$

An R_{PB} greater than 2 indicates that the metal oxide is initially protective but does not adhere to the surface properly due to volume expansion and eventually cracks due to compressive stresses. An R_{PB} less than 2 indicates that the metal oxide is protective. The magnetite, Fe_3O_4, present on the root has an R_{PB} just above 2. Given the large variation across the root of the weld, it is possible that a protective oxide does form on some parts which increase PWSCC resistance. However, the chromium content is below that which would form an external oxide. Internal oxidation of chromium could occur first expelling pure nickel nodules. This would be followed by the formation of the iron oxide healing layer which would make the root of the weld more susceptible to PWSCC. Also, the R_{PB} calculated does not take into account the other oxides formed on the root as found in XPS (see Section 5.2.3).

5.4.2 Comparisons to Alloy 800

The increase in Fe content in the root causes dissimilar welds of Alloy 82 between carbon steel (or stainless steel) and Alloy 600 to be comparable to Alloy 800 in some respects. Alloy 800 is regarded as PWSCC immune and has elevated iron content compared to Alloys 600 and 690.

The comparison between Alloy 800 and the root of dissimilar metal welds of Alloy 82 is given in Table 11.

Table 11 – Comparison of Alloy 800 to the root of the Alloy 82 weld

Alloy	Ni	Fe	Cr
Alloy 82 Root	53%	34%	13%
Alloy 800	30% - 35%	39.5% min.	19% - 23%

Alloy 800 and the root of the Alloy 82 weld share similar iron contents. However, the chromium content is much higher in Alloy 800. Alloy 800 should form a combination of external iron and chromium oxides. These layers will inhibit the ingress of oxygen. The Alloy 82 root does not have the potential to form an external chromium oxide and may internally oxidize increasing PWSCC susceptibility. XPS results indicate that the only region on the welds which have the potential to form an external chromium oxide is at the outer edge of the filler where the chromium content is at its peak. This region would never be exposed to primary water conditions during plant operation.

Dutta et al. exposed Alloy 800 to PWSCC environments for 264h [53]. There were mixed oxides of both chromium and iron on the surface. It is unclear whether the presence of an iron oxide alone would make dissimilar Alloy 82 welds PWSCC resistant. As mentioned, the presence of small nodules elevated in nickel content on the root indicates that chromium may have oxidized internally before a healing layer of iron was formed externally. The external iron oxide on the root may make the Alloy 82 welds less susceptible to PWSCC than Alloy 600, as indicated by several studies, but not completely PWSCC immune like Alloy 800.

5.5 Effect of Exposure Time

Samples were exposed for 3 days and 5 days. It is difficult to attribute the difference in oxidation to time. Diffusion is proportional to the square root of time. The difference in time was 2 days which is not enough to draw firm conclusions on time effects. The potential effects of increased exposure time are discussed in this section.

Macroscopically, exposed welds looked similar regardless of exposure time. However, SEM images indicated that exposures for 5 days contained a more developed iron oxide on the root of the weld. Additionally, areas with chromium contents greater than 15% appeared to have a layer of expelled Ni rather than simply nodules. The regions with less than 15% Cr had the typical expulsion of nodules seen in internal oxidation first by Rapp [23] and later by Scenini [50].

A much larger amount of Ni being expelled at higher chromium contents could be due to more chromium internally oxidizing for approximately the same depth of oxygen penetration over a longer time period. 16% Cr is the threshold border for the transition from internal to external chromium oxide. Patches in the filler consisted of chromium contents in excess of 18% and XPS indicated the formation of an external chromium oxide.

The root of the welds developed an iron oxide with some small pure nickel nodules. An increase in time would allow for more iron to diffuse to the surface. However, these results do not agree with those found by Scenini et al. on Alloy 600 at similar conditions. Scenini noticed Ni nodules being expelled in the same fashion regardless of exposure time. Time would have to be increased dramatically to produce these effects.

5.6 Effect of Hydrogen Partial Pressure Position in Relation to the Ni/NiO Equilibrium

Previous studies indicate that the highest crack growth rate in Alloy 82 and 182 welds occurred at approximately 11 $cm^3\ H_{2_{(aq)}}/kg\ H_2O_{(l)}$ at SATP, or just below the Ni/NiO dissociation pressure. Lima et al. found that at greater dissolved hydrogen contents (50 $cm^3\ H_{2_{(aq)}}/$ $kg\ H_2O_{(l)}$) the external oxide on the root of the weld was less porous [42]. They suggested that this film may be a protective iron oxide.

In this study, the external oxide on the root of the weld did not vary in particle size with an increase in hydrogen partial pressure. However, an increase in exposure time caused the external oxide to increase in crystal size, while the nickel nodules grew smaller. Andresen et al. suggested that increasing the hydrogen content in primary water to 100 $cm^3\ H_{2_{(aq)}}/kg\ H_2O_{(l)}$ would cause the crack growth rate of Alloy 82 welds to become negligible [12]. Increasing the hydrogen partial pressure to these levels was not performed in this study.

Chapter 6: Summary of High Pressure Exposures to Hydrogenated Steam at 375ºC

6.1 Summary of Experimental Details

Sample preparation, the operating procedure, and sample removal are discussed in detail in Appendix C, section C-1. Alloy 82 weld samples were exposed to a simulated PWR environment with 10.0 MPa of hydrogenated steam at 375ºC. Samples were mechanically polished and exposed to hydrogenated steam in a 2.2 litre autoclave vessel. There were many inherent flaws in the system which may have led to some debatable results and caused many experiments to fail. Many experiments were attempted but only five were considered successful experiments. These experiments were similar to those performed by Fabio Scenini on Alloy 690 and 600 at 400ºC and 20.7 MPa [63].

6.2 Discussion of SEM and EDX Results

There are some similarities between SEM and EDX results for all exposed Alloy 82 weld samples. The root of all the exposed welds had a darkened region, which may be an oxide, and flakes enriched in nickel. The filler had lines which may be composed of small particles or nodules.

The darkened stained regions on the Alloy 82 root could not be successfully characterized. EDX analysis of the darkened regions returned a similar composition to that of the Alloy 82 root. Previous studies by Scenini et al. indicated the formation of a spinel type oxide on the surface of mechanically polished Alloy 600 after exposure to hydrogenated steam at 400ºC and 20.7 MPa [63]. The oxide on the Alloy 82 root in these experiments does not have a spinel formation. Another analytical technique may need to be employed to determine the composition of this darkened region.

Randomly distributed flakes were also present on the root the exposed Alloy 82 weld samples. EDX analysis indicated that these flakes were slightly enriched in nickel (approximately 10% more nickel than in the surrounding region). The initial assumption was that these flakes were a potential indication of internal oxidation of chromium. Given the low composition of chromium, this seems like it could be a viable assumption. However, Scenini found similar flakes on samples of Alloy 690 exposed to at 400ºC and 20.7 MPa, but with increased kinetics.

Internal oxidation is unlikely on Alloy 690 due to its high chromium content of 27% - 31% [63]. Alloy 690 is more likely to form an external and protective C_2O_3 film on the surface.

Scenini suggested that the reason for flakes on the surface of the Alloy 690 samples was stoichiometry. The Fe-Cr spinel present in the root of Figure 27 (a) for low pressure exposures can be either Fe_3O_4 or $FeCr_2O_4$ due to the double valence state of Fe [63]. On the other hand, nickel has only one valence state (+2). Therefore, the Ni-Cr spinel oxide can exist only as $NiCr_2O_4$. Scenini reasoned that the nickel available would form the Ni-Cr spinel. However, there would be nickel remaining which would not form the $NiCr_2O_4$ spinel or NiO because conditions were below the Ni/NiO dissociation pressure. The remaining nickel would form these metallic flakes [63]. In this study, there should be sufficient Ni and Cr to form a Ni-Cr spinel without having excess Ni. Consequently, Scenini's explanation is insufficient since similar flakes enriched in Ni formed on the Alloy 82 root. Given the low Cr content in the root of the weld, internal oxidation seems like a more reasonable explanation.

The filler of the Alloy 82 weld was comprised of lines of small particles with empty spaces separating them. The spacing is similar to those experiments performed in the low pressure atmospheric reactor at 480ºC. However, the particles are significantly smaller than the large pure Ni nodules present in the latter experiments. The EDX results indicate a small enrichment in Ni among clusters of small nodules. Scenini found similar small particles which caused Ni enrichment along grain boundaries of Alloy 600 exposed with 20.7MPa of hydrogenated steam at 400ºC [63]. He concluded that these small particles could be evidence of internal oxidation of chromium. Scenini's conclusion may be applicable to the exposed Alloy 82 welds but further analysis using a more sensitive surface analysis technique should be done for validation.

Chapter 7: Conclusions

7.1 Metallurgical Analysis of Alloy 82 Welds

Weld composition was affected dramatically by the presence of dendrites, non-homogeneous nucleation, and dilution. In particular, dilution of the carbon steel parent material into the Alloy 82 welds increased the iron content in the root of the welds to twelve times the amount quoted in literature to approximately 34%. Also, the chromium content of the Alloy 82 welds was depleted to 11%-13% in the root and 14%-18% in the filler.

7.2 Low Pressure Exposures to Hydrogenated Steam at 480ºC

EDX analysis shows that the large nodules and/or layer formed on the Alloy 82 filler are at least a 90% nickel. AES and XPS confirmed the presence of pure nickel and determined the depth of oxygen penetration to be approximately 0.7 μm. This would support the internal oxidation model. The oxygen diffused into the filler of the Alloy 82 weld and internally oxidized chromium causing the expulsion of pure nickel to the surface by mechanical action and/or diffusion.

A potentially protective external oxide, consisting of primarily Fe_3O_4 and $FeCr_2O_4$, formed on the Alloy 82 root. However, the chromium content of the root is below that which would form an external oxide. Internal oxidation of chromium could occur first expelling pure nickel nodules. This would be followed by the formation of the iron oxide healing layer which would make the root of the weld susceptible to PWSCC.

To conclude, Alloy 82 welds of this type are probably not as susceptible to PWSCC as Alloy 600. However, they are not immune, like Alloy 800 and Alloy 690, due to the potential for internal oxidation in the root prior to the formation of a protective external oxide.

7.3 High Pressure Exposures to Hydrogenated Steam at 375ºC

Experiments performed at high pressure and 400ºC produced generally inconclusive results. However, there were results that indicated potential internal oxidation such as flakes and small particles with Ni enrichment distributed throughout weld samples. There were darkened regions across the weld which may indicate the presence of an external oxide.

Chapter 8: Future Work

The external iron oxide present on the Alloy 82 welds may be PWSCC resistant. There are signs of internal oxidation within the spinel oxide, but it is not a certainty. The area beneath the external oxide should be analyzed to determine if there was any internal oxidation of chromium. This can be done using a Focused Ion Beam (FIB) to cut and remove a cross-sectional area including the external oxide and the region beneath. The cross-sectional area can then be analyzed to determine if internal oxidation occurred beneath the external oxide film.

Exposed samples in the atmospheric reactor at 480ºC show a significant difference in nickel expulsion and external oxide formation after 3 and 5 days. The difference in time should be insignificant due to diffusion being proportional to the square root of time. Samples should be exposed for extreme differences in time to determine if there are any variations in the internal or external oxidation with respect to time.

The high pressure experiments at 400ºC take place in a batch system. The amount of hydrogen adsorbed to the autoclave or reacted will change the conditions of the system with respect to the Ni/NiO dissociation pressure. Scenini used a hydrogen cell to monitor and adjust the partial pressure of hydrogen when appropriate. This cell was comprised of a 7 mm stainless tube with a porous insert of palladium. The hydrogen partial pressure at the Ni/NiO equilibrium was equal to the hydrogen pressure in the middle of the cell, which was monitored throughout the experiment [63].

The analytical results from the high pressure experiments at 400ºC are inconclusive. The small particles on the filler and the flakes on the root have nickel enrichment. The composition of these particles need to be determined using a more sensitive analytical technique, such as AES or XPS.

Chapter 9: References

[1] P.M. Scott, *"An Overview of Internal Oxidation as a Possible Explanation of Intergranular Stress Corrosion Cracking of Alloy 600 in PWRs,"* Proceedings of the 9th International Conference on Environmental Degradation of Materials in Nuclear Power Systems - Water Reactors, edited by S. Bruemmer, P. Ford, G. Was. (Warrendale, PA, Aug. 1-5: Minerals, Metals and Materials Society/AIME, 1999), p. 3-14.

[2] H. Coriou, L. Grall, P. Olivier, H. Willermoz, *"Influence of Carbon and Nickel Content on Stress- Corrosion Cracking of Austenitic Stainless Alloys in Pure or Chloride Containing Water at 350ºC,"* Proceedings of Conference of Fundamental Aspects of Stress-Corrosion Cracking, edited by R.W. Staehle. (Houston, TX: 1969), p. 352.

[3] M.L. Bauccio, *ASM Metals Reference Book*, 1993: Materials Park, Ohio: ASM International.

[4] F. Delabrouille, L. Legras, F. Vaillant, P. Scott, B. Viguier, E. Andrieu, *"Effect of the Chromium Content and Strain on the Corrosion of Nickel Based Alloys in Primary Water of Pressurized Water Reactors,"* Proceedings of the 12th International Conference on Environmental Degradation of Materials in Nuclear Power Systems – Water Reactors, edited by T.R. Allen. (Salt Lake City, UT, Aug. 14-18: Minerals, Metals and Materials Society/AIME, 2005), p. 903-911.

[5] C.M. Younes, F.H. Morrissey, G.C. Allen, P. McIntyre, *"Effect of Heat Treatment on the Grain Boundary Chemistry and the Resistance to Intergranular Corrosion of Alloy 600 and Alloy 690,"* Proceedings of the 2nd International Conference on Corrosion-Deformation Interactions, edited by T. Margin. (Nice, France: NACE International, 1996), p. 421-434.

[6] G.S. Was, J.K. Sung, T.M. Angeliu, *"Effects of Grain Boundary Chemistry on the Intergranular Cracking Behaviour of Ni-16Cr-9Fe in High-Temperature Water,"* Metallurgical Transactions A, 1992, 23A: p. 3343-3359.

[7] K.H. Pyro, P.J. Kyu, L.Y. Soo, K.J. Soo, *"Effect of Microstructure on Stress Corrosion Cracking of Alloy 600 and Alloy 690 in Caustic Solution,"* Proceedings of the 16th International Conference on Structural Mechanics in Reactor Technology, edited by G. Wilkowski. (Washington DC, USA: 2001), p. 1-8.

[8] Y.S. Lim, J.H. Han, H.D. Cho, J.S. Kim, *"Precipitation Morphologies of Grain Boundary Chromium Carbides in Alloy 690TT,"* Proceedings of the 16th International Conference on Structural Mechanics in Reactor Technology, edited by G. Wilkowski. (Washington DC, USA: 2001), p. 8-15.

[9] H. Xu, S. Fyfitch, *"Laboratory Investigation of the Alloy 600 Bottom Mounted Instrumentation Nozzle Samples and Weld Boat Sample from South Texas Project Unit I,"* Proceedings of the 12th International Conference on Environmental Degradation in Nuclear Power Systems-Water Reactors, edited by T.R. Allen. (Salt Lake City, UT, Aug. 14-18: Minerals, Metals and Materials Society/AIME, 2005), p. 843-853.

[10] Report MRP-55, "*Materials Reliability Program (MRP) Crack Growth Rates for Evaluating Primary Water Stress Corrosion Cracking (PWSCC) of Thick-Wall Alloy 600 Material,*" (Palo Alto, CA: EPRI, 2002) (Non-proprietary version), p. 1-28.

[11] G. Economy, R.J. Jacko, F.W. Pement, *"IGSCC Behavior of Alloy 600 Steam Generator Tubing in Water or Steam Tests Above 360 deg C,"* Corrosion, 1987, 43(12): p. 727- 734.

[12] P. Andresen, R. Reid, J. Wilson, *"SCC Mitigation of Ni Alloys and Weld Metals by Optimizing Dissolved H2,"* 14th International Conference on Environmental Degradation of Materials in Nuclear Power Systems – Water Reactors. (Virginia Beach, VA, Aug. 23-27: Curran Associates Inc., 2009), p. 1-29.

[13] D.S. Morton, M. Hansen, *"The Effect of pH on Nickel Alloy SCC and Corrosion Performance,"* Proceedings of the Annual NACE Conference, edited by G.A. Cragnolino, D.S. Dunn, V. Jain, L. Yang. (San Diego, CA, Mar. 16-20: NACE, 2003), p. 12-19

[14] T. Nakagawa, N. Totsuka, T. Terachi, N. Nakajima, *"Influence of Dissolved Hydrogen on Oxide Film and PWSCC of Alloy 600 in PWR Primary Water,"* Journal of Nuclear Science and Technology, 2003, 40(1): p. 39-43.

[15] R.B. Rebak, Z. Szklarska-Smialowska, *"The Mechanism of Stress Corrosion Cracking of Alloy 600 in High Temperature Water,"* Corrosion Science, 1996, 38(6): p. 971-988.

[16] R.C. Newman. (November, 2009). *"Stress Corrosion Cracking"*. Lecture delivered at the University of Toronto. University of Toronto, Toronto, ON, Canada.

[17] P.L. Andresen, F.P Ford, *"Response to 'On the Modelling of Stress Corrosion Cracking of Iron and Nickel Base Alloys in High Temperature Aqueous Environments,"* Corrosion, 1996, 38(6): p. 1011-1016.

[18] J.R. Galvele, *"A Stress Corrosion Cracking Mechanism Based on Surface Mobility,"* Corrosion Science, 1987, 27(1): p. 1-33.

[19] A. Barnoush (2007). *"Hydrogen Embrittlement"*. Lecture delivered in Materials Science and Methods at Saarland Unversity, Saarbruecken, Germany.

[20] F.Foct, O.D. Bouview, T. Magnin, *"Stress Corrosion Cracking Mechanisms of Alloy 600 Polycrystals and Single Crystals in Primary Water – Influence of Hydrogen,"* Metallurgical and Materials Transactions A, 2000, 31A: p. 2025-2036.

[21] A.S. Khanna. *Introduction to High Temperature Oxidation and Corrosion*, 2002: Materials Park, Ohio: ASM International.

[22] F.H. Stott, G.C. Wood, *"Internal Oxidation,"* Materials Science and Technology, 1988, 4 (12): p. 1072-1078.

[23] S. Guruswamy, S.M. Park, J.P. Hirth, R.A. Rapp. *"Internal Oxidation of Ag-In Alloys: Stress Relief and the Influence of Imposed Strain",* Oxidation of metals, 1986, 26(1/2): p. 77-100.

[24] G.C. Wood, F.H. Stott, D.P. Whittle, Y. Shida, B.D. Bastow, *"The High-Temperature Internal Oxidation and Intergranular Oxidation of Nickel-Chromium Alloys,"* Corrosion Science, 1983, 23(1): p. 9-25.

[25] F.H. Stott, G.C. Wodd, D.P. Whittle, B.D. Bastow, Y. Shida, A. Martinez-Villafane, *"The Transport of Oxygen to the Advancing Internal Oxide Front During Internal Oxidation of Nickel-Based Alloys at High Temperature,"* Solid State Ionics, 1984, 12: p. 365-374.

[26] C.F. Miller, G.W. Simmons, R.P. Wei, *"Evidence for Internal Oxidation during Oxygen Enhanced Crack Growth in P/M Ni-Based Superalloys,"* Scripta Materialia, 2003, 48 (1): p. 103-108.

[27] P.M. Scott, M. Le Calvar, *"Some Possible Mechanisms of Intergranular Stress Corrosion Cracking of Alloy 600 in PWR Primary Water"*, Proceedings of the 6th International Conference on Environmental Degradation of Materials in Nuclear Power Systems-Water Reactors, edited by E.P. Simonen. (San Diego, CA, Aug. 1-5: Minerals Metals and Materials Society/AIME, 1993), p. 657-665.

[28] T.S. Gendron, S.J. Bushby, R.D. Cleland, R.C. Newman, *"Oxidation embrittlement of alloy 600 in hydrogenated steam at 400 deg C"*, Proceedings of the 2nd International Conference on Corrosion-Deformation Interactions, edited by T. Margin. (Nice, France: NACE International, 1996), p. 7-15.

[29] R.C. Newman, T.S. Gendron, P.M. Scott. *"Internal oxidation and embrittlement of Alloy 600"*, Proceedings of the 9th International Conference on Environmental Degradation of Materials in Nuclear Power Systems-Water Reactors, edited by S. Bruemmer, P. Ford, G. Was. (Warrendale, PA, Aug. 1-5: Minerals, Metals and Materials Society/AIME, 1999), p. 79-93.

[30] J. Panter, B. Viguier, J.M. Cloue, M. Foucault, P. Combrade, E. Andrieu, *"Influence of Oxide Films on Primary Water Stress Corrosion Cracking Initiation of Alloy 600,"* Journal of Nuclear Materials, 2006, 348 (1-2): p. 213-221.

[31] R.W. Staehle, Z. Fang, *"Comments on a proposed mechanism of internal oxidation for alloy 600 as applied to low potential SCC,"* Proceedings of the 9th International Conference on Environmental Degradation of Materials in Nuclear Power Systems-Water Reactors, edited by S. Bruemmer, P. Ford, G. Was. (Warrendale, PA, Aug. 1-5: Minerals, Metals and Materials Society/AIME, 1999), p. 69-77.

[32] R. Celin, F. Tehovnik, *"Degradation of a Ni-Cr-Fe Alloy in a Pressurised-Water Nuclear Power Plant,"* Institute of metals and technology, 2011, 45 (2): p. 151-157.

[33] Report NUREG/CR-6864, *"Crack Growth Rates and Metallographic Examinations of Alloy 600 and Alloy 82/182 fromField Components and Laboratory Materials Tested in PWR Environments,"* (Argonne, IL: United States Nuclear Regulatory Comission, May 2008), p. 1-63.

[34] Y. Soo Lim, H. Pyo Kim, H. Dong Cho, H. Hee Lee, *"Microscopic examination of an alloy 600/182 weld,"* Journal of Materials Characterization, 2009, 60 (12) : p. 1496-1506.

[35] S. Kou, *Welding Metallurgy*, 2003: New Jersey: John Wiley & Sons, Inc.

[36] S. J. Patel and G. D. Smith, *"The Role of Niobium in Wrought Superalloys,"* Proceedings of the 6th International Conference on Superalloys 718, 620, 706 and Derivatives, edited by E.A. Loria. (Pittsburgh, PA, Oct. 2-5: The Minerals, Metals, and Materials Society, 2005), p. 135-154.

[37] R. Rebak, P. Crook, *"Nickel Alloys for Corrosive Environments,"* Advanced Materials and Processes, 2000, 12 (3): p. 167–176.

[38] T. Fukumura, N. Totsuka, *"PWSCC susceptibility of stainless steel and nickel based alloy of dissimilar metal butt welds,"* NACE – International Corrosion Conference Series. (San Antonio, TX, Mar. 14-18: NACE International, 2010), p. 26-37.

[39] M.Nouri, A.Abdollah-zadeh, F.Malek, *"Effect of Welding Parameters on Dilution and Weld Bead Geometry in Cladding,"* Journal of Material Science Technology, 2007, 23 (6): p. 817-822.

[40] S.A. Davies, *Theory and Practice of Gas Tungsten Arc Welding*, 1991: Australia: Harcourt Brance Jovanovich.

[41] Report MRP-115NP, *"Materials Reliability Program, Crack growth rates for evaluating primary water stress corrosion cracking (PWSCC) of Alloy 82, 182, and 132 Welds,"* (Concord, CA: EPRI, 2004), p. 3-1 to 3-16.

[42] L.L. Lima, M.M.A.M Schvartman, C.A.Figueiredo, A.Q Bracarense, *"Stress Corrosion Cracking Behaviour of Alloy 182 Weld in Pressurized Water Reactor Primary Water Environment at 325ºC,"* Corrosion, 2011, 67(8): p. 085004-1 – 085004-9.

[43] P. Scott, M. Foucault, B. Brugier, J. Hickling, A. McIlree, *"Examination of stress corrosion cracks in Alloy 82 weld metal after exposure to PWR primary water,"* Proceedings of the 12th International Conference on Environmental Degradation of Materials in Nuclear Power Systems – Water Reactors, edited by T.R. Allen. (Salt Lake City, UT, Aug. 14-18: Minerals, Metals and Materials Society/AIME, 2005), p. 497-509.

[44] A. Jenssen, K. Norrgrad, G. Embring, J. Lagerstrom, D.R. Tice, "*Assessment of cracking in dissimilar metal welds*," Proceedings of the 10th International Conference on Environmental Degradation of Materials in Nuclear Power System — Water Reactors. (Lake Tahoe, NV, Aug. 5-9: Minerals, Metals, and Materials Society/AIME, 2001), p. 421-434.

[45] P. Efsing, C. Jansson, A. Jenssen, J. Sundberg, B. Forssgren, B. Bengtsson, A. Johnsson, *"IGSCC Disposition Curves for Alloy 82 in BWR Normal Water Chemistry,"* Proceedings of the 13th International Conference on Environmental Degradation of Materials in Nuclear Power Systems – Water Reactors, (Whistler, Canada, Aug. 19-23: Minerals, Metals and Materials Society/AIME, 2007), p. 1353-1363.

[46] I. Anzel, *"High Temperature Oxidation of Metals and Alloys"*, Metalurgija – Journal of Metallurgy, 2000, 39 (3): p. 325-336.

[47] C. Wagner, Z. Elektrochem., 63 (1959), 773.

[48] R.A. Rapp, *"The Transition from Internal to External Oxidation and the Formation of Interruption Bands in Silver-Indium Alloys,"* Acta Metallurgical, 1961, 23: p. 730-741.

[49] P. Kofstad. *High-Temperature Oxidation of Metals*, 1966: Oslo, Norway: John Wiley & Sons, Inc.

[50] F. Scenini, R.C. Newman, R.A. Cottis, R.J. Jacko, *"Alloy Oxidation Studies Related to PWSCC,"* Proceedings of the 12th International Conference on Environmental Degradation of Materials in Nuclear Power Systems – Water Reactors, edited by T.R. Allen. (Salt Lake City, UT, Aug. 14-18: Minerals, Metals and Materials Society/AIME, 2005), p. 891-902.

[51] R.C. Newman, F. Scenini, *"Another Way to Think About the Critical Oxide Volume Fraction for the Internal-to-External Oxidation Transition?,"* Corrosion, 2008, 64(9): p. 721-726.

[52] D.R. Askeland, P.P. Phule. *The Science and Engineering of Materials*, 2006: Toronto, ON: Thomson Canada Ltd.

[53] R.S. Dutta, *"Effect of Ageing Treatment on the Corrosion Properties of Alloy 800,"* Transactions of the Indian Institute of Metals, 2004, 57 (5): A44.

[54] R. Killian, *"Operating Experience with Alloy 800 SG Tubing in Europe,"* 13th International Conference on Environmental Degradation of Materials in Nuclear Power Systems, (Whistler, Canada, Aug. 19-23: Minerals, Metals and Materials Society/AIME, 2007), p. 1264-1275

[55] B. M. Capell, G.S. Was, *"Selective Internal Oxidation as a Mechanism for Intergranular Stress Corrosion Cracking of Ni-Cr-Fe Alloys,"* Metallurgical and Materials Transactions A, 2007, 38A: p. 1244-1259.

[56] Scenini, F., R. C. Newman, R. A. Cottis, *"Effect of Surface Preparation on Intergranular Stress Corrosion Cracking of Alloy 600 in Hydrogenated Steam,"* Corrosion, 2008, 64(11): p. 824-35.

[57] O.C. Wells, A. Boyde, E. Lifshin, A. Rezanowich. *Scanning Electron Microscopy*. Vol. 18. New York, NY, USA: McGraw-Hill, 1974.

[58] W. Zhou, Z. L. Wang. *Scanning Microscopy for Nanotechnology Techniques and Applications*. New York, NY, USA: Springer, 2007.

[59] D. Briggs and M.P. Seah. *Practical Surface Analysis. Volume 1 – Auger and X-ray Photoelectron Spectroscopy.* Second Edition. Chichester: John Wiley and Sons, 1990

[60] D. Briggs, J.T. Grant. *Surface Analysis by Auger and X-ray Photoelectron Spectroscopy*. Vol 6. Surface Spectra, 2003.

[61] R.C. Newman. *Private Communication.* Oct. 2010

[62] C. D. Wagner, A. V. Naumkin, A. Kraut-Vass, J. W. Allison, C. J. Powell, J. R. Rumble, Jr. *"NIST X-ray Photoelectron Spectroscopy Database,"* Published August 27, 2007. NIST Standard Reference Database 20, Version 3.5. Accessed September 16, 2011 <http://srdata.nist.gov/xps/>

[63] F. Scenini. *The Effect of Surface Preparation on the Oxidation and SCC Behaviour or Alloy 600 and 690 in Hydrogenated Steam.* Doctoral dissertation, University of Manchester, Manchester, United Kingdom. (2006).

[64] R.C. Weast. *CRC Handbook of Chemistry and Physics*. 67th Edition. Boca Raton, FL, USA: CRC Press Inc, 1986.

Appendices

Appendix A – Additional EDX Spectra and Composition Trends

Appendix B – Calculation of Oxygen Partial Pressure at Ni/NiO Dissociation Pressure and Atmospheric Reactor Parameters

Appendix C – Experimental Details and Results for High Pressure Exposure to Hydrogenated Steam at 375ºC

Appendix A: EDX Spectra and Composition Trends

Titanium and Niobium Carbides Described in Section 4.2.2

Several carbide inclusions were noticed on the surface of the Alloy 82 weld samples. Niobium carbide inclusions were formed along grain boundaries, while titanium carbides were distributed within grains randomly. Figure 31 (a) is an example of a titanium carbide located on the Alloy 82 filler with its EDX spectra (b) confirming the carbide as primarily composed of titanium. The elevated chromium and nickel shown on the EDX spectra can be credited to the poor accuracy of EDX in areas as small as the titanium carbide.

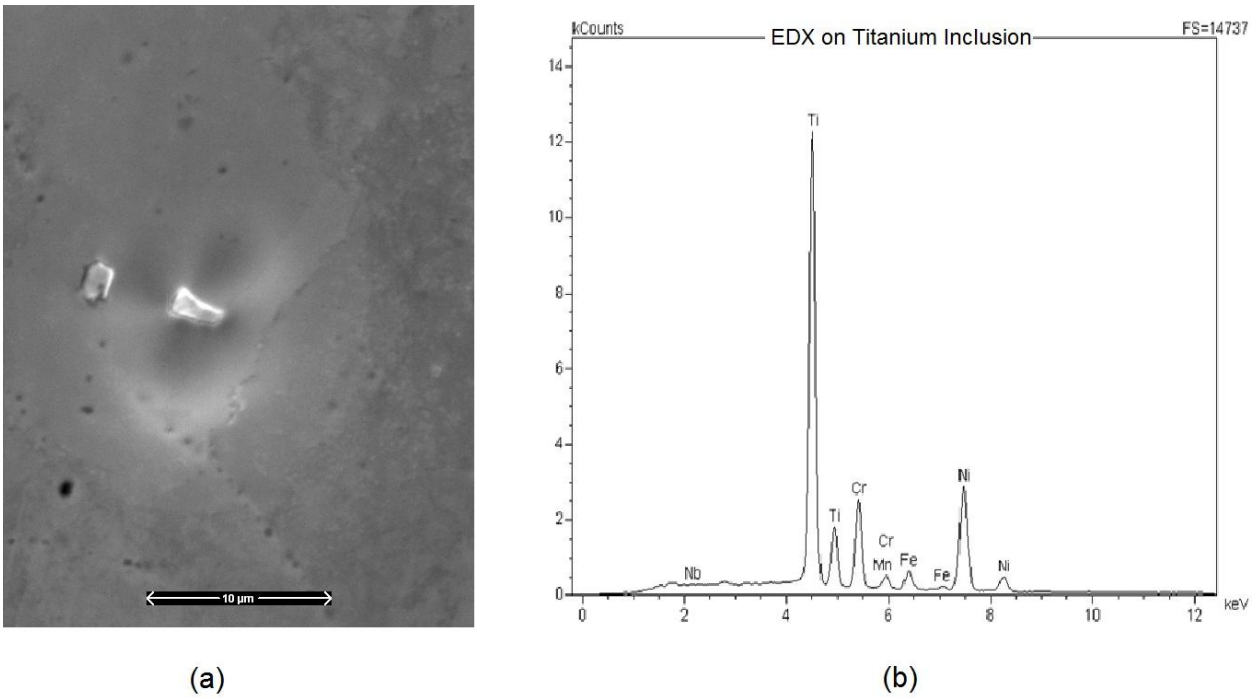

Figure 31 – A typical titanium carbide on the Alloy 82 filler (a) with EDX spectra (b)

Niobium carbides were much more prevalent than titanium carbides. There is a significantly higher composition of niobium than titanium in Alloy 82. Niobium carbides were located primarily along grain boundaries. Figure 32 is a niobium carbide (a) with its EDX spectra.

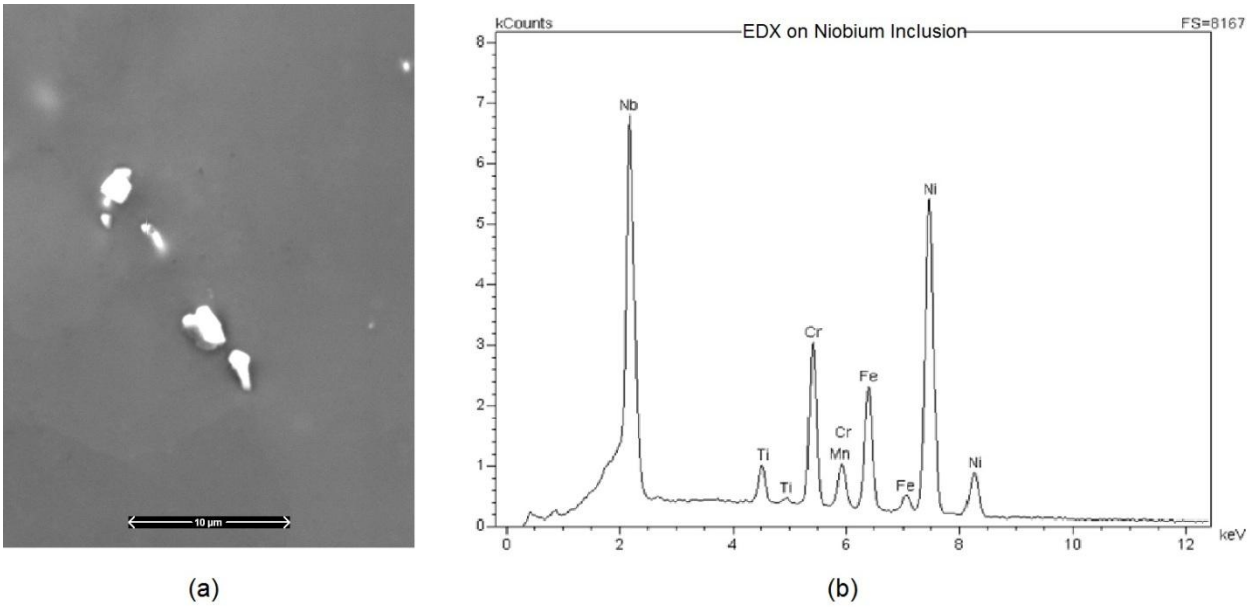

Figure 32 – A typical niobium carbide on the Alloy 82 weld (a) with EDX spectra (b)

Composition Trends in the x-Direction on Alloy 82 Root and Filler in Section 4.3.1

Unlike in the y-direction, the composition trends in the x-direction of the Alloy 82 weld were fairly constant. This was caused by the direction of cooling after welding. Welds cool in the y-direction which means the composition of each layer in the x-direction should be fairly constant. Composition trends in the x-direction for the Alloy 82 root are given in Figure 33 for nickel (b), iron (c), and chromium (d). The composition of each major element does not fluctuate more than a few percent. However, it still indicates very minor dilution closest to the carbon steel parent material (iron is the highest near the carbon steel while nickel and chromium are slightly depleted). A similar diagram is given in Figure 34 which is the composition trends across the filler of the weld. The composition remains fairly constant in the x-direction.

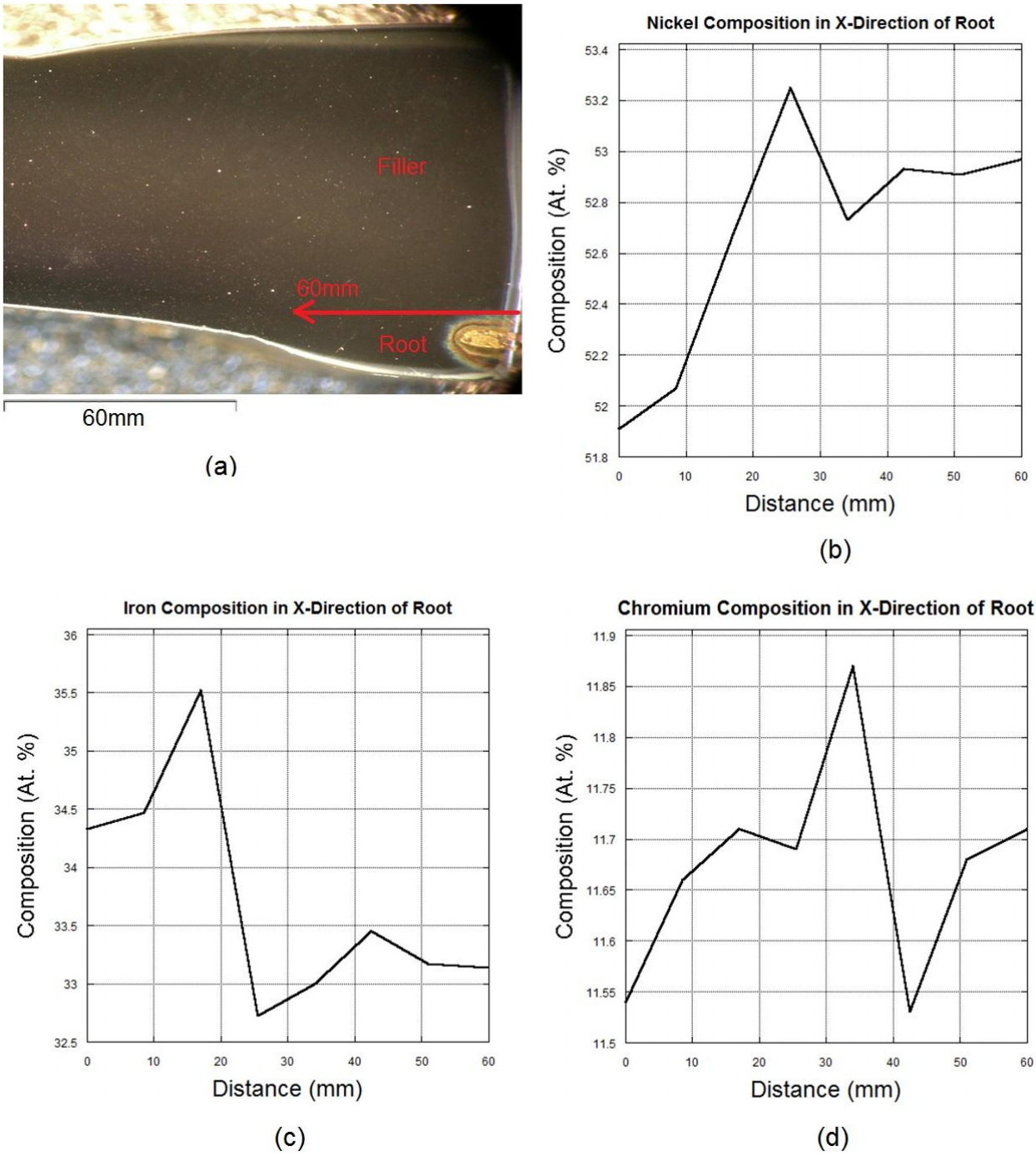

Figure 33 – Alloy 82 weld (a) with EDX spectra showing the composition of nickel (b), iron (c) and chromium (d) in the x-direction across the root (highlighted in red)

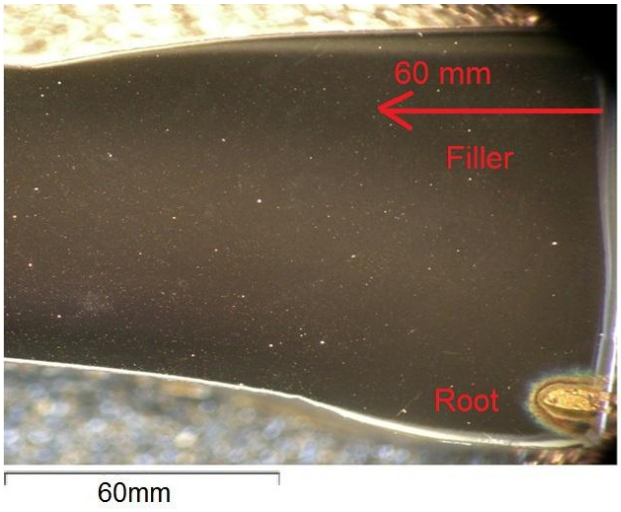

(a)

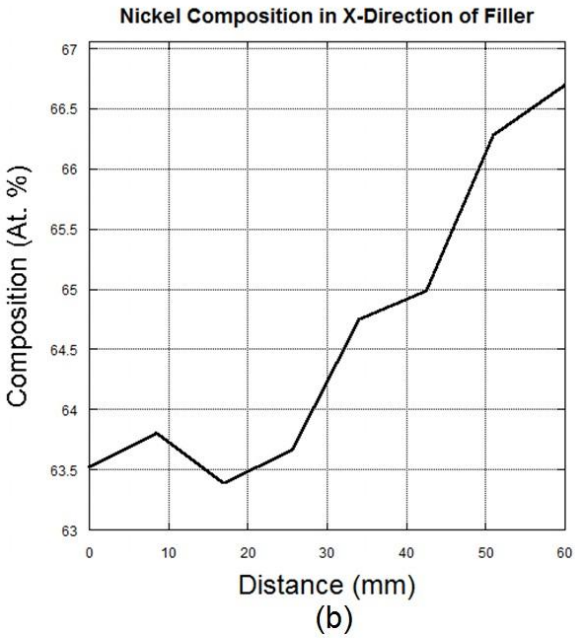

(b)

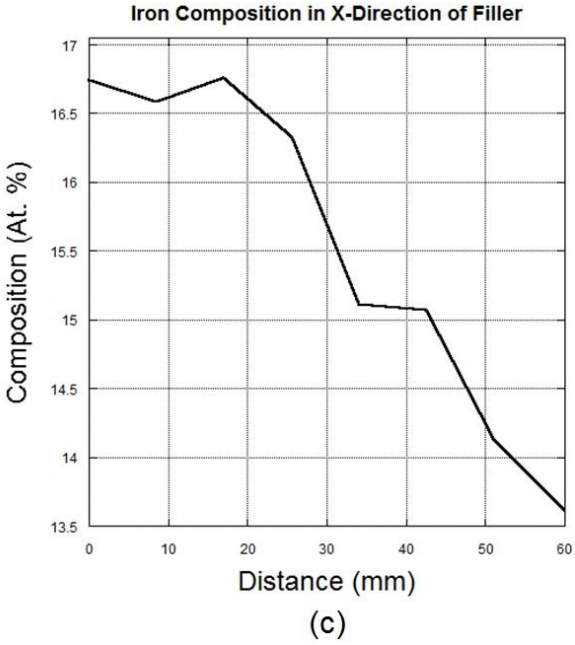

(c)

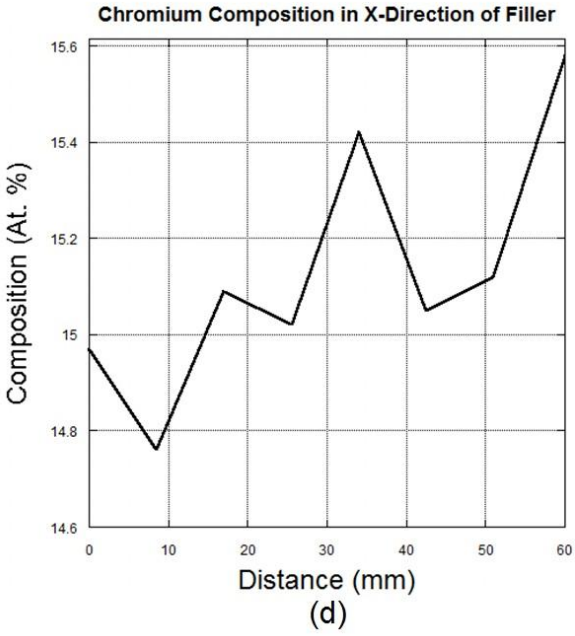

(d)

Figure 34 – Alloy 82 weld (a) with EDX spectra showing the composition of nickel (b), iron (c) and chromium (d) in the x-direction across the filler (highlighted in red)

EDX Spectra for Ni Nodules in Section 5.2.1.1

Table 6 gives numerical values for the composition of Ni nodules in the Alloy 82 weld root and filler. These compositions were calculated from the EDX spectra in this section. Table 12 associates each EDX spectra figure with the regions in Table 6.

Table 12 – Table associating EDX spectra with the regions defined in Table 6

Region	Associated Figure
Small Nodules in Fig. 25 (b)	Figure 35 (a)
Around Small Nodules in (b)	Figure 35 (b)
Large Nodules in Fig. 25 (d)	Figure 36 (a)
Around Large Nodules in (d)	Figure 36 (b)

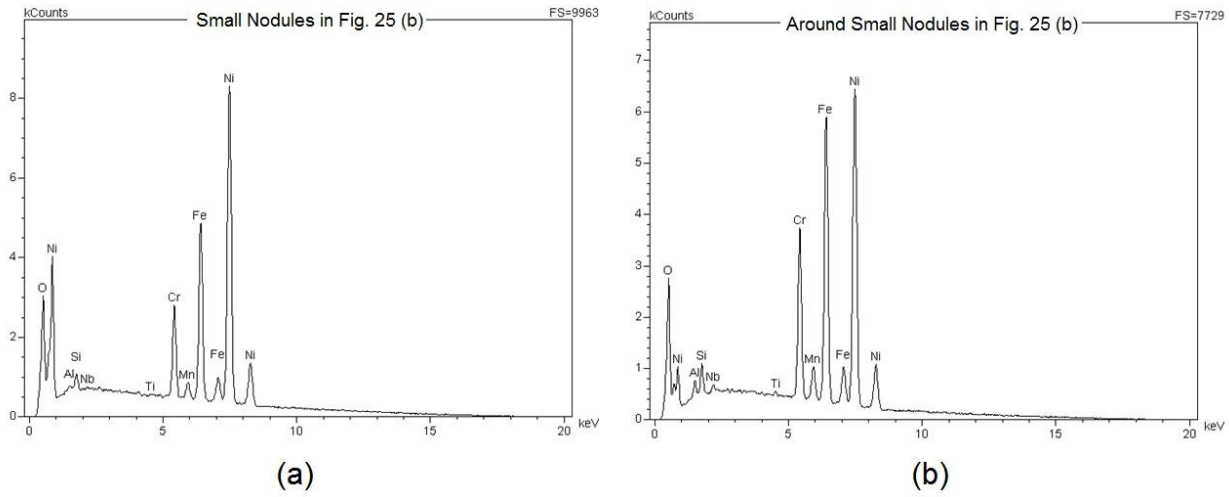

Figure 35 – EDX spectra of the small nodules (a) and around the small nodules (b) in the root of the exposed Alloy 82 weld after 3 days.

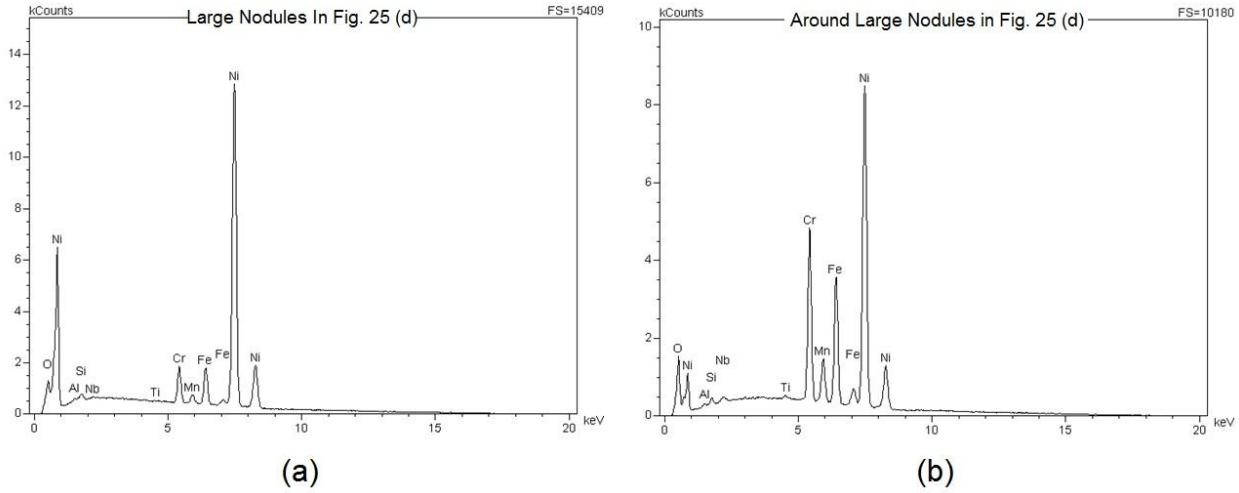

Figure 36 – EDX spectra of the large nodules (a) and around the large nodules (b) in the filler of the exposed Alloy 82 weld after 3 days.

EDX Spectra for Ni Nodules, Ni Layer, and Root Oxide in Section 5.2.1.2

Table 7 gives numerical values for the composition of Ni nodules, Ni layer, and root oxide in the Alloy 82 weld root and filler. These compositions were determined from the EDX spectra in this section. Table 13 associates each EDX spectra with the regions in Table 7.

Table 13 – Table associating EDX spectra with the regions defined in Table 7

Region	Associated Figure
Region 3 Nickel Layer	Figure 37 (a)
Region 2 Nickel Nodules	Figure 37 (b)
Region 1 Oxide	Figure 38 (a)
Region 1 areas within Oxide	Figure 38 (b)

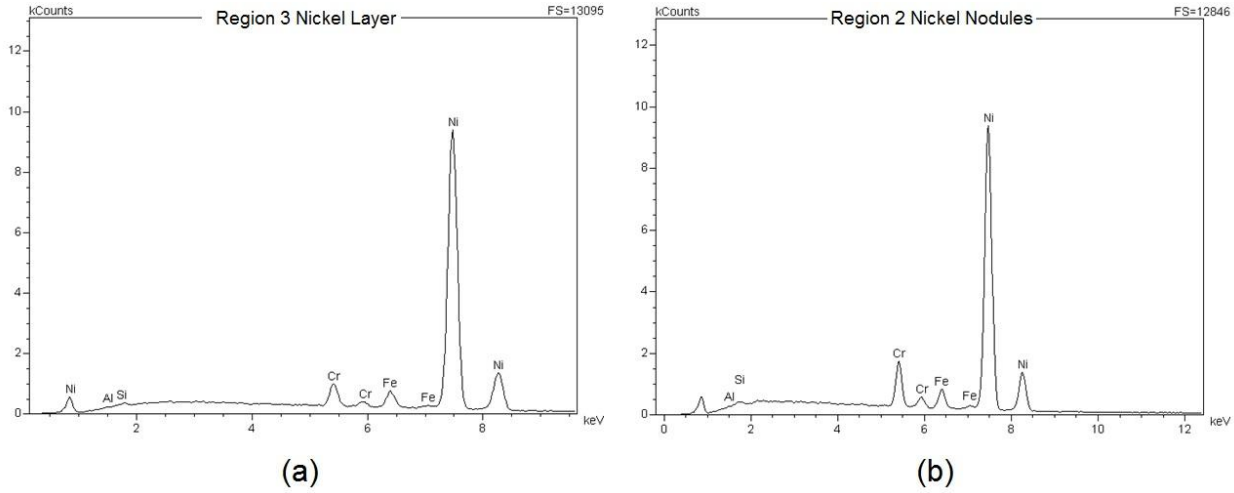

Figure 37 – EDX spectra of the nickel layer (a) and the nickel nodules in the filler of the Alloy 82 weld after exposure for 5 days.

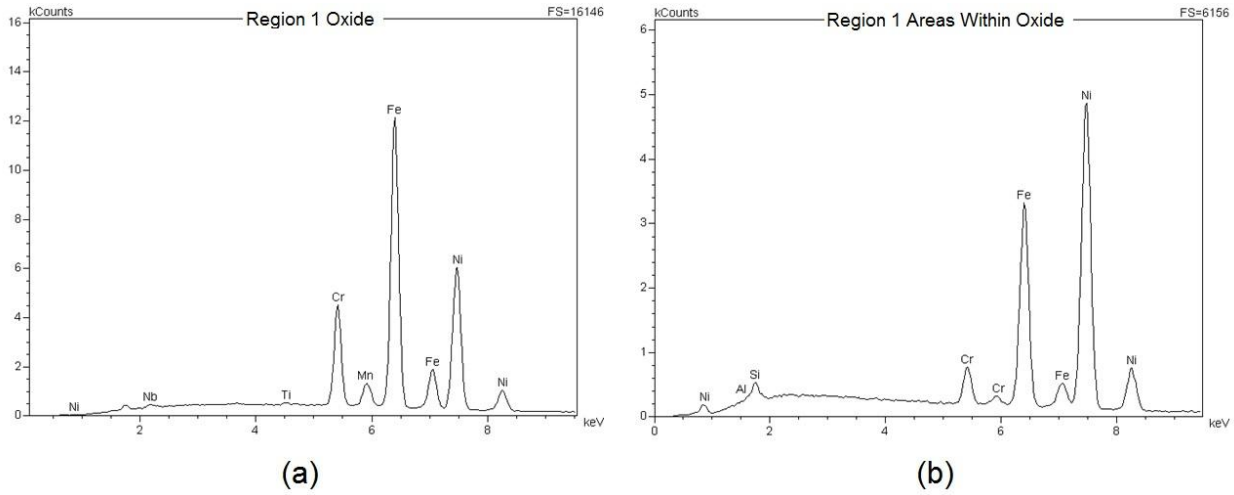

Figure 38 – EDX spectra of the oxide in the root (a) and within the oxide of the root (b) of the Alloy 82 weld after exposure for 5 days.

Appendix B: Calculation of Oxygen Partial Pressure at Equilibrium and Atmospheric Reactor Parameters

Calculation of Equilibrium Oxygen Partial Pressure

The partial pressure of oxygen at the dissociation pressure of a metal oxide can be found using the metal oxide chemical equilibrium:

$$aM_{(s)} + \frac{b}{2}O_{2_{(g)}} \rightleftharpoons M_aO_{b_{(s)}}$$

Determining whether or not the reaction above will form a metal oxide can be done using Gibbs free energy. At equilibrium, the Gibbs free energy, ΔG, of the above reaction will be equal to 0. Equation 1 is the Gibbs free energy as a function of the standard Gibbs free energy of formation, ΔG^0.

$$\Delta G_{M_aO_b} = \Delta G^0_{M_aO_b} + R \cdot T \cdot \ln(Q)$$

$$\Delta G_{M_aO_b} = \Delta G^0_{M_aO_b} + R \cdot T \cdot \ln\left(\frac{\alpha M_aO_b}{(\alpha M)^a \cdot (\alpha O_2)^{b/2}}\right) \quad (1)$$

Where R is the ideal gas constant, T is temperature, and α is the activity. For solids, the activity is equal to 1, while for gases it is the partial pressure of the gas.

Assuming both the metal and oxide are solid and oxygen is in its gaseous form, equation 1 is simplified to equation 2.

$$\Delta G_{M_aO_b} = \Delta G^0_{M_aO_b} + R \cdot T \cdot \ln\left(\frac{1}{(P_{O_2})^{b/2}}\right) \quad (2)$$

Where P_{O_2}, is the partial pressure of oxygen. Equating to 0 and isolating for $P_{O_2,eqm}$ yields equation 3 which can be used to solve for the equilibrium partial pressure of O_2 at the metal oxide dissociation pressure at a given temperature.

$$P_{O_2,eqm} = \left[exp\left(\frac{\Delta G^0_{M_aO_b}}{RT}\right)\right]^{2/b} \quad (3)$$

$\Delta G^0_{M_aO_b}$ can be found from data in chemistry and physic handbooks using equation 4. The value of $\Delta G^0_{M_aO_b}$ from equation 4 is in kcal/mol.

$$\Delta G^0_{M_aO_b} = \Delta H^0 + 2.303 \cdot A \cdot T \cdot \log(T) + B \cdot 10^{-3} \cdot T^2 + C \cdot 10^5 \cdot T^{-1} + I \cdot T \qquad (4)$$

ΔH^0, A, B, C, and I are constants. The values of these constants for the H_2O and NiO reactions are given in Table 14.

Table 14 – Constants used in equation 4 to calculate Gibbs standard free energy [64]

	2.303A	B	C	I	ΔH^0
$\boldsymbol{H_{2(g)} + \frac{1}{2} O_{2(g)} \rightleftharpoons H_2O_{(g)}}$	+6.75	-0.64	-0.08	-8.74	-56930
$\boldsymbol{Ni_{(s)} + \frac{1}{2} O_{2(g)} \rightleftharpoons NiO_{(s)}}$	-4.61	+2.16	-0.10	34.41	-57640

Sample Calculation for the O_2 Partial Pressure at the Ni/NiO Equilibrium

The following is an example calculating O_2 Partial Pressure at the Ni/NiO Equilibrium for the 480ºC atmospheric reactor exposures in Chapter 5. The chemical equation for the Ni/NiO equilibrium is:

$$Ni_{(s)} + \frac{1}{2} O_{2(g)} \rightleftharpoons NiO_{(s)}$$

Both Ni and NiO are solids so effectively their activities are 1. Assuming this, the $P_{O_2,eqm}$ can be calculated from equation 3. First the ΔG^0_{NiO} must be found using equation 4 and the constant values given in Table 14.

$$\Delta G^0_{NiO} = \Delta H^0 + 2.303 \cdot A \cdot T \cdot \log(T) + B \cdot 10^{-3} \cdot T^2 + C \cdot 10^5 \cdot T^{-1} + I \cdot T$$

$$= -40.51 \frac{kcal}{mol} = -169.5 \frac{kJ}{mol}$$

Assuming temperature is 480ºC, the equilibrium partial pressure of oxygen can be found:

$$P_{O_2,eqm} = \left[exp\left(\frac{\Delta G^0_{NiO}}{RT}\right)\right]^2 = \left[exp\left(\frac{-169500\ \frac{J}{mol}}{(8.314\ \frac{J}{mol \cdot K}) \cdot (480 + 273)K}\right)\right]^2$$
$$= 3.04 \times 10^{-24}\ bar$$

By keeping the partial pressure of oxygen below the dissociation pressure, no NiO will form. Primary water reactors maintain conditions slightly above or below this equilibrium pressure. Similar dissociation calculations were performed for Cr/Cr_2O_3 and Fe/Fe_3O_4 the $P_{O_2,eqm}$ for each of those equilibriums are:

- $P_{O_2,eqm}$ for $Cr/Cr_2O_3 = 5.21 \times 10^{-37}\ bar$
- $P_{O_2,eqm}$ for $Fe/Fe_3O_4 = 2.83 \times 10^{-28}\ bar$

It should be noted that the Cr/Cr_2O_3 and Fe/Fe_3O_4 dissociation pressures are many magnitudes lower than the Ni/NiO dissociation pressure. This means that if Cr or Fe is present in sufficient quantity, internal or external oxidation could occur for either minor element.

Calculation of the Ratio of Steam to Hydrogen (R_{H_2O/H_2}) Needed for 480ºC Exposures

Ideally, the oxygen partial pressure should be maintained near those of the Ni/NiO equilibrium, or below it. This means the oxygen partial pressure at 480ºC in the atmospheric reactor must be below $3.04 \times 10^{-24}\ bar$. The amount of oxygen in the atmospheric reactor at any given time is governed by the steam dissociation reaction:

$$H_{2_{(g)}} + \frac{1}{2} O_{2_{(g)}} \rightleftharpoons H_2O_{(g)}$$

It is easy to recognize that increasing hydrogen will reduce the amount of oxygen. The amount of oxygen, assuming equilibrium, can be found from the Gibbs free energy equation for steam dissociation in equation 5.

$$\Delta G^0_{H_2O} = -R \cdot T \cdot \ln\left(\frac{P_{H_2O}}{(P_{O_2})^{1/2} \cdot P_{H_2}}\right) \quad (5)$$

Isolating for P_{O_2}, yields equation 6, with R_{H_2O/H_2} is defined as the ratio between steam and hydrogen.

$$P_{O_2} = \left[R_{H_2O/H_2} \cdot exp\left(\frac{\Delta G^0_{H_2O}}{R \cdot T}\right)\right]^2, where\ R_{H_2O/H_2} = \frac{P_{H_2O}}{P_{H_2}} \quad (6)$$

The value of $\Delta G^0_{H_2O}$ can be found using equation 4 and the values for the steam dissociation reaction in Table 14. The value of $\Delta G^0_{H_2O}$ at 480ºC is -206100 J/mol.

The easiest way to determine P_{O_2} for experiments is to determine the value of R_{H_2O/H_2} at $P_{O_2,eqm}$ at the Ni/NiO dissociation pressure and set P_{O_2} at values below $R_{\frac{H_2O}{H_2},eqm}$. This is done by setting $P_{O_2} = P_{O_2,eqm} = 3.04 \times 10^{-24}\ bar$ and solving for $R_{\frac{H_2O}{H_2},eqm}$. This is shown in equation 7.

$$P_{O_2} = P_{O_2,eqm} = \left[R_{H_2O/H_2} \cdot exp\left(\frac{\Delta G^0_{H_2O}}{R \cdot T}\right)\right]^2$$

$$R_{H_2O/H_2} = \frac{\sqrt{P_{O_2,eqm}}}{\exp\left(\frac{\Delta G^0_{H_2O}}{R \cdot T}\right)} = 346 \quad (7)$$

By keeping the R_{H_2O/H_2} below 346, no NiO will be formed. Effectively, the system will be running below the Ni/NiO dissociation pressure similar to primary water conditions.

We can now set values of R_{H_2O/H_2} and use these to find the desired P_{O_2} for the 480ºC exposures. Assume $R_{H_2O/H_2} = 100$, P_{O_2} can be determined from equation 6:

$$P_{O_2} = \left[R_{H_2O/H_2} \cdot exp\left(\frac{\Delta G^0_{H_2O}}{R \cdot T}\right)\right]^2 = 2.53 \times 10^{-25}\ bar$$

The value of P_{O_2} is 12 times below the Ni/NiO dissociation pressure and was used for two experiments performed in Table 5.

Determining the Flow Rate of Hydrogen Gas and Water to the 480ºC Reactor

Now the desired P_{O_2} and R_{H_2O/H_2} have been determined for the atmospheric reactor. The last step is to determine the actual flow rate of water and hydrogen to the system inputted at 25ºC. This can be done using the law of conservation of mass and the ideal gas law. Also, the number of moles and temperature of steam and hydrogen remain constant throughout the experiment so

the ratio of pressures in R_{H_2O/H_2} can be re-written as the ratio of flow rates as shown in equation 8.

$$R_{H_2O/H_2} = \frac{P_{H_2O_{(g)},480C}}{P_{H_{2(g)},480C}} = \frac{Q_{H_2O_{(g)},480C}}{Q_{H_{2(g)},480C}} \tag{8}$$

$P_{H_2O_{(g)},480C}$ can be related to $P_{H_2O_{(l)},25C}$ by the law of conservation of mass. The mass of water and steam will remain constant. Therefore, the flow rate of water at 25ºC can be written as shown in equation 9.

$$Q_{H_2O_{(l)},25C} \cdot \rho_{H_2O_{(l)},25C} = Q_{H_2O_{(g)},480C} \cdot \rho_{H_2O_{(g)},480C}$$

$$Q_{H_2O_{(g)},480C} = \frac{Q_{H_2O_{(l)},25C} \cdot \rho_{H_2O_{(l)},25C}}{\rho_{H_2O_{(g)},480C}} \tag{9}$$

Where Q and ρ are the flow rate and density respectively. The flow rate of hydrogen can be calculated using the pressure-volume-temperature relationship from the ideal gas law, assuming hydrogen is always in its gaseous state. This is shown in equation 10.

$$\frac{P_{H_2} \cdot Q_{H_2,25C}}{T_{25C}} = \frac{P_{H_2} \cdot Q_{H_2,480C}}{T_{480C}}$$

$$Q_{H_2,480C} = \frac{Q_{H_2,25C} \cdot T_{480C}}{T_{25C}} \tag{10}$$

Equation 8 can now be solved in terms of the flow rates of hydrogen and water at 25ºC by substituting in equations 9 and 10. This is done in equation 11.

$$R_{H_2O/H_2} = \frac{Q_{H_2O_{(l)},25C} \cdot \rho_{H_2O_{(l)},25C} \cdot T_{25C}}{\rho_{H_2O_{(g)},480C} \cdot Q_{H_2,25C} \cdot T_{480C}} \tag{11}$$

All variables in equation 11 are known except for the flow rates of hydrogen and water at room temperature. One of these variables can be set prior to the experiment. The R_{H_2O/H_2} is also set, knowing that it must be below the Ni/NiO equilibrium dissociation pressure, at 346. Continuing with the previous example, set the $R_{H_2O/H_2} = 100$ which will have the system running 12 times

below the Ni/NiO dissociation pressure. Also, set the hydrogen flow rate, $Q_{H_2,25C}$, constant at 32.65 ml/min. Using equation 11, the flow rate of water, $Q_{H_2O_{(l)},25C}$, can be found:

$$Q_{H_2O_{(l)},25C} = \frac{R_{H_2O/H_2} \cdot \rho_{H_2O_{(g)},480C} \cdot Q_{H_2,25C} \cdot T_{480C}}{\rho_{H_2O_{(l)},25C} \cdot T_{25C}} = 2.5\ ml/min$$

Assume that $\rho_{H_2O_{(g)},480C} = 2.94 \times 10^{-4}\ kg/l$ and $\rho_{H_2O_{(l)},25C} = 1\ kg/l$.

In this section, I have now successfully calculated the conditions for experiments 2 and 5 in Table 5. These conditions are as follows:

$P_{O_2} = 2.53 \times 10^{-25}\ bar$

$R_{H_2O/H_2} = 100$

$Q_{H_2O_{(l)},25C} = 2.5ml/min$

$Q_{H_2,25C} = 32.65\ ml/min$

$T = 480^{O}C$

$P = 1\ atm$

At these conditions, the experiment was successfully run at 12 times below the Ni/NiO dissociation pressure. Calculations for all other 480ºC atmospheric reactor exposures were performed in a similar fashion.

Appendix C: Experimental Details and Results for High Pressure Exposures to Hydrogenated Steam at 375ºC

C-1 Experimental Details

Alloy 82 weld samples were exposed to hydrogenated steam at 10.0 MPa total pressure and 375ºC in an autoclave vessel. Only hydrogen and steam were present in the autoclave during exposure. The initial hydrogen and steam partial pressure were maintained below the Ni/NiO dissociation pressure. However, the autoclave is a batch system and hydrogen and steam were never refreshed during experiments. Calculations demonstrating how the steam to hydrogen ratio was maintained below the Ni/NiO dissociation pressure are similar to those done in the low pressure 480ºC exposure, which can be found in Appendix B. The calculation is modified slightly due to the pressure increase to 10.0 MPa which was taken into account (in the ratio of hydrogen to steam).

Sample Preparation

Samples were mechanically polished similar to the low pressure exposures in hydrogenated steam at 480ºC. See Section 5.1.1 for additional sample preparation details.

Description of System and Operating Procedure

The autoclave vessel used was 2.2 litres and rated for temperatures up to 400ºC. It has 3 primary connections: an inlet to place water, and inlet for gas, and an outlet for gas. There is a thermocouple extending into the autoclave through the bottom of the vessel to record temperature. Also, a rupture disk is connected to the bottom of the vessel for safety. There are two additional outlet pipes on the bottom of the autoclave which were not used for this experiment; these pipes were filled with water and kept at room temperature throughout exposures.

The autoclave is made of hastelloy. Samples cannot be allowed to touch any metallic part of the autoclave during experiments. As such, samples were lowered into the autoclave vessel using a ceramic tray. Care was taken to ensure that the ceramic tray would not be interfered with during water addition.

There were several flaws present throughout this experiment:

1. Previously, the autoclave vessel used had not run at operating temperatures above 315ºC. The increase in temperature to 375ºC caused Teflon, used for sealing, to deform. This may have caused the autoclave to leak for many exposures. Eventually, problems with leaks were resolved. However, given the extremely small size of the hydrogen molecule and the small quantity used, there is still the possibility that some hydrogen could have escape for the successful exposures.
2. The autoclave is a batch system. Hydrogen and steam are not refreshed throughout the experiment. This is unlike the primary water circuit and the 480ºC low pressure exposures which are continuously refreshed.
3. At the end of experiments. it was impossible to remove the autoclave lid before 8-10 hours of cooling time. Steam was found to condense on the samples where streaks of oxidation were observed.
4. Hydrogen could be adsorbed by the autoclave vessel itself. This could reduce the hydrogen partial pressure below the Ni/NiO dissociation pressure. However, additional hydrogen was added to counter this (although the amount adsorbed was never determined).

The operating procedure is as follows:

1. The autoclave was cleaned using acetone and deionized water. Samples were placed in the centre of the autoclave on a ceramic tray. The autoclave was then sealed using an O-ring attached to a lid.
2. Air present in the autoclave was removed by slowly pressurizing and de-pressurizing the autoclave with pure nitrogen five times. While maintaining a steady flow of nitrogen, a valve was removed and the desired amount of deaerated water was added to the vessel. The autoclave was then sealed completely and pressurized with the desired amount of hydrogen using a 95% nitrogen and 5% hydrogen mixture.
3. The autoclave was heated to a controlled temperature of 375°C over a period of 4 hours.
4. Once the autoclave reached 375 °C, the experiment was allowed to proceed over a period of 3-5 days and approximately 10.0 MPa of hydrogen and steam.
5. After exposure, the autoclave was allowed to cool for 8 hours. The sealed autoclave lid was removed (this took approximately 1-2 hours) and samples were taken out for analysis.

Sample Removal and Storage

Unfortunately, samples were kept in the autoclave up to 10 hours after exposure. This was to allow the autoclave to cool. Also, the Teflon used for sealing the autoclave was completely deformed. Once the samples were removed, there were areas where steam had condensed on the exposed samples. In some instances, this created visible streaks along the sample which are not indicative of exposure at 400ºC and 10.0 MPa.

Once removed from the autoclave, samples were ultrasonically cleaned in ethanol and placed in a desiccator. Samples were analyzed using SEM and EDX within a week of exposure.

List of Experiments Performed and Calculation Changes to Determine Variables in Appendix B

Table 15 is a list of experiments performed in the autoclave vessel. Temperature was maintained at 375ºC for all experiments. Ideally, the desired temperature for exposure was 400ºC. However, the autoclave vessel was rated for 400ºC and it was unsafe to perform exposures at the rated limit. The temperature and pressure decrease would result in slowed kinetics. The equilibrium partial pressure of O_2, determined from experiments similar to those in Appendix B, was 1.25×10^{-29}.

Table 15 – List of experiments performed at 375ºC at 100 bar. Weld samples from two Alloy 82 welds were exposed.

Test #	Duration (h)	P_{O2} (Pa)	Distance from $P_{O2, Ni/NiO}$
1	120	4.15×10^{-31}	30 times below
2	120	1.25×10^{-30}	10 times below
3	120	4.15×10^{-31}	30 times below
4	120	1.25×10^{-30}	10 times below
5	120	4.15×10^{-31}	30 times below

The steam/hydrogen ratio, partial pressure of O_2, and the distance from the dissociation Ni/NiO partial pressure of O_2 ($P_{O2, Ni/NiO}$) is given; the calculation of each of these variables is given in detail in Appendix B. Experiments one and two were performed with only the first weld acquired. The remaining three were performed with samples from both welds. Scenini performed similar experiments at 400ºC and 20.7 MPa and determined that the theoretical dissociation partial pressure of O_2 was below the actual dissociation partial pressure of O_2 [64]. He performed experiments and determined that the Ni/NiO transition occurred at hydrogen partial pressures approximately five to ten kPa higher than expected [64]. In this study, most experiments were run well below the Ni/NiO dissociation pressure to counteract any differences between theoretical calculations and experiments.

There are differences between those calculations in Appendix B and calculations for this experiment. The partial pressures of hydrogen and steam were calculated using the ratio of steam to hydrogen necessary to have conditions near the Ni/NiO equilibrium. It was assumed that the overall pressure of the system was 100 bar. Hence, using the known ratio of steam to hydrogen the individual partial pressures of hydrogen and steam could be calculated. Also, steam cannot be treated as an ideal gas. Van der waals equation was used to determine the necessary amount of steam needed from water. Finally, the water and hydrogen inputted to the system in Appendix B was treated as a flow rate because the low pressure atmospheric reactor is a continuous system. For high pressure experiments, in a batch autoclave, the volume (or pressure) of hydrogen and volume of water are needed instead of flow rates.

C-2 Results

Figure 39 is typical Alloy 82 weld samples after exposure. Even though all experiments were run under similar conditions, there was difficulty detecting similarities between exposed samples macroscopically. It is difficult to distinguish between the filler, root, and parent material. However, the oxide is darker on the root portion of the weld slowly becoming less dark towards the edge of the filler. This could indicate the formation of an iron oxide in the root of the weld. Welds were further analyzed using SEM and EDX. Unfortunately, no AES or XPS analysis was performed on the exposed samples.

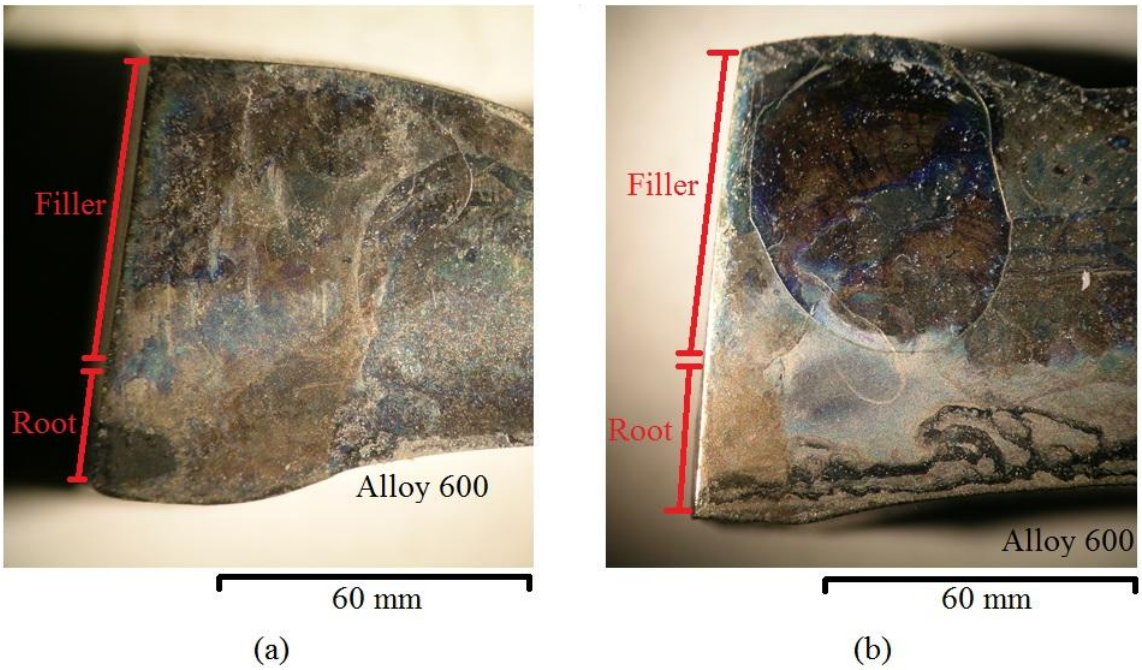

Figure 39 – Typical exposed weld samples after exposure in an autoclave 10 times (a) and 30 times (b) below the Ni/NiO dissociation pressure.

SEM and EDX Analysis of the Alloy 82 Root

SEM analysis was done on the Alloy 82 root. There were a few similarities between the exposed samples on a microscopic level. There were regions which contained a mixture of a darkened areas and flakes, such as in Figure 40 (a). The darkened region could be an external oxide but does not show signs of any small oxide particles (see Figure 40 (b)). The flakes could be caused by internal oxidation of chromium but does not have an appearance similar to those nodules in Chapter 5 (see Figure 40 (c) and (d)).

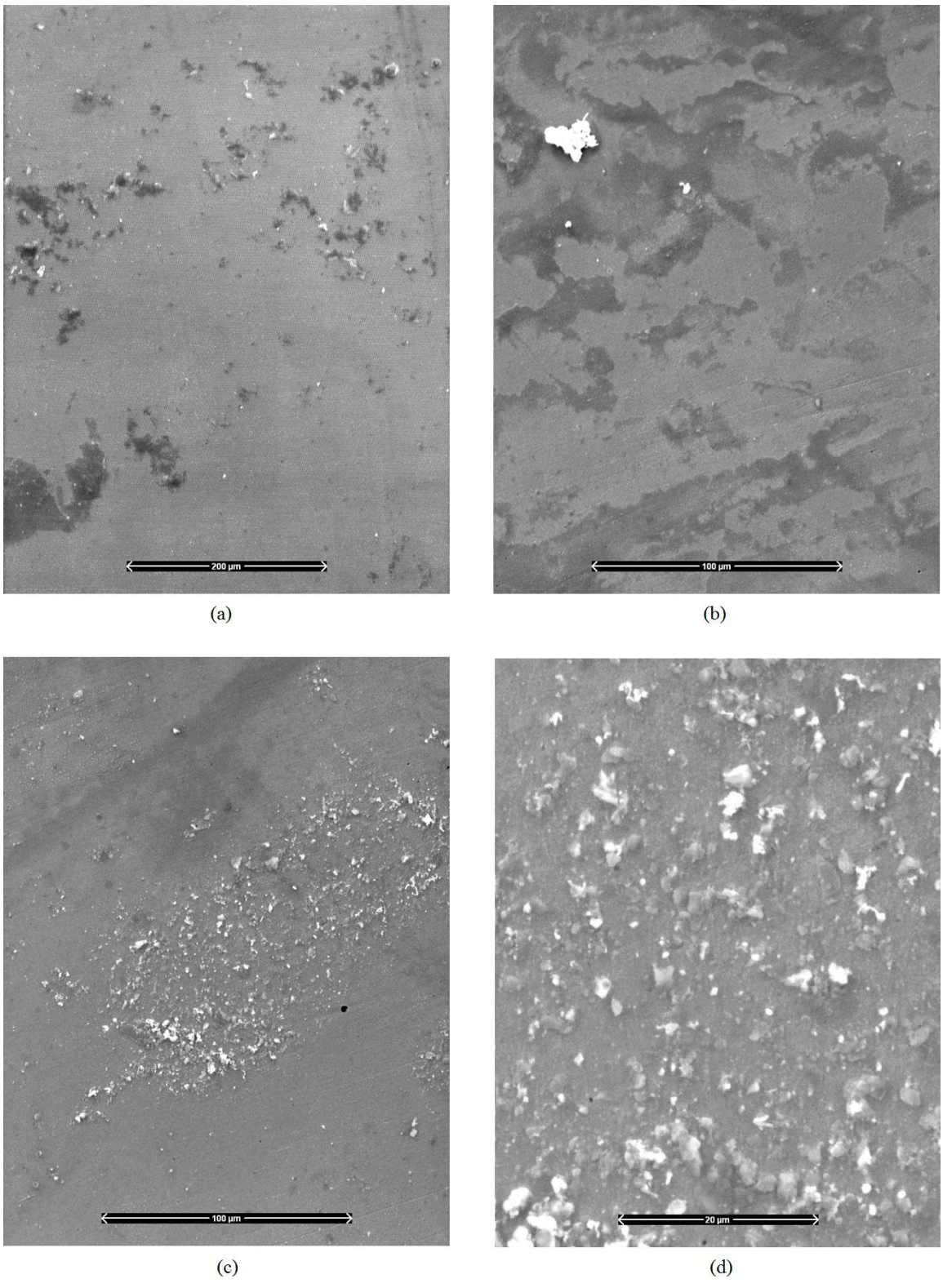

Figure 40 – Typical Alloy 82 weld root region with darkened areas and areas with flakes, Figure 40 (a). Figure 40 (b) shows higher magnification of a darkened region and Figure 40 (c) shows higher magnification of an area with flakes. Figure 40 (d) further magnifies the flakes.

Table 16 is the EDX results of a darkened region shown in Figure 40 (b) and the flakes shown in Figure 40 (c) and (d). The results are inconclusive. With regards to the darkened region, the composition is similar to the unexposed Alloy 82 root.

The most common similarity between Alloy 82 exposed weld samples is the presence of flakes throughout the root (see Figure 40 (c) and (d)). Table 16 gives the compositional analysis of these flakes from EDX spectra. The flakes are definitely enriched in nickel. Unfortunately, the nickel enrichment is not as pronounced as those on the nickel nodules in Chapter 5. It is possible that that some regions around the flakes were erroneously included in the analysis which caused increases in iron and chromium content. These flakes may have been expelled by internal oxidation of chromium but the high concentration of chromium and iron make this debatable.

Table 16 – EDX results for the composition in the darkened region and flakes in Figure 40

Region	Ni	Fe	Cr	Mn, Ti, Nb, Al, Si
Darkened region shown in Figure 40 (b)	51.5	34.5	11.5	Bal.
Flakes on root in Figure 40 (c) and (d)	61.0	21.1	14.1	Bal.

SEM and EDX Analysis of the Alloy 82 Filler

SEM images of the Alloy 82 filler showed very small particles distributed in lines throughout the exposed sample as shown in Figure 41 (a). The filler region closer to the root of the weld has dense regions with similar particles as shown in Figure 41 (b). These particles could be nodules of nickel being expelled by internal oxidation of chromium or an external oxide. The small particles are significantly smaller than the nodules observed in Chapter 5 (see Figure 41 (c). The easiest way to analyze the particles was to perform EDX analysis on areas of the filler where a high density of small particles appear and compare that to an empty area in the vicinity of the small particles.

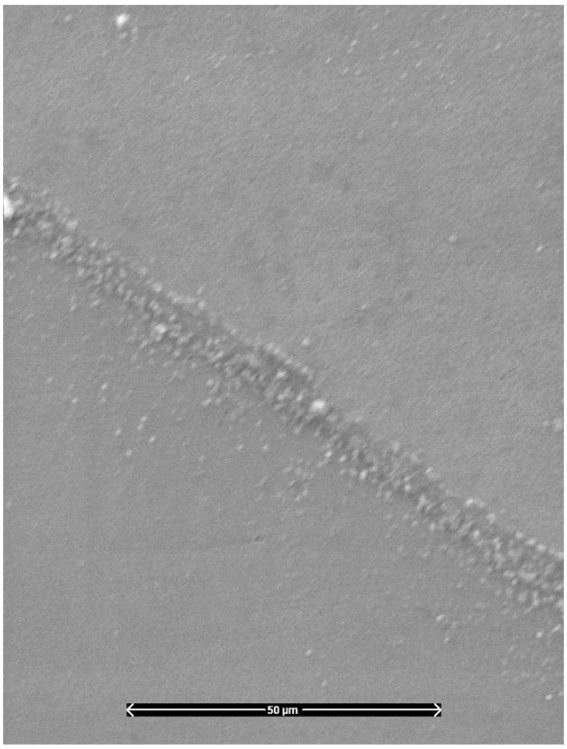

(a)

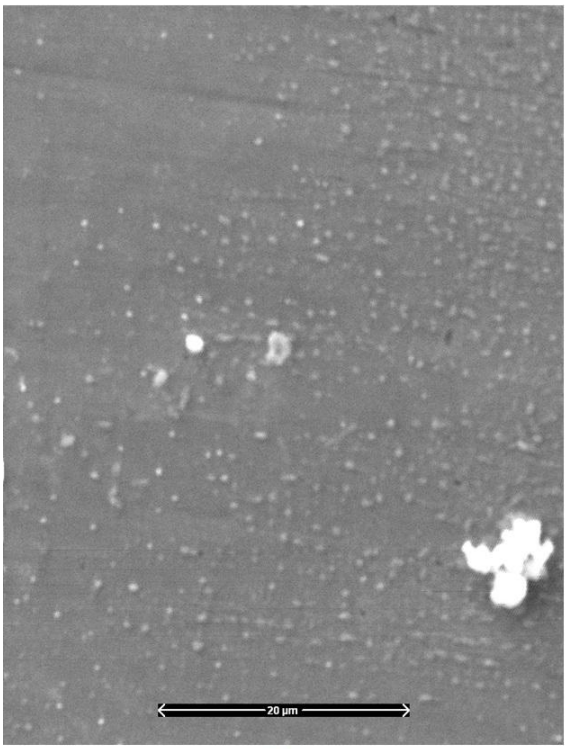

(b)

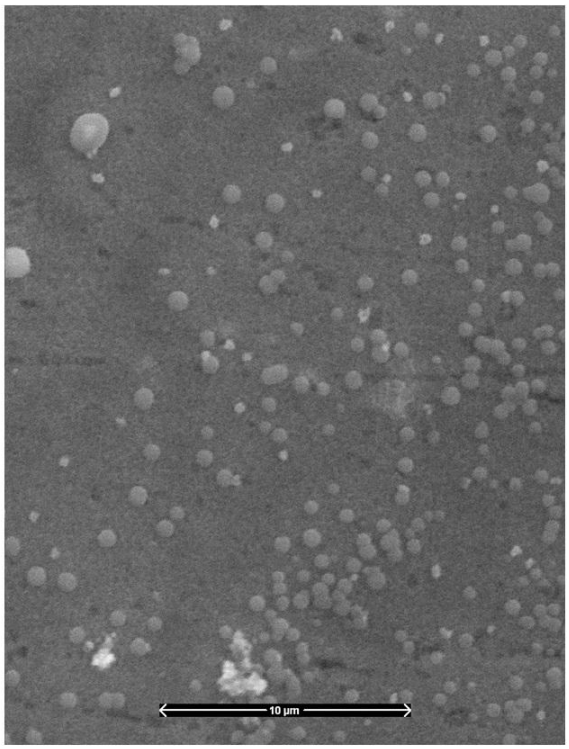

(c)

Figure 41 – The particles are separated by empty areas and appear in lines (a). More small particles appear as you move closer to the Alloy 82 root (b). The particles are significantly smaller than those in Chapter 5 as shown by high magnification (c)

The EDX results for the lines of small particles present in the filler of exposed weld samples is given in Table 17. There is a slight enrichment in nickel and chromium but the enrichment is not significant enough to make any concrete conclusions.

It is possible that the small particles could be pure nickel expelled by internal oxidation of chromium. However, it could also be an oxide. A more sensitive surface analytical technique needs to be employed to determine the composition of these particles.

Table 17 – EDX results for the small particles in Figure 41

Region	Ni	Fe	Cr	Mn, Ti, Nb, Al, Si
A cluster of small particles shown in Figure 41	69.0	11.1	16.8	Bal.
Around the small particles shown in Figure 41	63.7	19.3	13.5	Bal.